Impact Loading and Rapid Volumetric Assessment of Braided Composite Structures

Alexander Benjamin Dondish

A thesis submitted to the Faculty of Graduate Studies in partial fulfillment of the requirements for the degree of Master of Applied Science

Department of Mechanical Engineering

Lassonde School of Engineering

York University

Toronto, Ontario, Canada

Abstract

Braided composites have become a viable alternative to traditional materials in performance-critical applications, with advantages including favourable specific strength and stiffness and highly tailorable properties. However, their inherent complexity and heterogeneity pose challenges in thoroughly assessing their load response. Micro-computed tomography (μCT) offers a method for examining materials and their internal structures through volumetric X-ray imaging. This thesis explores an automated method of rapidly characterizing the internal structures of braided composites subjected to impact testing. The developed methodology is based on algorithms that use image processing techniques to segment and analyze various features in sample volumes. The extracted features in braided composites for study are geometric profiles, voids, and impact damage. The results from the developed algorithms are supplemented with three-dimensional strain measurements by digital volume correlation (DVC).

Dedication

This thesis is dedicated to my loving parents, Sergey and Elena Dondish, who have raised me and supported me in learning, helping others, and ultimately growing as a person.

Acknowledgements

Firstly, I would like to acknowledge my supervisor, Dr. Garrett Melenka, who has provided me the opportunity to perform research under his guidance, for undergraduate research terms in the past, and eventually for full-time graduate terms. Throughout my research work, I was able to gain and develop a variety of new skills in my journey of life-long learning. Dr. Melenka has taught me how to perform systematic research, to develop a clear experimental workflow, and to effectively communicate my ideas and findings to others, both verbally and in writing, ultimately developing my independent working and communication skills. He has also provided me various opportunities to work alongside industry partners, helping me to develop my collaboration skills. He has an open mindset to research, and has given me excellent opportunity to ask questions, to express my thoughts and ideas, and to ultimately grow as a professional and as a person. I would like to extend my deepest gratitude to him and consider him as a supportive and excellent research supervisor.

I would also like to acknowledge all my close lab mates, who have helped bring a sense of belonging in the research space for me. I enjoyed witnessing how their work has developed and learning from their experiences within their respective specialties. I would like to thank them for their willingness to generously provide me with the support that helped me improve my thesis work. I am also grateful for the opportunities that I had to provide them with support as well, as it brought me joy to see them succeed. Overall, I value the time spent with them both inside and outside of the lab.

Table of Contents

Abstract ii

Dedication iii

Acknowledgements iv

Table of Contents v

List of Figures viii

List of Tables xiii

List of Abbreviations xiv

List of Variables xvi

Chapter 1 Introduction 1

1.1 Motivation 1

1.2 Thesis Objective 4

1.3 Thesis Scope 5

1.4 Thesis Outline 5

1.5 References 7

Chapter 2 Literature Review 10

2.1 Introduction 10

2.2 Composite Materials 11

2.2.1 Fundamentals of Composite Materials 11

2.2.2 Braided Composites 15

2.3 High Strain Rate Testing of Composite Materials 20

2.3.1 Impact Testing Methods 20

2.3.2 Fundamentals of Split Hopkinson Bar Testing 22

2.3.3 Split Hopkinson Pressure Bar in Braided Composites 23

2.4 Damage Analysis of Composite Structures 34

2.4.1 Non-Destructive Testing Methods 34

2.4.2 Fundamentals of Computed Tomography 35

2.4.3 Computed Tomography for Analysis of Composites 39

2.4.4 Digital Volume Correlation 44

2.5 Gaps in Literature 49

2.6 Proposed Study 50

2.7 References 50

Chapter 3 Assessment of Low-Velocity Impact Response of a Hybrid Carbon-Aramid Braided Composite by Algorithmic Quantification of Volumetric Structures 67

3.1 Introduction 67

3.2 Methods 70

3.2.1 Sample Preparation 70

3.2.2 Impact Testing 71

3.2.3 Volumetric Scanning 72

3.2.4 Image Processing 74

3.2.5 Digital Volume Correlation 81

3.3 Results & Discussion 82

3.3.1 Volume Registration 82

3.3.2 Volume and Void Analysis 85

3.3.3 Digital Volume Correlation 94

3.4 Conclusions 98

3.5 Acknowledgements 99

3.6 Supplemental Files 99

3.7 References 100

Chapter 4 Conclusions, Recommendations, and Future Work 109

4.1 Conclusions 109

4.2 Recommendations 113

4.3 Future Work 114

Appendix A Image Processing for Braided Composites 116

Appendix B Multi-Layered Braided Composite Manufacturing 143

List of Figures

Figure 1-1: Market value forecast between 2022 and 2032 of: (a) composites using a compound annual growth rate of 7.29% [1]; (b) hybrid composites using a compound annual growth rate of 17.45% [2]........ 1

Figure 2-1: Schematics of (a) single-layer fibrous; (b) multi-layer laminate; (c) particulate reinforced composites........ 12

Figure 2-2: Manufacturing methods for composites: (a) hand lay-up; (b) RTM; (c) pultrusion; (d) filament winding........ 15

Figure 2-3: 2D tubular braided composite: (a) maypole braiding schematic; (b) dry fibre preform; (c) final tubular braided composite part........ 16

Figure 2-4: Diagrams of braid preform architectures with labelled unit cells: (a) Diamond (1/1); (b) Regular (2/2); (c) Hercules (3/3); (d) Regular (2/2) triaxial........ 16

Figure 2-5: Diagrams of (a) open-mesh; (b) closed-mesh braided composite fibre preforms...... 17

Figure 2-6: Diagrams of hybrid braid configurations: (a) hybrid lay-up – material within layers are varied; (b) hybrid textile – materials within the textile are varied; (c) commingled composite – materials within the yarn tows are varied........ 19

Figure 2-7: Schematic of damage modes of fibre-reinforced composite materials........ 21

Figure 2-8: Schematic of a split Hopkinson pressure bar apparatus with a transversely mounted tubular braided composite sample........ 23

Figure 2-9: Common defects in composites: (a) voids formed in the matrix material after curing; (b) ply wrinkling from the hand lay-up process; (c) material cracking from applied impact damage. 35

Figure 2-10: Schematic of the working principles of CT. The process is illustrated for µCT of a braided composite material. 36

Figure 2-11: Illustration of the image reconstruction process for CT. Projections of a sample along the r-z axes are converted into slices of the sample along the x-y axes. The stack of slices is then assembled to form the sample volume. 37

Figure 2-12: SkyScan 1272 µCT apparatus with a tubular braided composite sample on a rotation stage. 38

Figure 2-13: Illustration of image binarization for feature segmentation: (a) original 8-bit image; (b) image histogram with the threshold value selected between the two greyscale value peaks; (c) resultant binarized image. 39

Figure 2-14: Illustration of the DVC process. Identifying geometries that match between the reference and target allow for identification of the necessary transformations for pattern matching. 45

Figure 2-15: Example of the DVC process: (a) intact sample volume as the reference; (b) deformed sample volume as the target; (c) field of local displacement magnitudes generated by DVC. Data provided by Tudisco et al. [98]. 46

Figure 3-1: Hybrid braided composite lay-up: (a) schematic of full tubular cross-section; (b) ply-by-ply material properties; (c) image of sample in cross-sectional view; (d) image of sample in transverse view for braid angle measurement. 71

Figure 3-2: Representative cross-sectional images of the hybrid braided composite sample (a) before impact damage; (b) after impact damage. A defect caused by the hand lay-up process is found in both the undamaged and damaged samples. Sample damage manifested as thin internal cracks and was localized to the impact site. 73

Figure 3-3: Process for registering volumetric datasets from μCT. The damaged dataset is rotated, then vertically translated to align with the matching portion of the undamaged sample. 75

Figure 3-4: Dimensions and coordinate system of registered datasets. The origin of the coordinate system is shown in green in the x-y and x-z views. 75

Figure 3-5: Process for sample geometry analysis and void extraction: (a) original resized image; (b) image histogram with threshold value chosen using peak greyscale values; (c) image filtered and binarized; (d) flood-fill operation applied, creating the outer region; (e) binarized image subtracted from outer region; (f) subtracted image filtered for the largest object, creating the inner region; (g) inner region removed from subtracted image to isolate voids; (h) resultant void objects overlayed in green over the original image. 77

Figure 3-6: Process for registering individual voids. Voids are sorted by size and indices are assigned. Undamaged voids are matched to corresponding damaged void based on size and location similarities. 78

Figure 3-7: Process for impact crack detection: (a) raw resized image; (b) binarized image; (c) mask created by median filtering; (d) binarized image subtracted from mask; (e) image filtered for objects with thin features representing a crack profile; (f) image with small objects removed; (g) mask created by image dilation to identify the largest cohesive region; (h) image features extracted within the largest dilation mask object, representing the final isolated crack; (i) layer arc length versus image slice, used to refine the dilation masking process to eliminate outliers; (j) crack overlayed in red over the original image at z = 0 mm; (k) at z = 4.3 mm; (l) at z = 8.6 mm. 80

Figure 3-8: Digital volume correlation process: (a) the selected regions at the impacted side and opposite side are of equal volume; (b) dimensions of the region of interest at the impacted side with a subset enlarged for illustration. 81

Figure 3-9: Results from DVC sensitivity study: (a) original image slice of the impacted side of the damaged sample at z = 4.3 mm; (b) normal y-strain map for a subset size of 368 µm; (c) 184 µm; (d) 138 µm; (e) 92 µm; (f) 76 µm. 82

Figure 3-10: Visualized image registration results: (a) material volumes: (i) before; (ii) after registration; (b) isolated voids: (iii) before; (iv) after registration. 84

Figure 3-11: Results for topology analysis: (a) measurements of sample inner diameter over vertical position; (b) measurements of sample outer diameter over vertical position; (c) measurements of eccentricity of cross-sectional profiles over sample vertical position; (d) illustration of the inner cross-sectional profile shift at z = 0 mm; (e) at z = 4.3 mm; (f) at z = 8.6 mm. 86

Figure 3-12: Void volume fraction results in the context of the original material volume: (a) undamaged sample; (b) damaged sample. 90

Figure 3-13: Results from individual void analysis: (a) void registration: (i) 40 largest undamaged voids; (ii) corresponding registered damaged voids; (b) void statistical analysis; (iii) histograms of void volumes; (iv) histograms of void positions from sample centre; (v) histograms of void sphericities; (vi) volume change percentages of the largest voids after impact. 91

Figure 3-14: Results from impact crack detection: (a) detected crack in the context of the original material volume; (b) measures of crack arc lengths and areas over sample vertical position; (c) histogram of crack voxel distances from sample centre. 93

Figure 3-15: Normal y-strain maps of x-y slices for the impacted side at: (a) z = 0 mm; (b) z = 2.1 mm; (c) z = 4.3 mm; (d) z = 6.4 mm; (e) z = 8.6 mm. 95

Figure 3-16: DVC measurements of x-z slices for the impacted side: (a) x-y view with locations of selected slices for each material layer; (b) normal y-strain maps of the inner layer; (c) the middle layer; (d) the outer layer. 96

Figure 3-17: Normal y-strain measurements of the impacted and opposite sides: (a) maps of x-y slices at: (i) z = 0 mm; (ii) z = 4.3 mm; (iii) z = 8.6 mm; (b) line plots along dashed lines illustrated in image slices at: (iv) z = 0 mm; (v) z = 4.3 mm; (vi) z = 8.6 mm. 97

List of Tables

Table 2-1: Summary of common fibre materials for composites [1]... 13

Table 2-2: Summary of literature for SHPB testing of braided composites................................. 33

Table 3-1: Micro-computed tomography scan settings for tubular braided composite sample.... 72

Table 3-2: Volume registration results - applied transformations to the damaged sample. 83

Table 3-3: Volume registration results - cross-correlation coefficients between undamaged and undamaged datasets. 84

Table 3-4: Paired-sample t-test results for inner and outer surface topology shifts. 87

Table 3-5: Volume measurement, general statistical data, and t-test results for the voids of the undamaged and damaged samples... 88

Table 3-6: General statistical data of the detected impact crack. 93

List of Abbreviations

FRP	Fibre-Reinforced Polymer
PMC	Polymer Matrix Composite
PAN	Polyacrylonitrile
PP	Polypropylene
PEEK	Poly-Ether-Ether-Ketone
PPS	Polyphenylene Sulfide
2D	Two-Dimensional
3D	Three-Dimensional
3D4d	Three-Dimensional Four-Directional
3D5d	Three-Dimensional Five-Directional
RTM	Resin Transfer Molding
VARTM	Vacuum Assisted Resin Transfer Molding
CLPT	Classical Laminate Plate Theory
FEA	Finite Element Analysis
SHPB	Split Hopkinson Pressure Bar
SHTB	Split Hopkinson Tensile Bar
TSHB	Torsional Split Hopkinson Bar
SHSB	Split Hopkinson Shear Bar
NDT	Non-Destructive Testing
SEM	Scanning Electron Microscope
CT	Computed Tomography

μCT	Micro-Computed Tomography
DVC	Digital Volume Correlation
DIC	Digital Image Correlation
ROI	Region of Interest
BVID	Barely Visible Impact Damage
RVE	Representative Volume Element

List of Variables

I_0	X-ray source light intensity
I	X-ray detector light intensity
μ	light attenuation coefficient
L	length of light path through medium
f	reference volume data
g	target volume data
r	normalized cross-correlation coefficient
D	diameter
A_c	cross-sectional area
e	ellipse eccentricity
a	ellipse semi-major axis
b	ellipse semi-minor axis
v_v	void volume fraction
V_c	volume of composite material
V_v	volume of voids
ψ	three-dimensional object sphericity
$P(t)$	time-dependent applied load
E	modulus of elasticity
ε	normal strain

Chapter 1 Introduction

1.1 Motivation

In the pursuit of increased efficiency of engineered products, weight reduction is a major consideration in the design of parts. This motivating factor has resulted in the adoption of composite materials as a replacement to traditional materials such as metals in various industries. Across industries such as architecture, infrastructure, and automotive, the composites market has been reported to be valued at US$117.5 billion in 2022 with a compound annual growth rate of 7.29% [1]. Additionally, the hybrid composites market has been reported to be valued at US$506.62 million in 2022 with a compound annual growth rate of 17.45% [2]. A ten-year forecast of the composites market is illustrated in Figure 1-1, indicating that the share of hybrid composites (b) in the total composites market (a) is expected to increase from 0.4% to 1.1% between the years 2022 and 2032.

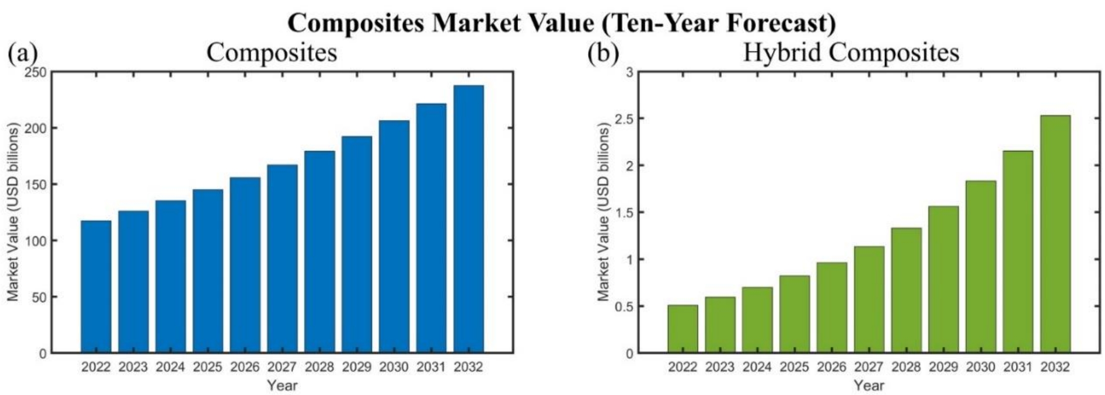

Figure 1-1: Market value forecast between 2022 and 2032 of: (a) composites using a compound annual growth rate of 7.29% [1]**; (b) hybrid composites using a compound annual growth rate of 17.45%** [2]**.**

Composites offer numerous advantages to traditional materials such as high specific stiffness and strength, and most importantly tailorable properties [3]. Modern composites are generally comprised of a reinforcement phase, which serves as the primary load-bearing component, and a matrix phase, which serves as the binding component and forms the cohesion of the material [4]. The most common form of composites for high-performance applications are continuous fibre reinforced composites, which traditionally consist of layers of parallel fibres referred to as laminae which are stacked to form laminates [5]. Fibres can also be interlaced with the objective of enhancing mechanical properties using the interaction between fibre bundles referred to as tows. Fibre tows interlaced orthogonally are used to form textile composites, where fibres are oriented along longitudinal and transverse directions, referred to as warp and weft respectively [3]. Fibres can also be interlaced diagonally at equal angles from a principal longitudinal axis to form braided composites. The angle between fibres and the principal axis is referred to as the braid angle. Braided composites are classified as 2D with a planar braid architecture, or as 3D with yarns interwoven along the three Cartesian axes to improve through-thickness mechanical properties [6]. The primary composite structure discussed in this thesis is 2D braided composites, as they are more economical and commercially available than 3D braided composites and require less specialized equipment to manufacture.

In braided composites, there is significant influence of factors such as braid angle, yarn undulation, voids, and material imperfections on overall mechanical performance. This combination of factors poses a challenge in quality control of braided composite parts, as fibre geometry irregularities and zones of poor resin impregnation are likely to occur from the manufacturing processes and ultimately hinder the mechanical properties of the material [7]. As a result, the adoption of braided composites in industries requires thorough and accurate characterization of materials by investigating these factors and their effects.

To further utilize the tailorable nature of composites, materials can also consist of multiple components of reinforcement or matrix phase. These materials, referred to as hybrid composites, are designed to provide a balance of properties between constituents for specialized applications [8]. For instance, a hybrid material containing high-stiffness graphite fibres and impact-resistant aramid fibres can exhibit good energy absorption properties [9].

Composites occupy a substantial proportion by mass in some multi-purpose vehicles, as well as some commercial aircraft such as the Airbus A320, A380, and A350, and the Boeing 787 [10]. Such vehicles are subjected to various sources of impact damage, such as road debris in the case of ground vehicles, and hail stones and bird strikes in the case of air vehicles. For these reasons, impact performance is a critical factor in materials design for such applications to ensure sufficient part longevity while maintaining the weight-saving benefits inherently provided by composite materials. The response of a material to impact can be characterized using the split Hopkinson pressure bar (SHPB) [11] or the drop-weight test [12].

The increasing market for composites is a major driving factor for efforts in improving cost effectiveness throughout the life cycle of materials and parts. In the pursuit of assessing the structural integrity of composite parts, it is most economically viable to analyze such parts without inducing any further damage, such that the parts can then be repaired as necessary and reused in service. Such assessment of materials is performed using non-destructive testing (NDT) methods such as micro-computed tomography (μCT) [13]. Through μCT, a volumetric profile of a sample is acquired such that features such as material constituents, voids, defects, and damage can be captured and analyzed. The response of a material under loading can be quantified by acquiring a volumetric dataset before and after loading, then using a correlation-based measurement technique known as digital volume correlation (DVC) [14]. DVC provides full-field strain measurements throughout a sample volume, allowing for identification of local material behaviours under loading. Furthermore, this technique is directly comparable to finite element analysis (FEA) and can be used to compare measurements of a physical sample with results from a corresponding numerical model.

1.2 Thesis Objective

This thesis uses the SHPB to apply impact energy to hybrid 2D tubular braided composites, µCT to assess their volumetric features and impact damage, and DVC to measure strains caused by impact. The objective of this thesis is to provide a means of rapidly characterizing and measuring the internal features of advanced materials before and after an impact test. The first requirement to achieve this objective is to create representations of physical samples and their internal structures in a digital form that can be analyzed computationally. This step is achieved by the µCT process where samples are represented by a set of X-ray based images. Next, individual features of materials such as voids, defects, and damage must be identified and analyzed in isolation. This step is achieved by image segmentation where various image processing techniques are used to extract distinct image features and store them as separate objects. Finally, these objects must be quantified to directly correlate impact loading with changes in features. This step is achieved by statistical analysis of objects and DVC. Statistical techniques are used to determine whether certain features experienced significant change due to impact. DVC is used to determine localized material behaviours in the form of volumetric strains. The methodology developed in this thesis was applied to a hybrid 2D tubular braided composite to assess its mechanical response to impact loading. The results will ultimately demonstrate the complex influence of internal features of materials on impact response. Consequently, the methodology can be applied to impact testing of various advanced materials that contain complex volumetric structures.

1.3 Thesis Scope

Experimental procedures were performed on a hybrid 2D tubular braided composite comprised of an inter-ply hybrid lay-up of carbon and aramid fibres. As SHPB impact testing required large-scale equipment to perform, µCT scanning was performed ex-situ, meaning that it was separate from impact testing. The datasets acquired before and after impact were then aligned using image registration by 3D inspection software (DataViewer, Bruker Corporation, Billerica, MA, USA). Image segmentation and statistical analysis of objects was performed using a MATLAB based algorithm that used image processing techniques and paired-sample t-tests. This algorithm was ultimately used to analyze surface geometries, voids, and damage cracks of the hybrid tubular braided composite before and after impact. Analysis from µCT was supplemented with DVC at reduced volumes of interest using a commercial image analysis software package (Avizo 2021.2, Thermo Fisher Scientific, Waltham, MA, USA).

1.4 Thesis Outline

This thesis consists of four chapters. Chapter 2 begins the discussion by providing fundamentals and applications of the critical topics, as well as a review of current literature. Chapter 2 consists of three major topics. The first topic is composite materials, which includes an introduction of fundamentals and in-depth discussion of braided composites and hybrid braided composites. The second topic is high strain rate testing, which includes an introduction of impact testing methods followed by a discussion of SHPB testing and its application to braided composites. The third topic is NDT, which includes an introduction of various forms of NDT followed by a discussion of µCT and DVC and their applications to composites. Finally, current gaps in literature are summarized and discussed to demonstrate the motivation for the work in the subsequent chapters.

Chapter 3 outlines the work performed in this thesis to address the objectives. A detailed description of methodologies for impact testing, μCT, and data processing is provided. The work demonstrates the algorithm developed in MATLAB to provide detailed characterization of internal features of the material and the influence of impact loading by means of statistical analysis. The analysis performed through the algorithm is supplemented with volumetric strain measurement by DVC. A version of this chapter has been submitted to *Composite Science and Technology* and is currently under review.

Chapter 4 summarizes the findings of this thesis and their significance for future work in this field. The first section discusses critical finding of the profile of impact-induced cracking in the hybrid tubular braided composite and its quantified properties. The next section outlines recommendations from the author on successful study of internal structures of impact damaged materials, including sample preparation, sample alignment for μCT, and additional procedures for SHPB. The provided recommendations aim to leverage the knowledge gained from experimental work to aid in future research of impact response of advanced materials. The final section provides suggestions of potential areas of research where the methodologies in this thesis can be applied in the future.

Appendix A provides a detailed demonstration of the image processing steps employed in the algorithm used in this thesis, using a singular image slice of the tubular braided composite sample as an example. Additionally, supplemental data such as reconstructed image slices and code files are provided with instructions on their use [15]. Appendix B provides detailed steps on manufacturing a multi-layered tubular braided composite sample using the hand lay-up process.

1.5 References

[1] "Composites Market Size, Share & Trends Analysis Report by Fiber Type (Glass Fiber Composites, Carbon Fiber Composites, Natural Fiber Composites), Resin Type (Thermoset Composites, Thermoplastic Composites), Manufacturing Process, By End-Use Industry, By Region, And Segment Forecasts, 2023-2031," Mar. 2023.

[2] "Hybrid Composites Market - By Fibre Type, By Resin (Thermoset And Thermoplastic), By End-Use Industry (Automotive & Transportation, Aerospace & Defense, Wind Energy, Marine, Sporting Goods) & By Region (North America, Latin America, Europe, Asia Pacific, Middle East & Africa) - Global Industry Analysis, Size, Share, Growth, Trends, Forecast | 2023-2028," Mar. 2023.

[3] S. Sharma, *Composite Materials*. CRC Press, 2021. doi: 10.1201/9781003147756.

[4] H. V. S. GangaRao and W. Prachasaree, *FRP Composite Structures*. Boca Raton: CRC Press, 2021. doi: 10.1201/9781003196754.

[5] V. V. Vasiliev, *Mechanics of Composite Structures*. CRC Press, 2017. doi: 10.1201/9780203747858.

[6] J. P. Carey, "Introduction to braided composites," in *Handbook of Advances in Braided Composite Materials: Theory, Production, Testing and Applications*, Elsevier Inc., 2017, pp. 1–21. doi: 10.1016/B978-0-08-100369-5.00001-5.

[7] G. W. Melenka *et al.*, "Manufacturing processes for braided composite materials," *Handbook of Advances in Braided Composite Materials: Theory, Production, Testing and Applications*, pp. 47–153, Jan. 2017, doi: 10.1016/B978-0-08-100369-5.00003-9.

[8] V. M. Karbhari, P. J. Falzon, and I. Herzberg, “Energy Absorption Characteristics of Hybrid Braided Composite Tubes,” *J Compos Mater*, vol. 31, no. 12, pp. 1164–1186, Jun. 1997, doi: 10.1177/002199839703101201.

[9] G. L. Farley, R. K. Bird, and J. T. Modlin, “The Role of Fiber and Matrix in Crash Energy Absorption of Composite Materials,” *Journal of the American Helicopter Society*, vol. 34, no. 2, pp. 52–58, Apr. 1989, doi: 10.4050/JAHS.34.2.52.

[10] D. Coutellier, “Composites and Dynamic Failures: Experimental and Numerical Solving Strategies and Solutions,” in *Dynamic Failure of Composite and Sandwich Structures*, 2013, pp. 611–643. doi: 10.1007/978-94-007-5329-7_14.

[11] H. Kolsky, “An Investigation of the Mechanical Properties of Materials at very High Rates of Loading,” *Proceedings of the Physical Society. Section B*, vol. 62, no. 11, pp. 676–700, Nov. 1949, doi: 10.1088/0370-1301/62/11/302.

[12] S. R. Abid, G. Murali, J. Ahmad, T. S. Al-Ghasham, and N. I. Vatin, “Repeated Drop-Weight Impact Testing of Fibrous Concrete: State-Of-The-Art Literature Review, Analysis of Results Variation and Test Improvement Suggestions,” *Materials*, vol. 15, no. 11. MDPI, Jun. 01, 2022. doi: 10.3390/ma15113948.

[13] E. N. Landis and D. T. Keane, “X-ray microtomography,” *Materials Characterization*, vol. 61, no. 12. Elsevier Inc., pp. 1305–1316, 2010. doi: 10.1016/j.matchar.2010.09.012.

[14] A. Buljac *et al.*, “Digital Volume Correlation: Review of Progress and Challenges,” *Exp Mech*, vol. 58, no. 5, pp. 661–708, Jun. 2018, doi: 10.1007/s11340-018-0390-7.

[15] A. Dondish and G. W. Melenka, “Assessment of low-velocity impact response of a hybrid carbon-aramid braided composite by algorithmic quantification of volumetric structures.” Federated Research Data Repository, 2023. doi: https://doi.org/10.20383/103.0770.

Chapter 2 Literature Review

2.1 Introduction

The objective of this work is to develop a method of assessing the impact response of braided composites through the investigation of internal structures using an X-ray based micro-computed tomography (μCT) imaging method. This chapter provides an introduction of the critical topics for this work and an extensive review of literature within the major areas examined in this work. The following sections will present the fundamental principles and current literature of composite materials and braided composites, high strain rate testing, and non-destructive testing (NDT). Finally, this chapter will demonstrate the identified literature gaps and propose the work in this thesis that aims to address this gap.

Braided composites are a cost-effective form of composite materials that have good damage tolerance and impact properties compared to traditional composites, due to the interaction between fibres formed during the braiding process. These properties make braided composites a favourable choice in various impact performance-critical applications such as the aerospace industry. The first section of this chapter will introduce composite materials. Discussion will begin with fundamentals and basic classifications of composites and their constituents. Next, an in-depth discussion on braided composites will be provided, including classification of 2D and 3D braided composites and their braiding patterns, manufacturing methods, and examples of theoretical analysis of their properties.

The next section of this chapter will discuss high strain rate testing for studying the impact properties of composites. First, common methods of impact testing will be introduced and distinguished between low-velocity and high-velocity impact. Next, a discussion of the split Hopkinson pressure bar (SHPB) and its fundamentals will be provided. Finally, a thorough review of works that applied SHPB testing to braided composites will be provided.

The next section of this chapter will introduce NDT methods of evaluating damage and imperfections in composites and some commonly used examples. Then, an in-depth discussion of computed tomography (CT) and its fundamental principles will be provided, as well as a description of imaging processing techniques used to analyze CT data. Next, a thorough review of literature pertaining to CT for various analyses of composites will be provided. Finally, digital volume correlation (DVC) will be introduced, and works that employed DVC in strain measurement of composites will be reviewed.

2.2 Composite Materials

2.2.1 Fundamentals of Composite Materials

A composite material is defined as a material that consists of multiple constituents at a macroscopic level. Traditionally, a composite is made from a reinforcement phase and a matrix phase. The reinforcement acts as a primary subject of load bearing, and the matrix forms the cohesion of the material. The result is a non-homogeneous, multi-phase material with the aim of leveraging advantages from each constituent material for improved performance. Early examples of composite materials are found in straw-reinforced brick for construction of homes in ancient times, and metal-reinforced plastics for canes and umbrella handles in the nineteenth century [1].

Composite materials are used in a wide variety of engineering applications due to their favourable strength-to-weight ratio, corrosion resistance, and ease of customization compared to traditional materials [1]. Examples of current uses of composites include aircraft structures such as wings, fuselages, and stabilizers [2]; marine structures such as vessels, bulkheads, and propellers [3]; biomedical devices such as catheters, joint replacements, and prosthetic devices [4]; and sporting goods such as rackets, swimsuits, and bicycles [5]. As shown in Figure 1-1, composites can be classified as fibrous (a), laminated (b), particulate (c), or any combination of these types [6].

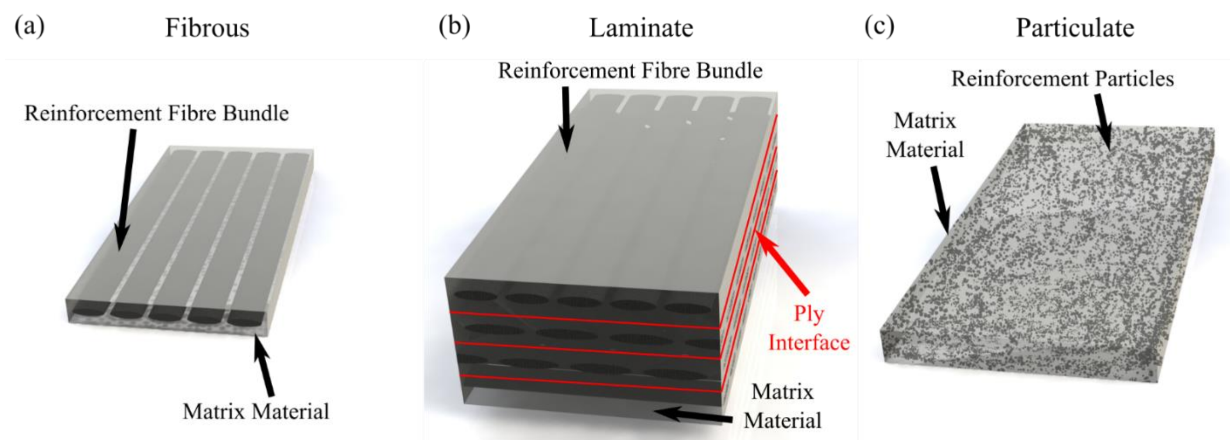

Figure 2-1: Schematics of (a) single-layer fibrous; (b) multi-layer laminate; (c) particulate reinforced composites.

2.2.1.1 Reinforcement Materials

Reinforcement materials are most commonly in the form of fibres, which can be used as long strands individually, in bundles referred to as tows, in woven configurations, or as short fibres. Materials for reinforcement fibres must fulfill intrinsic requirements such as strength, stiffness, and density, as well as extrinsic requirements such as feasibility of manufacturing and compatibility with matrix materials [7]. Carbon fibres are a common material choice for performance-critical applications such as aircraft and are most often manufactured using polyacrylonitrile (PAN) as the precursor. A common alternative precursor for carbon fibres is pitch, which yields fibres that have higher stiffness, but are also more brittle, have lower toughness, and are more costly to manufacture than PAN-based fibres [1]. Ultimately, carbon fibres have high tensile strength and stiffness but are generally costly and brittle. Glass fibres are the most common form of reinforcement material and are used in applications with less strict performance requirements. They are manufactured from various minerals which are melted, extruded, and coated. Glass fibres are ductile and cost-effective but have low stiffness and high hygrothermal sensitivity. Aramid fibres, also referred to as aromatic polyamide, are manufactured through the reaction of para-phenylenediamine and terephthaloyl chloride. Aramid fibres have high impact resistance and thermal resistance but have high moisture absorption and ultraviolet light sensitivity [1]. Properties of these materials are summarized in Table 2-1.

Table 2-1: Summary of common fibre materials for composites [1]**.**

Fibre Material	**Advantages**	**Disadvantages**
Carbon (PAN)	High strength High stiffness	Moderately high cost
Carbon (Pitch)	Very high stiffness	Low toughness High cost
Glass	Low cost High ductility	Low stiffness High hygrothermal sensitivity
Aramid	High impact resistance Good thermal stability	High moisture absorption High UV sensitivity

2.2.1.2 Matrix Materials

The matrix material serves to distribute loading uniformly to the fibres and is subjected to some requirements. The material must adhere sufficiently to the fibres and allow for manufacturing under feasible temperatures and pressures. The most common matrix materials for composites are comprised of polymers [7]. Materials that use polymers as the matrix are referred to as polymer matrix composites (PMC), more commonly referred to as fibre reinforced polymers (FRP). Polymers are classified as either thermoset or thermoplastic. Thermoset polymers undergo chemical bonding known as cross-linking during the curing process and cannot be melted or re-molded. Thermoplastic polymers undergo no additional chemical bonding when curing and can be melted and re-molded.

For thermoset polymers, a common choice for performance-critical applications is epoxy, which is made from epichlorohydrin and bis-phenol and cured with amines. Epoxy has high strength and corrosion resistance but has high cost and curing times. Polyester resin is one of the most widely used polymer matrix materials, which is made from polyhydric alcohols and organic acids and cured with peroxides. Polyester has low cost and low toxicity but has low strength and high shrinkage during curing. Vinyl ester resin is made from epoxy and acrylic or methacrylic acid and cured with peroxides. Vinyl ester has good fracture toughness and resistance to corrosion and various chemicals but is prone to significant shrinkage that can cause part warpage. Polyurethane resin is available in either thermoplastic or thermoset form and is made by reaction injection molding. Polyurethane has high compressive strength and ductility but have high manufacturing cost compared to other resins, which are usually cast rather than injection molded. For thermoplastic polymers, other commonly used materials include polypropylene (PP), poly-ether-ether-ketone (PEEK), polysulfone, and polyphenylene sulfide (PPS) [1].

2.2.1.3 Methods for Manufacturing Composites

Parts made from FRP are manufactured by a wide variety of processes as shown in Figure 2-2. Hand lay-up (a) is the simplest process and is largely manual. Part quality can be improved by applying mechanical pressure using a vacuum bagging technique, or by using an autoclave where temperature and pressure can be controlled. Resin transfer molding (RTM) (b), vacuum assisted resin transfer molding (VARTM), and pultrusion (c) can be used for high-volume production. Filament winding (d) is automated and primarily used for hollow structural components. The manufacturing process is chosen on a case-by-case basis and is dependent on the performance requirements for a given application and equipment availability [6].

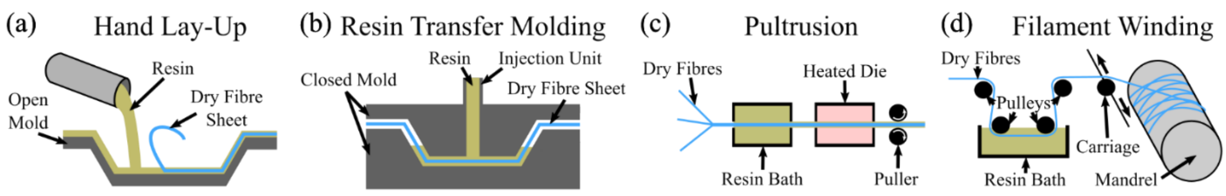

Figure 2-2: Manufacturing methods for composites: (a) hand lay-up; (b) RTM; (c) pultrusion; (d) filament winding.

2.2.2 *Braided Composites*

Braided composites are a classification of composite materials characterized by an interwoven structure of fibres. They are classified fundamentally as 2D or 3D braided composites and are manufactured using maypole, radial, or Cartesian braiders as discussed in this section. As an example, a 2D tubular braided composite is illustrated in Figure 2-3. The maypole braiding process (a) is used to form fibre tows into tubular preforms (b) which are impregnated with a matrix material to form the final part (c).

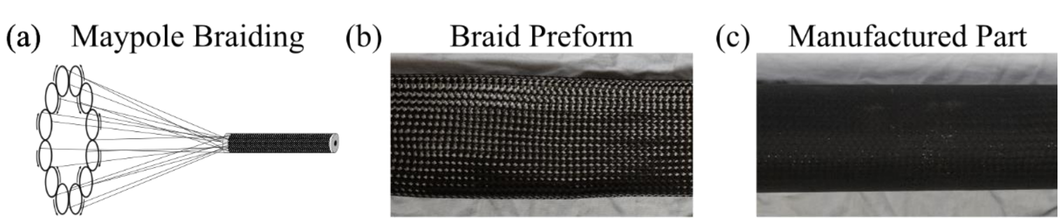

Figure 2-3: 2D tubular braided composite: (a) maypole braiding schematic; (b) dry fibre preform; (c) final tubular braided composite part.

Fibres are primarily configured diagonally, with interlacing tows at equal angles from an axis referred to as the principal axis [8]. Due to interaction between interlacing fibre tows, braided composites have improved toughness over laminate composites. However, the undulations also cause a reduction in stiffness and compressive properties [9]. Additionally, material choice heavily influences a wide variety of mechanical properties as demonstrated by Armanfard and Melenka [10], who found by experimentation that carbon and aramid braids have equally high axial stiffness, carbon braids have high torsional stiffness, and glass braids have relatively low stiffness. There are many commonly used braiding methods that produce fibre configurations with distinct repeating patterns as described in this section. Braiding patterns are represented by a unit cell, which is the unique element of minimal size that fully defines the pattern [8]. Example braid unit-cells are shown in Figure 2-4.

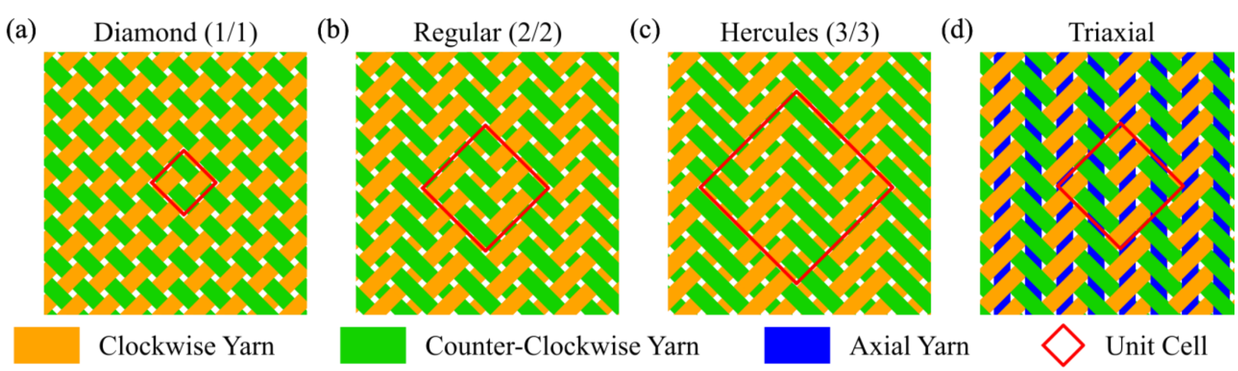

Figure 2-4: Diagrams of braid preform architectures with labelled unit cells: (a) Diamond (1/1); (b) Regular (2/2); (c) Hercules (3/3); (d) Regular (2/2) triaxial.

Braids can be categorized as open mesh as shown in Figure 2-5(a), which have many resin-rich regions resulting in low fibre volume fractions, or as closed mesh as shown in Figure 2-5(b), where fibres are tightly packed, resulting in high fibre volume fractions [8]. Mesh openness is determined by the cover factor, which is defined as the proportion of the surface area occupied by the reinforcement material [11], which is less than 1 for open mesh braids and equal to 1 for closed mesh braids. Open mesh braided composites are used in applications such as catheters, as design requirements included sufficient axial and torsional rigidity, as well as varied bending rigidity between sections. Resin-rich areas provide compliance to the overall material, allowing for the satisfaction of these requirements. An example where closed mesh composites are used is golf club shafts. As this application required higher torsional and bending stiffness, the material design depended on a higher contribution of fibres to the overall material [12].

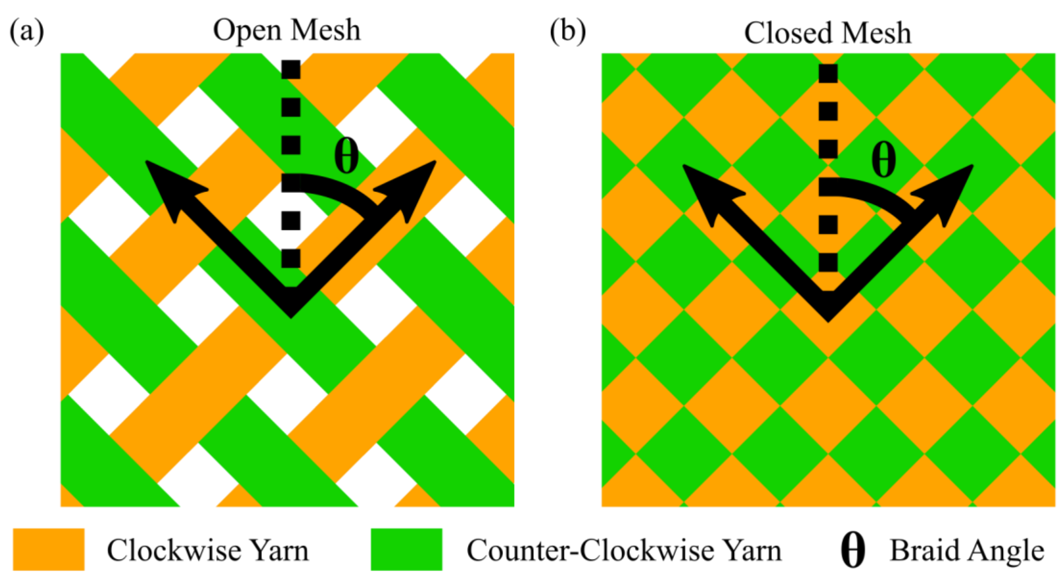

Figure 2-5: Diagrams of (a) open-mesh; (b) closed-mesh braided composite fibre preforms.

Braids that have a planar weave architecture are referred to as two-dimensional (2D) braided composites. Fibre preforms are traditionally prepared using a maypole braider which uses a series of horn gears to interlace bobbins sequentially [13] and can produce preforms in either flat or tubular forms [8]. Alternatively, preforms can be prepared using a rotary braider, which has a higher production rate but can only produce tubular braids [14]. The three most common biaxial braiding patterns are the diamond (one-over-one) pattern as shown in Figure 2-4(a), the regular (two-over-two) pattern as shown in Figure 2-4(b), or the Hercules (three-over-three) pattern as shown in Figure 2-4(c). Additionally, triaxial braiding patterns as shown in Figure 2-4(d) can be formed by adding fibre tows along the principal axis.

Braids with a weave architecture that spans three axes are referred to as three-dimensional (3D) braided composites. 3D braiding has been used to produce various solid structures such as rods and cylinders, as well as complex geometries. Fibre preforms are prepared using either maypole-style techniques such as the solid and 3D rotary braiding processes, or by track and column techniques such as the two-step, four-step, and multi-step braiding processes [15], [16]. Some braid patterns for 3D fibre preforms in increasing order of unit cell structure coarseness include 1 × 1, 2 × 1, 3 × 1, and 4 × 1. This work will focus on 2D braided composites due to their cost-effectiveness and commercial availability, as manufacturing 3D braided composites is significantly more complex and require specialized equipment.

Braided composites that are comprised of multiple components of reinforcement or matrix materials are referred to as hybrid braided composites. The primary objective of hybridization in composites is to optimize the balance of mechanical properties of constituents to tailor a material for specialized applications [17]. For instance, under static crush testing of composite tubes comprised of graphite/epoxy, aramid/epoxy, and hybrid graphite-aramid/epoxy, the hybrid material was found to have high energy absorption properties [18]. Hybrid braided composites are classified as inter-ply hybrids with one material per ply, such as hybrid lay-up, or as intra-ply hybrids with multiple materials per ply, such as hybrid textile and commingled composites [19]. These hybrid configurations are illustrated in Figure 2-6.

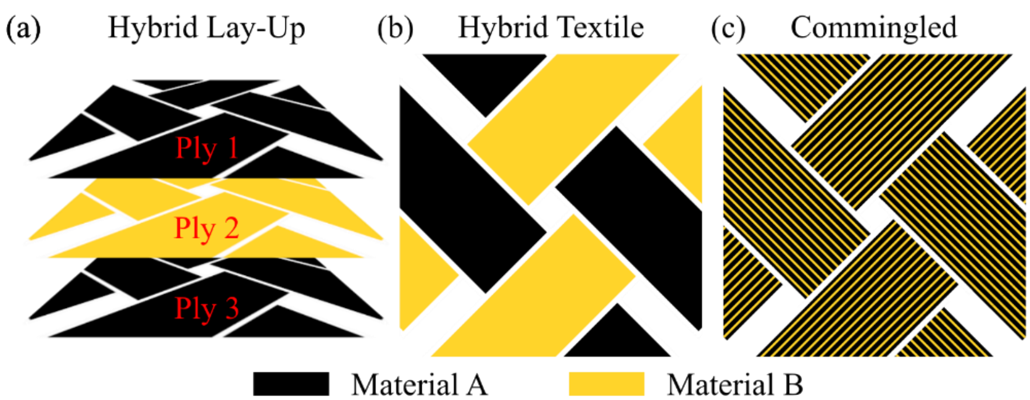

Figure 2-6: Diagrams of hybrid braid configurations: (a) hybrid lay-up – material within layers are varied; (b) hybrid textile – materials within the textile are varied; (c) commingled composite – materials within the yarn tows are varied.

There are many complex properties of braided composites that affect mechanical performance, such as braid angles, undulations, and local interactions within and between tows, thereby adding complications to theories that are applied to traditional composite laminates. In response, various specialized modelling techniques were developed for 2D and 3D braided composites to evaluate engineering constants such as moduli and strengths with sufficient accuracy. Models based on classical laminate plate theory (CLPT), which is derived from the Kirchhoff-Love plate theory [20], primarily modify CLPT equations to account for undulating yarns and tow curvatures under the assumption that loading is strictly in-plane. However, they apply only to thin plies and therefore cannot predict out-of-plane properties [21]. Fabric geometry models represent the materials as straight rods at varying orientations and are used for 3D braided composites. Although this method can generate results quickly, it inherently neglects undulations and curvatures [14]. Volume averaging models aim to address the limitations of other methods by applying coordinate transforms to account for undulations, resulting in more accurate but more resource intensive calculations [22]. Finite element analysis (FEA) models represent braids at the microscale for individual yarns, the mesoscale for individual unit cells, and the macroscale for the full braided structure. For this method, a balance is to be made between model accuracy and computation time based on the defined governing equations and boundary conditions in addition to mesh size [23]. Gholami and Melenka [24], [25] developed a geometric model for 2D tubular braided composites by generating yarn paths based on the desired braiding pattern and yarn parameters. The geometry of the model was compared with an experimental volumetric model, and FEA of tensile loading was performed to compare measured mechanical performance with results from experimental tensile testing [24]. Results were improved using particle swarm optimization, such that errors of less than 1% for the geometric model were achieved [25]. Despite the significant advances in modelling braided composite, a major limitation that remains is the modelling of material imperfections that occur from the manufacturing process and hinder the mechanical properties of the material. To address this limitation, models can incorporate volumetric data from physical samples, such as the model applied to conventional FRP laminates at the microscale by Czabaj et al. [26]. The development of computational modelling techniques for braided composites ultimately reduces the need for experimental testing and accelerates the design of braided composite structures for industries.

2.3 High Strain Rate Testing of Composite Materials

2.3.1 Impact Testing Methods

There are numerous damage modes in composite materials, further adding to the complexity of assessing their impact performance. The expected damage characteristics of a composite specimen are dependent on the material, part geometry, fibre configuration, loading type, loading direction, boundary conditions, and strain rate, among many factors. As shown in Figure 2-7, damage can occur in a composite material either within constituents, such as matrix cracking, fibre fracture, and tow splitting, or between plies or constituents, such as delamination, fibre pull-out, and interface debonding.

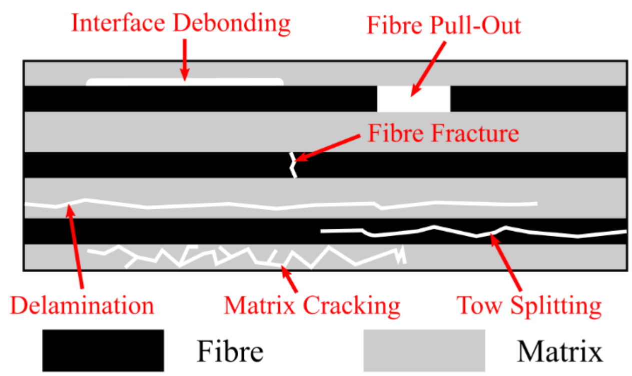

Figure 2-7: Schematic of damage modes of fibre-reinforced composite materials.

A low-velocity impact testing technique that was used by several works for braided composites is drop-weight impact testing, where a mass is lifted to a fixed height from the impact surface of a specimen, then released to allow freefall of the mass to impact the surface, applying impact energy onto the material and inducing an indentation [27]. Shi et al. [28] performed drop-weight impact testing on 2D tubular braided carbon/epoxy composites with various configurations of uniaxial and biaxial layers. This study found that a particular hybrid configuration with an inner uniaxial layer was advantageous in impact resistance at high energy. Na et al. [29] used drop-weight impact testing to study biaxially and triaxially braided carbon/epoxy flat panels and found that the triaxial braids have favourable impact properties owing to a higher fibre volume fraction. Guo et al. [30] examined the effects of material defects on the drop-weight impact performance of 3D braided carbon/epoxy composites and found that the presence of defects strictly hinders the impact properties of the material, with voids located near the centre of the thickness having more significant effects than those located near the surfaces. Wang et al. [31] developed a novel technique of 3D circular braiding to form three-way connected 3D braided composite tubes and applied axial compressive impact by drop-weight testing. For these specimens, compressive strength increased with the applied impact energy and number of braiding layers but decreased with increasing branch tube length due to the differences in stress concentration sites. Wu et al. [32] performed drop-weight impact testing on carbon/epoxy laminates with hybrid biaxial/triaxial braided layer configurations and found that impact resistance improved when triaxial braided layers were closer to the impact surface. Axial yarns in the triaxial braids promoted in-plane matrix cracking and thereby limited through-thickness damage.

Additionally, high-speed impact in the form of direct pressure gas gun impact testing was performed for braided composites by Zhu et al. [33]. Here, 2D triaxially braided carbon/epoxy flat panels were directly impacted by a projectile accelerated through a barrel by gas pressure. Results from damage inspection showed shear failure at the impacted surface and tensile failure at the opposite surface at the impact site. Beyond the impact site, these panels failed primarily by delamination, with in-plane coverage of damage increasing with impact velocity.

2.3.2 Fundamentals of Split Hopkinson Bar Testing

The split Hopkinson bar, also referred to as the Kolsky bar, is an impact testing apparatus developed by Herbert Kolsky [34] as a successor to the original Hopkinson bar developed by Bertram Hopkinson [35]. The apparatus, as shown in Figure 2-8, aims to address limitations of the Hopkinson bar caused by using a directly accelerated projectile. For instance, Hopkinson bar testing relied on an assumption that the projectile was fully fluid, and it was found that projectile rigidity was a major contributor to discrepancy from theory [35]. Instead, the split Hopkinson bar uses an incident bar that experiences minimal displacement and retains contact with the test sample, allowing for measurement of the longitudinal stress wave induced by the striker bar using condenser microphones [34]. The propagation speed of the pressure wave by the incident bar is dependent only on the material modulus of elasticity and density. The velocity of the striker bar can be used to derive the strain rates applied to the sample. The configuration of the apparatus prevents distortions caused by the striker bar from significantly affecting experimental results [34].

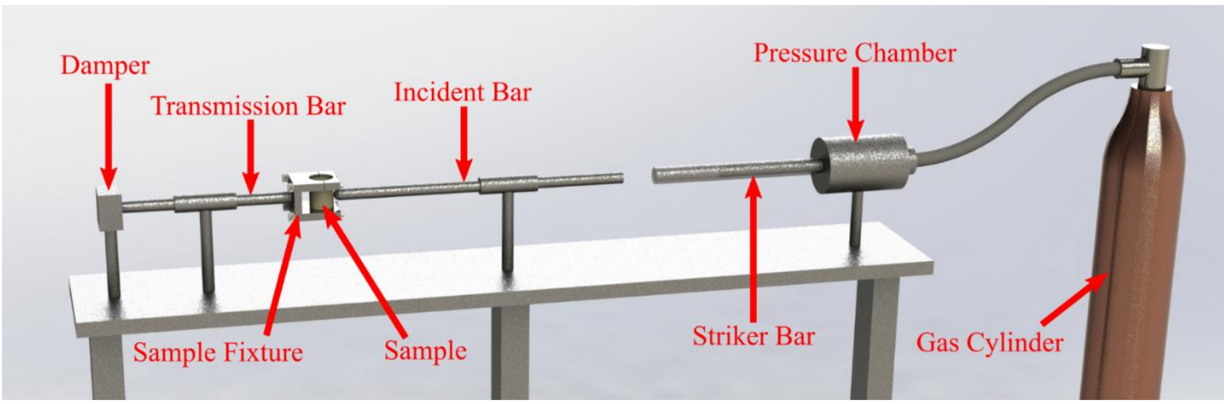

Figure 2-8: Schematic of a split Hopkinson pressure bar apparatus with a transversely mounted tubular braided composite sample.

Apart from its use in compressive impact testing, referred to as the SHPB [36], modifications exist to allow for other loading types, such as the split Hopkinson tensile bar (SHTB) [37], torsional split Hopkinson bar (TSHB) [38], and split Hopkinson shear bar (SHSB) [39]. A review of SHPB testing of braided composites is found in the following section.

2.3.3 Split Hopkinson Pressure Bar in Braided Composites

2.3.3.1 2D Braided Composites

Zhao et al. [40] investigated impact behaviour of 2D triaxially braided carbon/epoxy composite brick specimens. Braided fabrics with a braid angle of 60° with additional axial yarns were stacked in eight layers, then epoxy was applied by RTM to form panels, from which brick samples were cut to size. Both quasi-static and SHPB impact testing were performed to achieve a wide range of loading rates. Additionally, both longitudinal and transverse loading were investigated in this work. Under longitudinal loading, quasi-static testing caused fibre buckling, creating shear bands, whereas impact testing caused fibre shear fracture and delamination before buckling could occur. Under transverse loading, damage was instead primarily comprised of interface and matrix cracking.

2.3.3.2 3D Rectangular Braided Composites

Sun et al. [41] investigated the effects of applied strain rate on 3D braided E-glass/epoxy composites. The samples were manufactured using the four-step braiding method and RTM. Loading was applied in both the in-plane and out-of-plane directions, using impact tests by SHPB and quasi-static tests to achieve an extensive range of strain rates. The compressive stiffness was found to increase with strain rate throughout all test cases, indicating a clear strain rate sensitivity of the stress-strain curves. In contrast, the maximum stresses and strains did not have a clear correlation with strain rate. Additionally, for out-of-plane loading at higher strain rates, the compressive deformation that was seen universally was accompanied by shear deformation. However, no clear rupture was found for any sample in this work.

Gu and Chang [42] then applied energy absorption analysis in the frequency domain to the data from the previous work and found that the samples had higher energy absorption, and could absorb higher-frequency energy, at higher strain rates.

Sun and Gu [43] then performed the testing procedures from the previous works on similar materials, where vinyl ester replaced epoxy as the matrix material, and the size and velocity of the striker bar were increased to ensure failure of the samples. Here, ultimate compressive stresses were found to increase with strain rate, with equal sensitivities between the in-plane and out-of-plane loading directions. However, strains at failure decreased with increasing strain rate, especially when compared to quasi-static loading.

Sun et al. [44] investigated the stability of the 3D braided samples using Z-transforms and found that the material had increased stability with strain rate under out-of-plane loading but remained unstable under in-plane loading.

Li et al. [45] investigated the impact response of 3D5d carbon/phenolic braided composites with varying braid angles and fibre volume fractions. Loading was applied along the direction of braiding, referred to as the longitudinal direction. Macroscopic and microscopic fracture morphology of the samples was analyzed using a scanning electron microscope (SEM). The maximum stresses and failure strains were found to increase with strain rate, and the compressive moduli remained unaffected by strain rate. Additionally, based on fractographic data, fractures were found to be more brittle at higher strain rates, and failure consisted of cracking and debonding in the matrix material and local buckling and shear fracture in the fibre material.

Next, Li et al. [46] applied the methodology from the previous work to transverse loading of the same materials. Here, the maximum stresses increased with strain rate, and the failure strains and compressive moduli remained unaffected by strain rate. From fractographic analysis, failure occurred due to shearing of the matrix, fibre, and interface, as well as fibre tearing at the shear bands. Additionally, higher braid angles and fibre volume fractions caused increased sensitivity to strain rates and more prominent shear damage at higher strain rates.

Then, Li et al. [47] followed the previous work on longitudinal loading with further variation of braid angles and fibre volume fractions. At higher braid angles, the material became more susceptible to damage with manifesting shear failure modes in the matrix and fibre materials. At higher fibre volume fractions, the material experienced more severe and brittle fracture.

Zhang et al. [48] studied the transverse impact response of 3D braided carbon/epoxy composites manufactured to a significantly larger size. Boundary conditions in this study also varied from the previous works, such that samples were supported at their ends rather than sandwiched between the incident and transmission bars. At an impact velocity of 13.6 m/s, the sample did not fracture and experienced matrix cracking at its impacted face and fibre pullout at its opposite face. At higher impact velocities, fibre fracture became the dominant failure mode, resulting in ultimate fracture that exhibited a sawtooth profile, indicating shear failure through resin-rich areas. Total deflection of the samples also increased with impact velocity.

Zhang et al. [49] then employed frequency domain analysis on the data from the previous work and found that the stress amplitude increased with impact velocity, but the stress frequencies remained unchanged, concluding that the stress amplitudes are a primary determining factor for the expected failure modes of the materials.

Gao et al. [50] then developed a microscale FEA model to further assess the internal mechanisms of SHPB-based impact of 3D braided carbon/epoxy composites. Deformations were found to be more unevenly distributed with increasing strain rate, causing accelerated damage onset. Additionally, velocity gaps between the fibre and matrix materials were found to increase with strain rate, up to a maximum of 48 m/s due to interface debonding.

Zhao et al. [51] performed SHPB impact testing on 3D braided carbon/epoxy composites at three loading directions: longitudinal, transverse, and through-thickness. Samples were manufactured with varying braid angles to examine the effect of braid angle on impact properties in each loading direction. Gas gun pressures were also varied to examine strain rate sensitivity of the mechanical properties. The ultimate compressive strength of the material was found to increase with strain rate for all braid angles and all loading directions. This effect was most prevalent in longitudinal loading. Additionally, the through-thickness loading direction showed the most significant effect of the braid angle on the stress-strain curve, where a braid angle of 20° showed little strain recovery, while braid angles of 30° and 45° showed substantial strain recovery, resulting in a hysteresis curve profile.

Tan et al. [52] then followed the methodology from the previous work for samples with a 20° braid angle, then developed an FEA model for further compressive behaviour analysis. The compressive modulus and ultimate strength increased with strain rate, with the rate of increased being highest under longitudinal impact, followed by through-thickness, then transverse impact. Transverse mechanical properties were found to be further hindered by defects caused by sample machining, creating yarn discontinuity from a cut-edge effect. Between the combinations of loading direction and strain rate, numerical results correlated with only one experimental test case, due to the use of a simple linear elastic model.

Shi et al. [53] investigated impact fracture of 3D braided carbon/epoxy composite U-notch beams. Analyzed metrics included deformation and load progression, and crack mouth opening displacement. Impact testing was performed by SHPB at varying gas gun pressures. A solid epoxy U-notch beam was also tested for comparison of impact behaviours. In the composite beam, the crack was found to propagate in the direction of the angled braids, whereas in the solid epoxy beam, similarly to most isotropic materials, the crack propagated along the direction of impact, perpendicular to the beam cross-section.

Li et al. [54] examined the shear punch properties of braided 3D carbon/epoxy composites with varying thicknesses. Impact testing was performed using a modified SHPB setup, with a rectangular tip at the incident bar and a matching notch in the transmission bar. Damage morphology was qualitatively assessed by SEM imaging. With increased thickness, the punch shear modulus increased, but the total specific energy absorption decreased. From SEM examination, the primary damage modes were matrix cracking, fibre shear breakage, and fibre pullout.

Gao et al. [55] studied the damage mechanisms of 3D braided carbon/epoxy composite beams under multiple compressive impacts. Qualitative morphology analysis was done using images from high-speed cameras during testing. For the first impact, the material had the highest total energy absorption with interface damage and resin breakage being the primary mechanisms. For the second impact, the material had increased damage energy absorption but decreased total energy absorption, accounted primarily by fibre preform deformation and matrix debris. In both cases, the matrix absorbed the larger proportion of energy. For the third impact, energy absorption was minimal, and the fibres absorbed most of the energy instead.

Hu et al. [56] studied multiple impacts of 3D braided carbon/epoxy composite beams using varying braid angles and gas gun pressures. The beams were fixed at their ends and impacted transversely. At a braid angle of 20°, the beam demonstrated a low resistance to impact damage, stresses propagated rapidly through the thickness of the beam, and fibre fracture occurred as early as the second impact cycle. At a braid angle of 30°, the impact damage resistance was improved, and it took four impact cycles for fibre fracture to occur. At a braid angle of 40°, the beam demonstrated the highest resistance to impact damage, due to a larger number of points of interlaced yarns and sample thickness. Stresses were largely localized near the impact site, unlike what was observed for lower braid angles, where stresses propagated significantly in various directions.

Gao et al. [57] investigated multiple impacts of 3D braided carbon/epoxy composites under out-of-plane loading at varying braid angles. The sample with a 15° braid angle experienced linear elastic stress-strain behaviour followed by brittle fracture at the peak load. The samples with 26° and 37° braid angles experienced non-linear elastic stress-strain behaviour followed by ductile fracture past the yield point. Additionally, at a 15° braid angle, impact damaged followed a V-shaped profile, while for 26° and 37° braid angles, damage was uniformly distributed. Finally, the braid angle had significant effects on impact energy absorption by constituents at each impact cycle. At the first impact, fibre energy absorption increased braid angle due to the higher fibre volume fraction. At the second impact, fibre energy absorption decreased with increasing braid angle due to the change in load bearing capacity of the matrix due to the first impact. At the third impact, fibre energy absorption was the highest for the 26° braid angle.

Gao et al. [58] then applied the procedures from the previous work to multiple impacts of the samples under longitudinal loading. Here, at the first impact, the sample with a 15° braid angle experienced yarn and interface damage, while the samples with 26° and 37° braid angles experienced resin damage and interface debonding. At successive impacts, the sample with a 15° braid angle experienced significant fracture and dislocation of fibres, while the samples with 26° and 37° braid angles demonstrated improved structural integrity.

2.3.3.3 3D Circular Braided Composites

Zhou et al. [59] performed SHPB testing on 3D circular braided carbon/epoxy composites. Fibre preforms were manufactured by four-step circular braiding, then impregnated using the VARTM process. The circular samples were fixed at their ends, then impacted transversely at varying gas gun pressures. Peak load and energy absorption was found to increase with gas gun pressure, and the fibres endured higher stresses than the matrix. Stresses propagated from the impact site throughout both the circumference and the length of the sample, with much of the stress reaching the fixed ends. Furthermore, impact fracture was localized at the impact site in the form of concave deformation, matrix cracking, and fibre breakage, indicating the dominance of shear failure.

Zhou et al. [60] then tested the materials from the previous work in varying fibre configurations. Here, fibre preforms were manufactured in four-directional (3D4d) and five-directional (3D5d) configurations. Since the 3D5d samples had a higher linear density than the 3D4d samples, specific load and energy absorption were used as the comparing metrics between the two braiding configurations. The 3D5d samples were found to experience consistently higher specific loads and energy absorptions compared to the 3D4d samples due to the added axial fibres dispersing stresses much more quickly than the crimped fibres. As such, the 3D4d samples experienced more severe impact damage than the 3D5d samples.

Zhou et al. [61] then applied the same procedures from the previous works to the 3D4d circular braided composites, with variation of the number of radial layers. Here, an increase in layers increased peak load and energy absorption and decreased impact deflection. At the impact site, stresses were found to be compressive at the impacted side and tensile at the unimpacted side, while much of the remaining sample region was under tensile stress. Furthermore, damage morphology analysis showed that with 2 layers, the material fractured at the centre of the impact site and propagated outward in a star shaped profile, while with 3 or 4 layers, the material fractured around the edges of the impact site instead.

Zhou et al. [62] then applied the methodology from the previous works by testing the 3D4d circular braided composites with variation of both the number of layers and the braid angle. Additionally, µCT was used to capture the internal structures of the damaged samples and qualitatively assess damage mechanisms. At the highest impact velocity of 17 m/s, debonding between fibre yarns was found for all braid angles. However, at braid angles of 15° and 30°, the samples experienced fibre fracture, and cracks propagated along the length of the sample. In contrast, at a braid angle of 45°, fibre tow splitting was found to occur instead, and cracks propagated along the direction of impact. Furthermore, the fibre structure had increased rigidity with increasing braid angles, due to the increased number of yarn interlacing points.

Wu et al. [63] applied SHPB impact loading to 3D circular braided carbon/epoxy composites with varying angles under axial loading. A mesoscale FEA model was developed to further investigate the damage mechanisms. Specific energy absorption from axial impact increased with strain rate, with increased strain-rate sensitivity at decreasing braid angles. Impact damage initiation showed good correlation between experimental and FEA results. Stresses from FEA correlated well with experiments at lower strains but were significantly underestimated at higher strains.

Liu et al. [64] applied an investigation of defects to the FEA approach in the previous work with an aim to improve correlation of impact response with the same experimental results. Fibre breakages and matrix voids were generated randomly within the model to represent realistic manufacturing defects. As an example, for the 25° braid angle, the ideal model showed highly localized damage at the surface supported by the transmission bar. In contrast, the addition of fibre defects caused a shear band, which correlated well with experiments. However, an increase in matrix defects caused some divergence from experimental results, demonstrating the importance of limiting the matrix void content in the numerical model.

2.3.3.4 3D Braided Composites with Complex Geometries

Zhou et al. [65] studied the impact response of 3D-braided carbon/epoxy composite I-beams. The preforms were impregnated by VARTM using a custom four-part mold. The beams were fixed at the ends and impacted transversely at a flange. The complex geometry created complex stress distributions, and failure was concentrated at the junction point between the impacted flange and the web.

2.3.3.5 Summary

The current literature on SHPB testing of braided composite is summarized in Table 2-2. While many of the works outlined above examined various forms of 3D braided composites, there is very limited study on SHPB impact testing on 2D braided composites. 3D braided composites have a structural advantage over 2D braided composites, as 3D braid architectures provide through-thickness reinforcement, allowing for high impact resistance and applicability of the SHPB method. Furthermore, flat geometries are commonly tested in these works as they do not require significant modification of test procedures. Other geometries such as circular braids and I-beams were tested after sufficiently modifying the SHPB test. Additionally, the materials used in these works used a singular material per phase, with carbon as the most common reinforcement and epoxy as the most common matrix. The lack of study on the use of multiple materials per phase creates a significant gap in the analysis of hybrid braided composites by SHPB. Finally, assessment of internal structures of braided composites is limited, with Zhou et al. [62] using μCT to qualitatively assess impact damaged structures. Furthermore, there is a gap in quantitative analysis between damage states of braided composites.

Table 2-2: Summary of literature for SHPB testing of braided composites.

Authors	Braid Architecture	Fibre Material	Matrix Material
Zhao et al. [40]	2D Triaxial Flat	Carbon	Epoxy
Sun et al. [41], [44]	3D Flat	E-Glass	Epoxy
Gu and Chang [42]	3D Flat	E-Glass	Epoxy
Sun and Gu [43]	3D Flat	E-Glass	Vinyl Ester
Li et al. [45]–[47]	3D Flat	Carbon	Phenolic
Zhang et al. [48], [49]	3D Flat	Carbon	Epoxy
Gao et al. [50], [55], [57], [58]	3D Flat	Carbon	Epoxy
Zhao et al. [51]	3D Flat	Carbon	Epoxy
Tan et al. [52]	3D Flat	Carbon	Epoxy
Shi et al. [53]	3D Flat	Carbon	Epoxy
Li et al. [54]	3D Flat	Carbon	Epoxy
Hu et al. [56]	3D Flat	Carbon	Epoxy
Zhou et al. [59]–[62]	3D Circular	Carbon	Epoxy
Wu et al. [63]	3D Circular	Carbon	Epoxy
Liu et al. [64]	3D Circular	Carbon	Epoxy
Zhou et al. [65]	3D I-Beam	Carbon	Epoxy

2.4 Damage Analysis of Composite Structures

2.4.1 Non-Destructive Testing Methods

FRP composites have been shown to contain various defects throughout the material life cycle. Material defects are a consequence of material constituent properties, manufacturing processes, and in-service conditions [66]. As shown in Figure 2-9, some of the most prevalent defects in composites include voids and pores (a), fibre misalignment and ply wrinkling (b), ply delamination and interface debonding, and impact damage (c). Due to the significant effect of defects on the mechanical properties of composite materials, thorough and reliable analysis becomes more challenging for composites than for traditional materials due to added uncertainty [67]. In pursuit of this goal, numerous works employed various forms of NDT to quantify the effects on material performance in the presence of such defects.

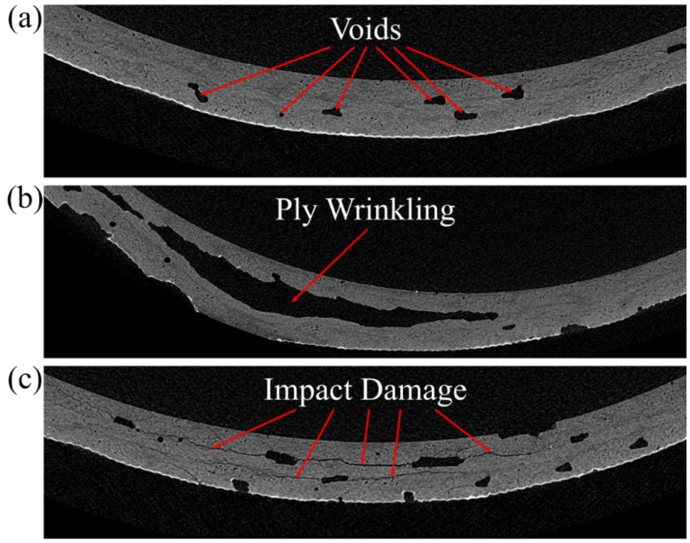

Figure 2-9: Common defects in composites: (a) voids formed in the matrix material after curing; (b) ply wrinkling from the hand lay-up process; (c) material cracking from applied impact damage.

Some NDT techniques that were used in FRP composites evaluation include acoustic wave-based techniques such as acoustic emission [68] and ultrasonic testing [69]; electromagnetism-based techniques such as infrared thermography [70]; and imaging-based techniques such as X-ray CT [71]. The following section reviews CT and its applications in composites.

2.4.2 Fundamentals of Computed Tomography

CT is an extension of conventional X-ray radiography, where 2D X-ray images of an object of interest are acquired at many angular orientations, such that the projections can be reconstructed into a 3D volume. The CT technique has one of its most impactful applications in medical imaging, with the first clinical scan performed on the head of a patient in 1971 [72].

Fundamentally, as shown in Figure 2-10, CT uses an X-ray source to generate X-ray beams that pass through a test sample and reach an X-ray detector at the opposite end. The detector measures intensity of the X-rays attenuated by the material of the test sample to generate a 2D image that represents the projection of the sample normal to the principal axis of the source and detector.

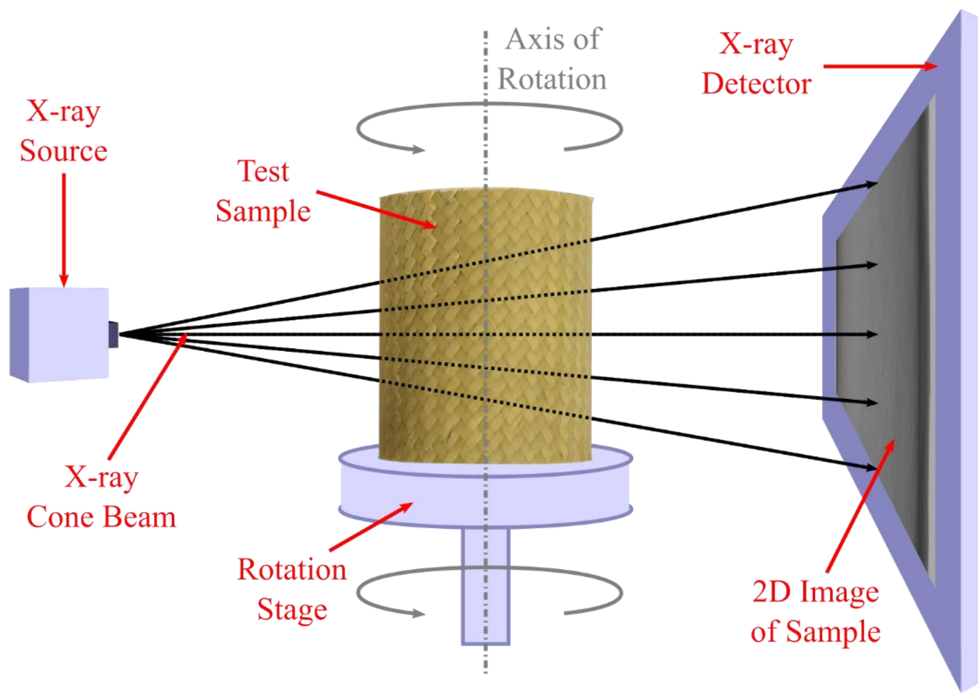

Figure 2-10: Schematic of the working principles of CT. The process is illustrated for µCT of a braided composite material.

CT makes use of the ability of different materials to absorb or scatter X-ray radiation [73]. For light generated by a source with intensity I_0 passing through a material with light attenuation coefficient μ and thickness L, the intensity of light received by a detector I is given by Equation 1, referred to as the Beer-Lambert law [73]. Consequently, 2D mappings of light received by the detector indicate the presence of various materials of various thicknesses at each projection.

$$I = I_0 e^{-\mu L} \tag{1}$$

To obtain a volumetric representation of a sample, CT images are acquired at many angular orientations of a sample, then reconstructed using an algorithm, either by direct means such as filtered back projection or direct Fourier inversion, or by iterative means [74]. As shown in Figure

2-11, the objective of the reconstruction algorithm is to convert a set of sample projections along the radial and height axes into a stack of image slices along the Cartesian axes that form the volume of the sample when assembled. The smallest element of the volume is defined as a voxel, which is the 3D equivalent to the pixel of a 2D image.

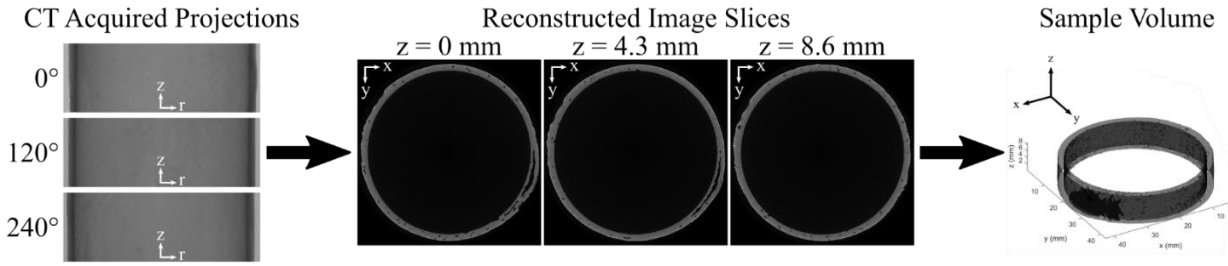

Figure 2-11: Illustration of the image reconstruction process for CT. Projections of a sample along the r-z axes are converted into slices of the sample along the x-y axes. The stack of slices is then assembled to form the sample volume.

µCT is a form of the CT technique that is used particularly for high-resolution volumetric scanning and characterization of materials at a relatively small scale [74]. This process can be performed ex-situ, where scanning is performed separately from mechanical testing, or in-situ, where mechanical testing is performed within the apparatus. Whereas medical CT uses a rotating gantry containing the X-ray source and detector at opposite ends from a stationary patient, µCT uses a stationary X-ray source and detector located at opposite ends from a rotating sample as shown in Figure 2-10. For example, the SkyScan 1272 as shown in Figure 2-12 is a µCT apparatus that consists of a 10-watt X-ray source, a 16-megapixel detector, and a rotation stage that contains the sample and rotates at controlled increments for acquisition of each X-ray image. This apparatus can be used for objects with a maximum diameter of 75 mm and a maximum height of 80 mm.

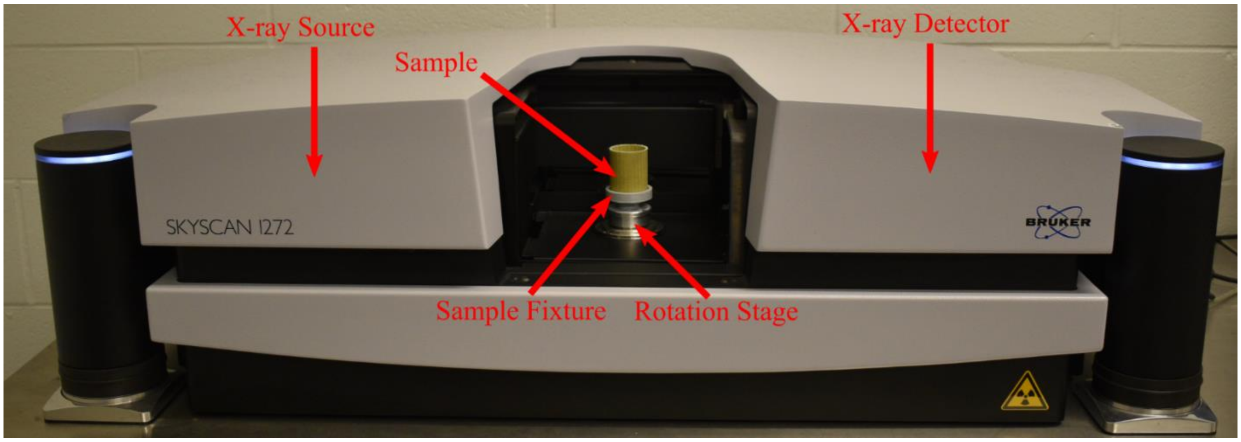

Figure 2-12: SkyScan 1272 μCT apparatus with a tubular braided composite sample on a rotation stage.

Distinct features are extracted using image segmentation, most commonly performed using the image histogram, which plots counts of image pixels based on light intensity [74]. A simple image segmentation process known as image binarization is illustrated in Figure 2-13. From the reconstructed image slice shown in Figure 2-13(a), the image histogram shown in Figure 2-13(b) is generated, and used to select a threshold to create the binarized image shown in Figure 2-13(c), where pixels of lower intensity are set to zero and pixels of higher intensity are set to one.

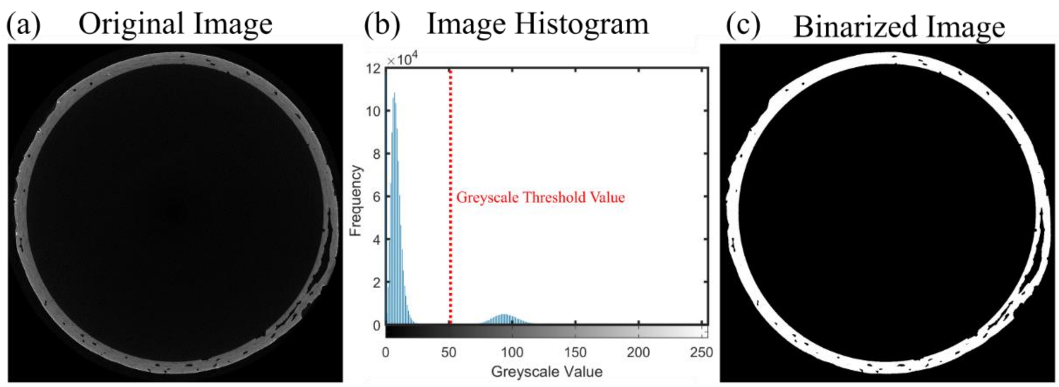

Figure 2-13: Illustration of image binarization for feature segmentation: (a) original 8-bit image; (b) image histogram with the threshold value selected between the two greyscale value peaks; (c) resultant binarized image.

These principles have allowed extensive application of µCT to the study of composite materials, due to the ability to distinguish between material constituents as well as defects. Using µCT, individual fibres and the fibre distribution of a preform can be assessed [75], structures of void networks can be quantified [76], and internal damage such as microcracks and macrocracks can be identified and investigated [77]. Furthermore, µCT can be used to obtain overall geometries of composites that can be used as a reference for analytical models [24], [25].

2.4.3 Computed Tomography for Analysis of Composites

2.4.3.1 Geometry Assessment of Composites

Düreth et al. [78] assessed initial yarn and cross-sectional geometry of textile carbon/epoxy composite combined loading samples using imaging techniques including in-situ CT. Here, average mesoscale properties such as undulation, crimp angle, and ply thickness were sufficiently characterized from CT imaging. However, the voxel size of 20 µm did not allow for yarn segmentation and individual yarn analysis. This local microscale analysis was done using micrographs instead.

2.4.3.2 Quantification of Voids in Composites

Ao et al. [79] studied the internal structure of a large woven ceramic matrix composite plate through CT within a limited region of interest (ROI). The work found that a voxel size of 28.4 microns was sufficient in capturing the extent of voids in the material. The porosity within the ROI was evaluated to be around 13% and the voids typically formed clear boundaries with the fibre tows. Fibre weave defects, which occurred often at sharp internal edges of the sample, contributed locally to an increase in void content.

Ayadi et al. [80] studied the internal structures of weft-knitted glass/PP composites under varying manufacturing conditions to control porosity. Panels were manufactured by staged consolidation using compression molding at varying compression ratios. It was found that with no compression, the matrix material coalesced and bridged between tows, forming voids within tows. Additionally, at a high compression ratio of 63%, the matrix material formed clusters within confined regions between fibre tows, resulting in poor impregnation of knitting yarns, especially at looping sections. The optimal impregnation quality was found in samples with intermediate compression ratios between 35% and 47%, allowing for more uniform flow of matrix material within the knitted fabric.

2.4.3.3 Quantification of Damage Cracks in Composites

Schöttl et al. [81] performed crack segmentation for quantitative analysis of in-situ µCT of cyclic load testing of a discontinuous glass fibre reinforced hybrid thermoset composite notched sample. The cracks were segmented using seeded region growing, a technique developed by Adams and

Bischof [82] that separates regions by greyscale intensity values defined by seed voxels. Here, since an in-situ configuration was used and the damage cracks were significantly larger than any material voids, the crack volume fraction could be reliably determined at each load step after noise filtering within the notch. Crack volume fractions of the sample remained at around 0.02% after three load steps, then increased to nearly 0.10% after the fourth load step.

Schöttl et al. [83] then extended the work from the previous study by applying an empirical second-order crack orientation tensor to the segmented cracks. After the first three load steps, the tensors indicated that the principal crack consistently aligned with the direction of loading. After the fourth load step, the crack orientation had shifted by around 30° transversely.

Ziółkowski et al. [84] performed mesoscale and macroscale CT for ballistic testing of woven aramid reinforced polymer composite panels. Samples were manufactured using either polyethylene (PE) or PP as the matrix material. Ballistic testing was performed using 0.38 calibre and 9 mm × 19 mm calibre projectiles, applying 392 J and 548 J of impact energy respectively. Mesoscale CT allowed for statistical analysis of pre-existing voids including volume and sphericity and found that voids in the PP matrix sample were more circular overall than those in the PE matrix sample. Macroscale CT showed the extent of large-scale delamination within the panels after ballistic testing and showed that, for the PP matrix sample, the higher-energy projectile caused a lower percentage of delamination due to the less significant spread of deformation around the impacted site.

Guo et al. [85] performed quasi-static tensile testing and tension-tension fatigue testing on 3D woven carbon/epoxy composites, using synchrotron radiation CT for volumetric damage analysis. Cuboid sections of damaged samples were prepared for scanning by waterjet cutting and polishing. All regions within the cuboid dimensions with low greyscale intensity were quantified as sample damage. Results from quasi-static testing showed that breakage of both warp and binder yarns occurred towards the edges of the weft yarn cross-section, as the highest undulation angles occurred at these positions. Results from fatigue testing showed that at the first stage, cracks manifested in resin-rich areas and propagated transversely. At the second stage, interface debonding became more prevalent as the matrix cracks continued to propagate. At the third stage, significant breakage occurred at the warp and binder yarns.

2.4.3.4 In-Situ Investigation of Effects of Voids on Damage of Composites Under Loading

Böhm et al. [86] used in-situ CT to investigate three different materials and the evolution of damage under loading and unloading. Two carbon/epoxy samples: one with non-crimp carbon fabric and one with weft woven carbon fabric, underwent in-plane tensile testing. One carbon/carbon sample underwent out-of-plane compressive testing. The in-situ testing guaranteed the alignment of datasets between scans. For the non-crimp carbon/epoxy sample, the combined length of cracks was consistently higher under loading compared to after unloading due to the partial closure of cracks. Similarly, for the weft woven carbon/epoxy sample, the delamination area was higher under loading than after unloading. For the compressed carbon/carbon sample, the void content decreased consistently under loading. However, after unloading, void content did not experience a significant decrease unless sufficient loading had been applied to induce plastic deformation. The study concluded that quasi-static damage analysis of composite materials would highly benefit from in-situ CT scanning under loading, as certain critical damage indications could become hidden after unloading.

Protz et al. [87] investigated the effects of void content in the tensile performance of glass/epoxy non-crimp fabric composites through in-situ CT. Samples were manufactured by VARTM with varying conditions to systematically induce void contents ranging from 0.01% to nearly 3%. It was found that crack growth was not much more prevalent in samples with low void content than in those with negligible void content. For samples with high void content, cracks propagated more easily from voids with thin, sharp profiles, but were more likely to be stopped by nearby spherical voids.

Hülsbusch et al. [88] investigated the evolution of damage in fatigue testing of glass fibre reinforced composites through in-situ CT. Samples were manufactured from glass/epoxy and glass/polyurethane in quasi-isotropic laminate configurations. Fatigue testing was performed in a high cycle regime using a servohydraulic testing apparatus, as well as a very high cycle regime using a resonant testing apparatus for a higher loading frequency. It was found that the glass/polyurethane samples had consistently lower fatigue strength than the glass/epoxy but had a lower concentration of visible material damage to failure. However, much of the damage in the glass/epoxy consisted of inter-fibre cracking. In contrast, the glass/polyurethane, which was found to have a higher pore content than the glass/epoxy, also had proportionally higher delamination which was thereby deduced as a leading cause of decreased fatigue strength.

Zeng et al. [89] performed in-situ µCT in shear testing of woven glass/epoxy flat laminates. Void segmentation and statistical characterization was performed using an algorithm developed in MATLAB. Crack segmentation was performed to characterize the various forms of shear damage as they developed. Classification of cracks was based on the clear distinction between warp and weft yarns due to the flat cross-section of the samples, which was leveraged here to distinguish between longitudinal and transverse cracking at warp and weft yarns.

2.4.3.5 Coupled Analysis of Internal Damage and Surface Measurements

Holmes et al. [90] performed tensile testing on plain woven carbon/PEEK composites and assessed damage by coupling µCT with surface measurements by digital image correlation (DIC). Samples were cut by waterjet at various orientations, including on-axis (0°) and off-axis (15°, 30°, and 45°). Here, μCT analysis found that 0° and 15° samples experienced minimal internal cracking, with any identified cracks remaining confined within tows. In contrast, the 30° and 45° samples experienced significant internal cracking that frequently extended across tow cross-sections. The μCT data was successfully correlated with DIC data, illustrating the effects of internal damage on surface strains.

2.4.3.6 Summary

There has been significant study on geometry, voids, and cracks in composites, although the focus typically remained on one type of feature. Coupled analysis of voids and cracks has been performed using in-situ μCT which ensures alignment of datasets at each loading stage. There remains a significant gap in the coupled study of different features in composites using ex-situ μCT, which is applicable to loading scenarios that require large-scale apparatus such as impact testing.

2.4.4 Digital Volume Correlation

DVC is a volumetric optical measurement technique that is primarily used for volumes reconstructed from μCT imaging. This technique is analogous to DIC, where in DIC, deformations of a sample are measured at a surface, while in DVC, deformations are measured within a volume [91]. DVC uses two volume datasets, typically an unloaded or undamaged sample as a reference and a loaded or damaged sample as a target. The primary objective of this technique is to evaluate local 3D deformations and strains throughout a volume, including its internal features [92]. DVC is often performed using local approaches, where volumes are split into subsets which are analyzed individually [93]. Additionally, DVC measurements can be improved by particle seeding, where high-contrast particles are incorporated into a material to create distinct subset features and reduce uncertainty in the correlation process [94]. A local approach to DVC is illustrated for a single subset in Figure 2-14.

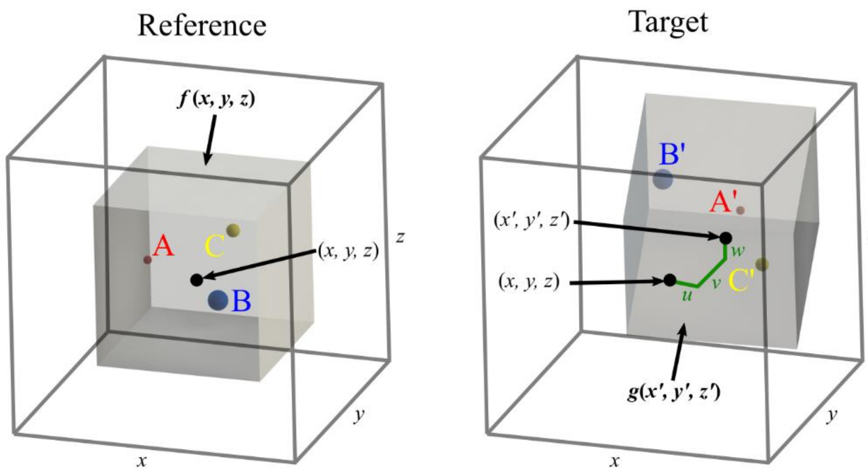

Figure 2-14: Illustration of the DVC process. Identifying geometries that match between the reference and target allow for identification of the necessary transformations for pattern matching.

For a given subset, its displacement is determined by measure of a correlation metric between reference and target volumes [95]. At the voxel level, cross-correlation is a commonly used metric for pattern matching and achieving displacement measurements [96]. For a reference volume f and target volume g with an offset vector of $[u, v, w]$, the normalized cross-coefficient r is defined by Equation 2 [97]. The displacement vector of a subset is defined as the offset vector where the cross-correlation criterion is maximized [93]. An example of this process is provided in Figure 2-15, where the DVC algorithm correlates subsets between the reference (a) and target (b) volumes to generate measurements such as displacement magnitudes (c).

$$r = \frac{\sum_{x,y,z}\left[f(x,y,z) - \bar{f}\right]\left[g(x+u, y+v, z+w) - \bar{g}_{u,v,w}\right]}{\sqrt{\sum_{x,y,z}\left[f(x,y,z) - \bar{f}\right]^2 \sum_{x,y,z}\left[g(x+u, y+v, z+w) - \bar{g}_{u,v,w}\right]^2}} \tag{2}$$

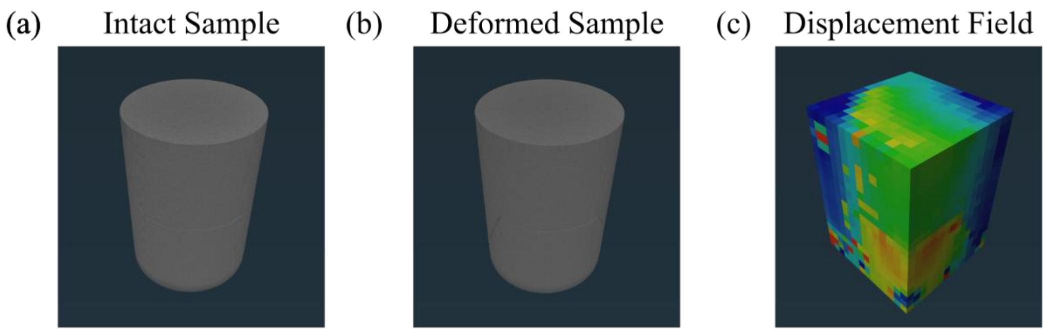

Figure 2-15: Example of the DVC process: (a) intact sample volume as the reference; (b) deformed sample volume as the target; (c) field of local displacement magnitudes generated by DVC. Data provided by Tudisco et al. [98]**.**

Mazars et al. [99] performed in-situ µCT in tensile testing of 3D woven ceramic matrix composites. Samples were manufactured with silicon carbide fibres and silicon carbide matrix using the melt infiltration process. Tensile testing was performed at room temperature and at 1250°C. DVC was also performed for more localized analysis of damage. Cracks in the material during testing were difficult to characterize from the reconstructed µCT images alone, but residuals from DVC showed the cracks clearly. Matrix cracking first developed along the weft fibres, after which they merged by through-thickness cracking. Fibre breakages outside of the ultimate failure crack occurred much more frequently at room temperature than at high temperature.

Lorenzoni et al. [100] studied the damage evolution of strain hardening cement composites using in-situ µCT. Tensile and compressive testing samples were manufactured from polyethylene microfibre reinforced cement, where the compressive samples had either longitudinally or transversally oriented fibres. Additionally, DVC was performed for the compressive samples to investigate normal strain and deformation profiles. From the qualitative assessment of μCT data, it was found for both the tensile and compressive samples that notches and pores were major contributors to the localization of damage and failure. However, the authors suggested that using larger samples may provide more representative findings due to statistical features. Strain maps of compressive samples from DVC showed a significant presence of strain concentrations in porous regions of the sample, thereby confirming the locations of failure initiation.

Liu et al. [101] performed in-situ μCT and DVC analysis of 3D braided silicon carbide/silicon carbide composites under three-point bending. Image subtraction was performed in the μCT reconstructed images to isolate newly created damage at each load step. Principal strain measurements from DVC indicated that at the first and second load steps, a periodic strain profile indicative of the 3D braid pattern was found, and small stress concentrations appeared at the compressive and tensile surfaces. Significant damage ensued at the third and fourth load steps, resulting in a large strain concentration at the compressive surface that propagated through the length of the sample. This observation agreed with the findings from segmented cracks in the reconstructed volumes, which showed that cracks propagated mainly along the direction of the fibre tows.

Holmes et al. [102] performed ex-situ μCT and DVC analysis for load relaxation tensile testing of woven glass/propylene composites. Tensile loading was applied to a sample along the warp direction and another in the weft direction, up to 90% of the ultimate extension prior to release. Samples were scanned before and after loading, after which a 3D rigid registration was applied to ensure appropriate characterization of damage through DVC. Qualitative μCT investigation showed that for the warp loaded sample, damage manifested as longitudinal delamination cracking constrained to an edge of the sample. This finding was confirmed quantitatively by a clear out-of-plane strain concentration as measured from DVC. In contrast, for the weft loaded sample, µCT images showed internal transverse cracking in fibre-rich areas formed by poor resin impregnation in the hot compaction process. Additionally, DVC measurements showed a significantly larger proportion of out-of-plane strain for the weft loaded sample, which was largely attributed to the ductility of the matrix material rather than internal damage.

Goyal and Melenka [103] studied 2D braided hybrid carbon-aramid/epoxy flat samples under tensile loading using in-situ µCT. The material configuration used an intra-ply hybrid textile of carbon and aramid tows. Additionally, the effects of particle seeding in strain measurements were examined. For these samples, peak strain values were found to be 1.7% in tension along the axial direction, and 6.5% in compression along the transverse direction. Furthermore, the absence of seeded particles resulted in poor correlation in over 50% of the subsets, whereas particle seeding reduced this proportion to below 15%.

From the reviewed literature on DVC, there is limited study on DVC of hybrid braided composites as most works used singular materials per phase. Additionally, there remains a gap in DVC analysis using ex-situ µCT for composites, particularly for use with impact testing. DVC is applicable to impact testing, as it can measure the induced permanent material damage in the form of strain. DVC is also directly comparable to FEA due to its discrete nature and can be used to validate FEA models of impact tested structures. Experimental measurements from DVC can provide valuable insight for validating numerical models of hybrid braided composites to help accelerate the design of materials and structures.

2.5 Gaps in Literature

When considering impact testing of braided composites, particularly using the SHPB apparatus, it is noted that most works that exist to date focus solely on 3D braided composites, which have substantially higher impact resistance compared to 2D braided composites, owing to the influence of additional interaction of fibre tows along the through-thickness direction. SHPB testing of 2D braided composites is limited to testing of specimens with flat cross-sections, as performed in the work by Zhao et al. [40]. Impact testing of 2D braided composites was also performed by drop-weight testing [28], [29], [32] and direct pressure gas gun testing [33], with the works of Shi et al. [28] and Wu et al. [32] focusing on hybrid configurations of braid architectures. However, these studies used uniform fibre and matrix materials, and hybrid configurations of materials were not focused.

Concerning CT analysis of composites, many of the works examined either quasi-static or cyclic loading of samples. The use of CT for dynamic testing of composites, particularly by SHPB impact, is limited to qualitative post-damage inspection of 3D circular braided composites, as studied in the work by Zhou et al. [62]. Additionally, the study of crack development alongside voids and pores was performed using in-situ CT techniques, thereby ensuring the alignment of datasets between unloaded and loaded samples without the need for image registration after scanning. Dynamic testing was not used in these studies, likely due to the concern of feasibility of direct coupling of large impact testing apparatus with X-ray CT scanning equipment. Studies with a focus on DVC have also largely used in-situ µCT for non-hybrid composites, with the exceptions of Holmes et al. [102] who employed ex-situ µCT of glass/propylene composites for quasi-static tensile load-relaxation testing, and Goyal and Melenka [103] who employed in-situ µCT of intra-ply hybrid carbon-aramid/epoxy composites for tensile testing.

It is concluded from the review of the literature that there remains much room for study of the impact behaviours of 2D braided composites and hybrid material composites, as well as internal impact damage and strain behaviours of composites. These gaps demonstrate the need for a method of rapid quantification of voids and damage in braided composites, particularly using automated processes based on computational algorithms.

2.6 Proposed Study

To address the gaps in literature, the author proposes the study in the following chapter with the objective of assessing the internal impact response of a 2D braided composite tube with an inter-ply hybrid material configuration. The tubular sample is fixed at its ends and impact loading is applied transversely. Volumetric data of the sample is acquired before and after impact damage by ex-situ μCT. Image registration is performed to align the volume of the damaged sample with the undamaged sample. Material voids are segmented and matched between the two volumes by an algorithm, then analyzed individually and compared statistically. Impact damage cracks are extracted by an algorithm based on identifying object shape properties and assessed in the context of the full scan volume. Finally, the μCT analysis is supplemented with a DVC study, where volumetric strains are measured for correlation with the cracks identified by image processing and any additional damage modes.

2.7 References

[1] H. V. S. GangaRao and W. Prachasaree, *FRP Composite Structures*. Boca Raton: CRC Press, 2021. doi: 10.1201/9781003196754.

[2] C. Soutis, “Carbon fiber reinforced plastics in aircraft construction,” *Materials Science and Engineering A*, vol. 412, no. 1–2, pp. 171–176, Dec. 2005, doi: 10.1016/j.msea.2005.08.064.

[3] G. Neşer, “Polymer based composites in marine use: History and future trends,” in *Procedia Engineering*, Elsevier Ltd, 2017, pp. 19–24. doi: 10.1016/j.proeng.2017.08.111.

[4] S. Ramakrishna, J. Mayer, E. Wintermantel, and K. W. Leong, “Biomedical applications of polymer-composite materials: a review,” *Compos Sci Technol*, vol. 61, no. 9, pp. 1189–1224, Jul. 2001, doi: 10.1016/S0266-3538(00)00241-4.

[5] X. Lyu, “Influence of High-Performance Composite Sports Equipment on Brand International Sports Marketing Strategy,” *Advances in Materials Science and Engineering*, vol. 2022, 2022, doi: 10.1155/2022/3959628.

[6] S. Sharma, *Composite Materials*. CRC Press, 2021. doi: 10.1201/9781003147756.

[7] V. V. Vasiliev, *Mechanics of Composite Structures*. CRC Press, 2017. doi: 10.1201/9780203747858.

[8] J. P. Carey, “Introduction to braided composites,” in *Handbook of Advances in Braided Composite Materials: Theory, Production, Testing and Applications*, Elsevier Inc., 2017, pp. 1–21. doi: 10.1016/B978-0-08-100369-5.00001-5.

[9] A. C. West and D. O. Adams, “Effects of yarn crimping on compressive strength design allowables of braided composites,” in *Proceedings of the American Society for Composites*, 1996, pp. 999–1006. [Online]. Available: https://www.scopus.com/inward/record.uri?eid=2-s2.0-0030368622&partnerID=40&md5=58fea5f001037f02a01a612a1a0c777a

[10] A. Armanfard and G. W. Melenka, “Experimental evaluation of carbon fibre, fibreglass and aramid tubular braided composites under combined tension–torsion loading,” *Compos Struct*, vol. 269, Aug. 2021, doi: 10.1016/j.compstruct.2021.114049.

[11] G. W. Melenka *et al.*, “Manufacturing processes for braided composite materials,” in *Handbook of Advances in Braided Composite Materials*, Elsevier, 2017, pp. 47–153. doi: 10.1016/B978-0-08-100369-5.00003-9.

[12] C. M. Pastore, J. P. Carey, F. K. Ko, G. W. Melenka, and A. J. Hunt, “Design of braided composite materials,” in *Handbook of Advances in Braided Composite Materials: Theory, Production, Testing and Applications*, Elsevier Inc., 2017, pp. 365–394. doi: 10.1016/B978-0-08-100369-5.00010-6.

[13] K. Bilisik, “Braiding and Recent Developments,” in *Fibres to Smart Textiles*, A. Patnaik and S. Patnaik, Eds., Boca Raton : Taylor & Francis, a CRC title, part of the Taylor & Francis imprint, a member of the Taylor & Francis Group, the academic division of T&F Informa, plc, [2020] | Series: Textile Institute professional publications: CRC Press, 2019, pp. 131–152. doi: 10.1201/9780429446511.

[14] C. Ayranci and J. Carey, “2D braided composites: A review for stiffness critical applications,” *Compos Struct*, vol. 85, no. 1, pp. 43–58, Sep. 2008, doi: 10.1016/j.compstruct.2007.10.004.

[15] R. Kamiya, B. A. Cheeseman, P. Popper, and T.-W. Chou, “Some recent advances in the fabrication and design of three-dimensional textile preforms: a review,” *Compos Sci Technol*, vol. 60, no. 1, pp. 33–47, Jan. 2000, doi: 10.1016/S0266-3538(99)00093-7.

[16] K. Bilisik, “Three-dimensional braiding for composites: A review,” *Textile Research Journal*, vol. 83, no. 13, pp. 1414–1436, 2013, doi: 10.1177/0040517512450766.

[17] V. M. Karbhari, P. J. Falzon, and I. Herzberg, “Energy Absorption Characteristics of Hybrid Braided Composite Tubes,” *J Compos Mater*, vol. 31, no. 12, pp. 1164–1186, Jun. 1997, doi: 10.1177/002199839703101201.

[18] G. L. Farley, R. K. Bird, and J. T. Modlin, “The Role of Fiber and Matrix in Crash Energy Absorption of Composite Materials,” *Journal of the American Helicopter Society*, vol. 34, no. 2, pp. 52–58, Apr. 1989, doi: 10.4050/JAHS.34.2.52.

[19] G. Zumpano, M. Fox, W. J. Stronge, and M. P. F. Sutcliffe, “Impact damage in hybrid braided twill composites,” *J Mater Sci*, vol. 43, no. 20, pp. 6668–6675, Oct. 2008, doi: 10.1007/s10853-008-2880-y.

[20] A. E. H. Love, “XVI. The small free vibrations and deformation of a thin elastic shell,” *Philos Trans R Soc Lond A*, vol. 179, pp. 491–546, Dec. 1888, doi: 10.1098/rsta.1888.0016.

[21] G. W. Melenka, C. M. Pastore, F. K. Ko, and J. P. Carey, “Advances in 2-D and 3-D braided composite material modeling,” in *Handbook of Advances in Braided Composite Materials: Theory, Production, Testing and Applications*, Elsevier Inc., 2017, pp. 321–363. doi: 10.1016/B978-0-08-100369-5.00009-X.

[22] J.-H. Byun, “The analytical characterization of 2-D braided textile composites,” *Compos Sci Technol*, vol. 60, no. 5, pp. 705–716, Apr. 2000, doi: 10.1016/S0266-3538(99)00173-6.

[23] X. Ji *et al.*, “Multi-scale simulation and finite-element-assisted computation of elastic properties of braided textile reinforced composites,” *J Compos Mater*, vol. 48, no. 8, pp. 931–949, Apr. 2014, doi: 10.1177/0021998313480198.

[24] A. Gholami and G. W. Melenka, “Finite element analysis of 2-D tubular braided composite based on geometrical models to study mechanical performances,” *Mechanics of Advanced Materials and Structures*, vol. 29, no. 28, pp. 7542–7558, 2022, doi: 10.1080/15376494.2021.2001879.

[25] A. Gholami and G. W. Melenka, “Studying the geometrical models of tubular braided composite using micro computed tomography and particle swarm optimization,” *Compos B Eng*, vol. 260, Jul. 2023, doi: 10.1016/j.compositesb.2023.110758.

[26] M. W. Czabaj, M. L. Riccio, and W. W. Whitacre, “Numerical reconstruction of graphite/epoxy composite microstructure based on sub-micron resolution X-ray computed tomography,” *Compos Sci Technol*, vol. 105, pp. 174–182, Dec. 2014, doi: 10.1016/J.COMPSCITECH.2014.10.017.

[27] S. R. Abid, G. Murali, J. Ahmad, T. S. Al-Ghasham, and N. I. Vatin, “Repeated Drop-Weight Impact Testing of Fibrous Concrete: State-Of-The-Art Literature Review, Analysis of Results Variation and Test Improvement Suggestions,” *Materials*, vol. 15, no. 11. MDPI, Jun. 01, 2022. doi: 10.3390/ma15113948.

[28] L. Shi, Z. Wu, X. Cheng, Z. Pan, and Y. Yuan, “Transverse impact response of hybrid biaxial/uniaxial braided composite tubes,” *Eng Struct*, vol. 244, Oct. 2021, doi: 10.1016/j.engstruct.2021.112816.

[29] H. Na, L. Trueba, and B. H. You, “A Study of the Mechanical Properties of Biaxial and Triaxial Braided Composites for an Automotive Propeller Shaft,” *Fibers and Polymers*, vol. 23, no. 9, pp. 2712–2718, Sep. 2022, doi: 10.1007/s12221-022-0061-2.

[30] J. Guo, Y. Ke, Y. Wu, B. Gu, and B. Sun, “Effects of defect sizes at different locations on compressive behaviors of 3D braided composites,” *Thin-Walled Structures*, vol. 179, Oct. 2022, doi: 10.1016/j.tws.2022.109563.

[31] Q. Wang, X. Gao, M. Hu, B. Gu, and B. Sun, “A novel braiding method and impact behaviors of 3-D braided composite three-way integrated circular tubes,” *Compos Struct*, vol. 304, Jan. 2023, doi: 10.1016/j.compstruct.2022.116451.

[32] Z. Wu, K. Wang, L. Shi, X. Cheng, and Y. Yuan, “Low-velocity impact response and damage tolerance of hybrid biaxial/triaxial braided composite laminates,” *Polym Compos*, Mar. 2023, doi: 10.1002/pc.27302.

[33] X. Zhu, W. Chen, L. Liu, K. Xu, G. Luo, and Z. Zhao, “Experimental investigation on high-velocity impact damage and compression after impact behavior of 2D and 3D textile composites,” *Compos Struct*, vol. 303, Jan. 2023, doi: 10.1016/j.compstruct.2022.116256.

[34] H. Kolsky, “An Investigation of the Mechanical Properties of Materials at very High Rates of Loading,” *Proceedings of the Physical Society. Section B*, vol. 62, no. 11, pp. 676–700, Nov. 1949, doi: 10.1088/0370-1301/62/11/302.

[35] B. Hopkinson, “X. A method of measuring the pressure produced in the detonation of high, explosives or by the impact of bullets,” *Philosophical Transactions of the Royal Society of London. Series A, Containing Papers of a Mathematical or Physical Character*, vol. 213, no. 497–508, pp. 437–456, Jan. 1914, doi: 10.1098/rsta.1914.0010.

[36] W. Chen and B. Song, *Split Hopkinson (Kolsky) Bar*. Boston, MA: Springer US, 2011. doi: 10.1007/978-1-4419-7982-7.

[37] T. Nicholas, "Tensile testing of materials at high rates of strain," *Exp Mech*, vol. 21, no. 5, pp. 177–185, May 1981, doi: 10.1007/BF02326644.

[38] W. E. Baker and C. H. Yew, "Strain-Rate Effects in the Propagation of Torsional Plastic Waves," *J Appl Mech*, vol. 33, no. 4, pp. 917–923, Dec. 1966, doi: 10.1115/1.3625202.

[39] B. Budiwantoro, M. A. Kariem, and B. Febrinawarta, "The Influence of Shear Angles on the Split Hopkinson Shear Bar Testing," *Int J Impact Eng*, vol. 149, Mar. 2021, doi: 10.1016/j.ijimpeng.2020.103787.

[40] Z. Zhao *et al.*, "Effects of loading rate and loading direction on the compressive failure behavior of a 2D triaxially braided composite," *Int J Impact Eng*, vol. 156, Oct. 2021, doi: 10.1016/j.ijimpeng.2021.103928.

[41] B. Sun, L. Yang, and B. Gu, "Strain rate effect on four-step three-dimensional braided composite compressive behavior," *AIAA Journal*, vol. 43, no. 5, pp. 994–999, 2005, doi: 10.2514/1.14560.

[42] B. Gu and F. K. Chang, "Energy absorption features of 3-D braided rectangular composite under different strain rates compressive loading," *Aerosp Sci Technol*, vol. 11, no. 7–8, pp. 535–545, Nov. 2007, doi: 10.1016/j.ast.2007.03.004.

[43] B. Sun and B. Gu, "High strain rate behavior of 4-step 3D braided composites under compressive failure," *J Mater Sci*, vol. 42, no. 7, pp. 2463–2470, Apr. 2007, doi: 10.1007/s10853-006-1295-x.

[44] B. Sun, N. Pan, and B. Gu, “Three-dimensional textile structural composites under high strain rate compression: Z-transform and discrete frequency-domain analysis,” *Philosophical Magazine*, vol. 87, no. 34, pp. 5461–5484, Dec. 2007, doi: 10.1080/14786430701675803.

[45] D. Sen Li, Z. X. Lu, and D. N. Fang, “Longitudinal compressive behavior and failure mechanism of three-dimensional five-directional carbon/phenolic braided composites at high strain rates,” *Materials Science and Engineering A*, vol. 526, no. 1–2, pp. 134–139, Nov. 2009, doi: 10.1016/j.msea.2009.07.009.

[46] D. Sen Li, Z. X. Lu, N. Jiang, and D. N. Fang, “High strain rate behavior and failure mechanism of three-dimensional five-directional carbon/phenolic braided composites under transverse compression,” *Compos B Eng*, vol. 42, no. 2, pp. 309–317, Mar. 2011, doi: 10.1016/j.compositesb.2010.11.011.

[47] D. Sen Li, Z. X. Lu, N. Jiang, and D. N. Fang, “Influence of braiding parameters on the dynamic compressive properties and failure mechanism of 3D braided composites,” *Mechanics of Advanced Materials and Structures*, vol. 21, no. 9, pp. 716–721, Oct. 2014, doi: 10.1080/15376494.2012.707300.

[48] Y. Zhang, B. Sun, and B. Gu, “Experimental characterization of transverse impact behaviors of four-step 3-D rectangular braided composites,” *J Compos Mater*, vol. 46, no. 24, pp. 3017–3029, Nov. 2012, doi: 10.1177/0021998311435531.

[49] Y. Zhang, P. Wang, and C. Guo, “Energy absorption behaviors of 3D braided composites under impact loadings with frequency domain analysis,” *Polym Compos*, vol. 37, no. 5, pp. 1620–1627, May 2016, doi: 10.1002/pc.23334.

[50] X. Gao, M. Zhang, A. Siddique, H. Yang, T. Liu, and M. Cao, "Damage evolution and failure mechanism of three-dimensional braided composite subjected to varied high strain-rate loadings," *Textile Research Journal*, Apr. 2022, doi: 10.1177/00405175221135877.

[51] Z. Zhao, L. Liu, W. Chen, and X. Huang, "Dynamic compressive behavior in different loading directions of 3D braided composites with different braiding angle," *Latin American Journal of Solids and Structures*, vol. 15, no. 9, Aug. 2018, doi: 10.1590/1679-78255111.

[52] H. Tan, X. Huang, L. Liu, Y. Guan, and W. Chen, "Dynamic compressive behavior of four-step three-dimensional braided composites along three directions," *Int J Impact Eng*, vol. 134, Dec. 2019, doi: 10.1016/j.ijimpeng.2019.103366.

[53] B. Shi, S. Liu, A. Siddique, Y. Du, B. Sun, and B. Gu, "Impact fracture behaviors of three-dimensional braided composite U-notch beam subjected to three-point bending," *International Journal of Damage Mechanics*, vol. 28, no. 3, pp. 404–426, Mar. 2019, doi: 10.1177/1056789518772619.

[54] Y. Li, B. Gu, B. Sun, and Z. Pan, "Punch shear performance and damage mechanisms of three-dimensional braided composite with different thicknesses," *Textile Research Journal*, vol. 89, no. 11, pp. 2126–2141, Jun. 2019, doi: 10.1177/0040517518786281.

[55] X. Gao, B. Sun, and B. Gu, "Damage mechanisms of 3-D rectangular braided composite under multiple impact compressions," *Aerosp Sci Technol*, vol. 82–83, pp. 46–60, Nov. 2018, doi: 10.1016/j.ast.2018.08.031.

[56] M. Hu, J. Zhang, B. Sun, and B. Gu, "Finite element modeling of multiple transverse impact damage behaviors of 3-D braided composite beams at microstructure level," *Int J Mech Sci*, vol. 148, pp. 730–744, Nov. 2018, doi: 10.1016/j.ijmecsci.2018.09.034.

[57] X. Gao, A. Siddique, B. Sun, and B. Gu, “Effect of braiding angle on dynamic mechanical properties of 3-D braided rectangular composites under multiple impact compressions,” *J Compos Mater*, vol. 53, no. 13, pp. 1827–1846, Jun. 2019, doi: 10.1177/0021998318812926.

[58] X. Gao, A. Siddique, B. Sun, and B. Gu, “Influence of Braiding Angle on Multiple Impact Damages of 3-D Braided Composite along Longitudinal Direction,” *Applied Composite Materials*, vol. 26, no. 4, pp. 1261–1280, Aug. 2019, doi: 10.1007/s10443-019-09779-1.

[59] H. Zhou, Z. Pan, R. K. Gideon, B. Gu, and B. Sun, “Experimental and numerical investigation of the transverse impact damage and deformation of 3-D circular braided composite tubes from meso-structure approach,” *Compos B Eng*, vol. 86, pp. 243–253, Feb. 2016, doi: 10.1016/j.compositesb.2015.10.019.

[60] H. Zhou, B. Sun, and B. Gu, “Responses of 3D four-directional and five-directional circular braided composite tubes under transverse impact,” *International Journal of Crashworthiness*, vol. 21, no. 4, pp. 353–366, Jul. 2016, doi: 10.1080/13588265.2016.1189161.

[61] H. Zhou, D. Hu, B. Gu, and B. Sun, “Transverse impact performance and finite element analysis of three dimensional braided composite tubes with different braiding layers,” *Compos Struct*, vol. 168, pp. 345–359, May 2017, doi: 10.1016/j.compstruct.2017.02.025.

[62] H. Zhou, C. Li, L. Zhang, B. Crawford, A. S. Milani, and F. K. Ko, “Micro-XCT analysis of damage mechanisms in 3D circular braided composite tubes under transverse impact,” *Compos Sci Technol*, vol. 155, pp. 91–99, Feb. 2018, doi: 10.1016/j.compscitech.2017.11.025.

[63] X. Wu, Q. Zhang, W. Zhang, B. Gu, and B. Sun, “Axial compressive deformation and damage of four-step 3-D circular braided composite tubes under various strain rates,” *Journal of the Textile Institute*, vol. 107, no. 12, pp. 1584–1600, Dec. 2016, doi: 10.1080/00405000.2015.1130298.

[64] T. Liu, X. Wu, B. Sun, W. Fan, W. Han, and H. Yi, “Investigations of defect effect on dynamic compressive failure of 3D circular braided composite tubes with numerical simulation method,” *Thin-Walled Structures*, vol. 160, Mar. 2021, doi: 10.1016/j.tws.2020.107381.

[65] H. Zhou, D. Hu, W. Zhang, B. Gu, and B. Sun, “The transverse impact responses of 3-D braided composite I-beam,” *Compos Part A Appl Sci Manuf*, vol. 94, pp. 158–169, Mar. 2017, doi: 10.1016/j.compositesa.2016.11.033.

[66] J. Chen, Z. Yu, and H. Jin, “Nondestructive testing and evaluation techniques of defects in fiber-reinforced polymer composites: A review,” *Frontiers in Materials*, vol. 9. Frontiers Media S.A., Oct. 24, 2022. doi: 10.3389/fmats.2022.986645.

[67] X.-Y. Zhou, S.-Y. Qian, N.-W. Wang, W. Xiong, and W.-Q. Wu, “A review on stochastic multiscale analysis for FRP composite structures,” *Compos Struct*, vol. 284, p. 115132, Mar. 2022, doi: 10.1016/j.compstruct.2021.115132.

[68] C. Barile, C. Casavola, G. Pappalettera, and V. P. Kannan, “Application of different acoustic emission descriptors in damage assessment of fiber reinforced plastics: A comprehensive review,” *Engineering Fracture Mechanics*, vol. 235. Elsevier Ltd, Aug. 01, 2020. doi: 10.1016/j.engfracmech.2020.107083.

[69] J. Jodhani, A. Handa, A. Gautam, Ashwni, and R. Rana, “Ultrasonic non-destructive evaluation of composites: A review,” *Mater Today Proc*, Jan. 2022, doi: 10.1016/j.matpr.2022.12.055.

[70] Y. Li, W. Zhang, Z. W. Yang, J. Y. Zhang, and S. J. Tao, “Low-velocity impact damage characterization of carbon fiber reinforced polymer (CFRP) using infrared thermography,” *Infrared Phys Technol*, vol. 76, pp. 91–102, May 2016, doi: 10.1016/j.infrared.2016.01.019.

[71] C. Timpano, H. Abdoli, S. N. Leung, and G. W. Melenka, “Characterization of open-cellular polymeric foams using micro-computed tomography,” *Polymer (Guildf)*, vol. 202, Aug. 2020, doi: 10.1016/j.polymer.2020.122628.

[72] J. Hsieh, “Introduction,” in *Computed Tomography: Principles, Design, Artifacts, and Recent Advances, Fourth Edition*, SPIE, 2022. doi: 10.1117/3.2605933.ch1.

[73] J. Hsieh, “Preliminaries,” in *Computed Tomography: Principles, Design, Artifacts, and Recent Advances, Fourth Edition*, SPIE, 2022. doi: 10.1117/3.2605933.ch2.

[74] E. N. Landis and D. T. Keane, “X-ray microtomography,” *Materials Characterization*, vol. 61, no. 12. Elsevier Inc., pp. 1305–1316, 2010. doi: 10.1016/j.matchar.2010.09.012.

[75] G. Requena, G. Fiedler, B. Seiser, P. Degischer, M. Di Michiel, and T. Buslaps, “3D-Quantification of the distribution of continuous fibres in unidirectionally reinforced composites,” *Compos Part A Appl Sci Manuf*, vol. 40, no. 2, pp. 152–163, Feb. 2009, doi: 10.1016/j.compositesa.2008.10.014.

[76] S.-B. Lee, S. R. Stock, M. D. Butts, T. L. Starr, T. M. Breunig, and J. H. Kinney, “Pore geometry in woven fiber structures: 0 ± 90 ± plain-weave cloth layup preform,” 1998.

[77] P. J. Schilling, B. P. R. Karedla, A. K. Tatiparthi, M. A. Verges, and P. D. Herrington, "X-ray computed microtomography of internal damage in fiber reinforced polymer matrix composites," *Compos Sci Technol*, vol. 65, no. 14, pp. 2071–2078, Nov. 2005, doi: 10.1016/j.compscitech.2005.05.014.

[78] C. Düreth *et al.*, "Determining the damage and failure behaviour of textile reinforced composites under combined in-plane and out-of-plane loading," *Materials*, vol. 13, no. 21, pp. 1–45, Nov. 2020, doi: 10.3390/ma13214772.

[79] B. Ao, J. Wu, G. Wu, and W. Wu, "Application of region of interest CT in analysis of CMC plate-like component," in *Second Symposium on Novel Technology of X-Ray Imaging*, P. Liu, Y. Tian, and T. Xiao, Eds., SPIE, May 2019, p. 117. doi: 10.1117/12.2524755.

[80] A. Ayadi, M. Deléglise-Lagardère, C. H. Park, and P. Krawczak, "Analysis of Impregnation Mechanism of Weft-Knitted Commingled Yarn Composites by Staged Consolidation and Laboratory X-Ray Computed Tomography," *Front Mater*, vol. 6, Oct. 2019, doi: 10.3389/fmats.2019.00255.

[81] L. Schöttl, P. Kolb, W. V. Liebig, K. A. Weidenmann, K. Inal, and P. Elsner, "Crack characterization of discontinuous fiber-reinforced composites by using micro-computed tomography: Cyclic in-situ testing, crack segmentation and crack volume fraction," *Composites Communications*, vol. 21, Oct. 2020, doi: 10.1016/j.coco.2020.100384.

[82] R. Adams and L. Bischof, "Seeded region growing," *IEEE Trans Pattern Anal Mach Intell*, vol. 16, no. 6, pp. 641–647, Jun. 1994, doi: 10.1109/34.295913.

[83] L. Schöttl, W. V. Liebig, K. A. Weidenmann, K. Inal, and P. Elsner, "The use of the empirical crack orientation tensor to characterize the damage anisotropy," *Composites Communications*, vol. 25, Jun. 2021, doi: 10.1016/j.coco.2020.100613.

[84] G. Ziółkowski, J. Pach, D. Pyka, T. Kurzynowski, and K. Jamroziak, "X-ray computed tomography for the development of ballistic composite," *Materials*, vol. 13, no. 23, pp. 1–19, Dec. 2020, doi: 10.3390/ma13235566.

[85] L. Guo, J. Huang, L. Zhang, and X. Sun, "Damage evolution of 3D woven carbon/epoxy composites under tension-tension fatigue loading based on synchrotron radiation computed tomography (SRCT)," *Int J Fatigue*, vol. 142, p. 105913, Jan. 2021, doi: 10.1016/j.ijfatigue.2020.105913.

[86] R. Böhm *et al.*, "A quantitative comparison of the capabilities of in situ computed tomography and conventional computed tomography for damage analysis of composites," *Compos Sci Technol*, vol. 110, pp. 62–68, Apr. 2015, doi: 10.1016/j.compscitech.2015.01.020.

[87] R. Protz, I. Koch, and M. Gude, "In-situ computer tomography for analyzing the effect of voids on the damage behavior of composite materials," in *IOP Conference Series: Materials Science and Engineering*, Institute of Physics Publishing, Sep. 2018. doi: 10.1088/1757-899X/406/1/012013.

[88] D. Hülsbusch, R. Helwing, S. Mrzljak, and F. Walther, "Comparison of the damage evolution in glass fiber-reinforced polyurethane and epoxy in the HCF and VHCF regimes investigated by intermittent in situ X-ray computed tomography," in *IOP Conference*

Series: Materials Science and Engineering, IOP Publishing Ltd, Oct. 2020. doi: 10.1088/1757-899X/942/1/012036.

[89] Q. Zeng, L. Sun, J. Ge, W. Wu, J. Liang, and D. Fang, "Damage characterization and numerical simulation of shear experiment of plain woven glass-fiber reinforced composites based on 3D geometric reconstruction," *Compos Struct*, vol. 233, Feb. 2020, doi: 10.1016/j.compstruct.2019.111746.

[90] J. Holmes, S. Sommacal, R. Das, Z. Stachurski, and P. Compston, "Characterisation of off-axis tensile behaviour and mesoscale deformation of woven carbon-fibre/PEEK using digital image correlation and X-ray computed tomography," *Compos B Eng*, vol. 229, Jan. 2022, doi: 10.1016/j.compositesb.2021.109448.

[91] H. Schreier, J.-J. Orteu, and M. A. Sutton, *Image Correlation for Shape, Motion and Deformation Measurements*. Boston, MA: Springer US, 2009. doi: 10.1007/978-0-387-78747-3.

[92] F. Xu, "Quantitative characterization of deformation and damage process by digital volume correlation: A review," *Theoretical and Applied Mechanics Letters*, vol. 8, no. 2, pp. 83–96, Mar. 2018, doi: 10.1016/j.taml.2018.02.004.

[93] A. Buljac *et al.*, "Digital Volume Correlation: Review of Progress and Challenges," *Exp Mech*, vol. 58, no. 5, pp. 661–708, Jun. 2018, doi: 10.1007/s11340-018-0390-7.

[94] C. S. Timpano and G. W. Melenka, "Artificial seeding for micro-computed tomography image contrast enhancement for digital volume correlation," *Compos B Eng*, vol. 215, Jun. 2021, doi: 10.1016/j.compositesb.2021.108809.

[95] B. K. Bay, T. S. Smith, D. P. Fyhrie, and M. Saad, "Digital volume correlation: Three-dimensional strain mapping using X-ray tomography," *Exp Mech*, vol. 39, no. 3, pp. 217–226, Sep. 1999, doi: 10.1007/BF02323555.

[96] T. Wang, Z. Jiang, Q. Kemao, F. Lin, and S. H. Soon, "GPU Accelerated Digital Volume Correlation," *Exp Mech*, vol. 56, no. 2, pp. 297–309, Feb. 2016, doi: 10.1007/s11340-015-0091-4.

[97] J. P. Lewis, "Fast Normalized Cross-Correlation," *Ind. Light Magic*, vol. 10, Oct. 2001.

[98] E. Tudisco, E. Andò, R. Cailletaud, and S. A. Hall, "TomoWarp2: A local digital volume correlation code," *SoftwareX*, vol. 6, pp. 267–270, Jan. 2017, doi: 10.1016/J.SOFTX.2017.10.002.

[99] V. Mazars *et al.*, "Damage investigation and modeling of 3D woven ceramic matrix composites from X-ray tomography in-situ tensile tests," *Acta Mater*, vol. 140, pp. 130–139, Nov. 2017, doi: 10.1016/j.actamat.2017.08.034.

[100] R. Lorenzoni *et al.*, "Combined mechanical and 3D-microstructural analysis of strain-hardening cement-based composites (SHCC) by in-situ X-ray microtomography," *Cem Concr Res*, vol. 136, Oct. 2020, doi: 10.1016/j.cemconres.2020.106139.

[101] C. Liu, Y. Chen, D. Shi, J. Marrow, X. Jing, and X. Yang, "In situ investigation of failure in 3D braided SiCf/SiC composites under flexural loading," *Compos Struct*, vol. 270, Aug. 2021, doi: 10.1016/j.compstruct.2021.114067.

[102] J. Holmes, S. Sommacal, Z. Stachurski, R. Das, and P. Compston, "Digital image and volume correlation with X-ray micro-computed tomography for deformation and damage

characterisation of woven fibre-reinforced composites," *Compos Struct*, vol. 279, Jan. 2022, doi: 10.1016/j.compstruct.2021.114775.

[103] A. Goyal and G. W. Melenka, "Investigation of carbon-aramid hybrid braided composites using digital volume correlation," *Compos Struct*, vol. 321, Oct. 2023, doi: 10.1016/j.compstruct.2023.117207.

Chapter 3 Assessment of Low-Velocity Impact Response of a Hybrid Carbon-Aramid Braided Composite by Algorithmic Quantification of Volumetric Structures

3.1 Introduction

Two-dimensional (2D) tubular braided composites are cost-effective and often used in axisymmetric parts for stiffness-critical applications [1], [2], and more complex structural applications using joints [3]. These materials consist of a woven architecture of fibre tows, which has favourable impact performance when compared to their unidirectional counterparts, particularly in residual compressive and shear strengths [4]. As such, characterizing the impact properties of braided composites in a variety of forms has become a valuable endeavour in recent years [5]–[8]. The braiding process forms fibres into a 2D or 3D textile architecture [9], [10], where matrix impregnation is then done using a variety of techniques, including manual lay-up, and automated resin transfer molding (RTM) [11], [12]. Braiding as an automated means of fabricating high-performance composite parts provides benefits in reducing manufacturing times and costs [13], [14], but also provides a challenge in quality control based on the selection of manufacturing processes [15].

Impact damage of braided composites has been characterized using various methods, such as finite element analysis (FEA) [16], [17], microscopic analysis [18], [19], and micro-computed tomography (μCT). μCT is a non-destructive method of sample imaging, where X-ray images are reconstructed into volumetric representations of a sample to examine its internal structure [20], and has been applied to polymer matrix composites to assess manufacturing quality, porosity, fibre architecture, and damage modes from quasi-static, fatigue, and impact tests [21]. Several general findings were made from μCT in damage assessment of materials. For instance, voids support the propagation of damage cracks and affect material performance based on a complex relationship between void size and criticality of location [22], individual fibres under compressive loading can fail based on a phenomenon known as micro-buckling [23], tensile failure of axial fibres can initiate from matrix failure within layers of transverse backing fibres [24], damage in a flat laminate can be characterized on a ply-by-ply basis using a distance transform technique [25], and nano-computed tomography can supplement μCT to investigate the microstructure of a crack initiation site [26].

Studies have used μCT to investigate a variety of braided composites, including 2D tubular braided composites made from carbon/epoxy [27]–[29], aramid/epoxy [30], and bio-based materials such as cellulose fibres [31]–[33], and 3D braided composites made from carbon/epoxy [34]–[37] and glass/epoxy [38]. Some hybrid composites have also been assessed, such as 2D braided carbon-glass-aramid [39] and glass-carbon [40], 2D woven carbon-glass-basalt [41] and carbon-aramid [42], [43], and 3D woven glass-carbon [44]. Literature on the assessment of impact response of braided composites by μCT is limited, with a work by Zhou et al. [34] investigating 3D circular braided composites by qualitative analysis of internal structures after impact. The study found that at a braid angle of 45°, tow splitting was found to be the primary damage mechanism and material cracking propagated radially, while at lower braid angles, fibre fracture became the dominant damage mechanism and material cracking propagated along the length of the material.

Furthermore, volumes acquired by μCT can be further assessed by measuring 3D volumetric deformations and strains using digital volume correlation (DVC). This technique was mainly employed with in-situ μCT to ensure sample alignment [45]–[48]. Goyal and Melenka [48] used in-situ μCT for tensile testing of 2D braided hybrid carbon-aramid composite flat samples. The effects of particle seeding on strain measurements were examined by testing samples with and without high-contrast copper particles. The study found that the addition of particles improved strain measurements by creating distinct subset profiles throughout the volume. Ex-situ μCT was used with DVC by Holmes et al. [49], where ceramic matrix composites were studied by tensile load relaxation testing. The study found that under warp loading, strain concentrations formed in the material along an edge of the sample, while under weft loading, the material experienced significant out-of-plane strain due to the ductility of the matrix material. Based on the available literature, there remains a significant gap in DVC measurement of ex-situ μCT scanned samples, which is highly applicable to impact testing where large-scale equipment is typically used.

Impact damage that is not easily detectable by external inspection is referred to as barely visible impact damage (BVID), which is found to have significant influence on the structural performance of composite parts [50]. For braided composites, studies on BVID are largely based on numerical modelling. Blinzler and Binienda [51] developed a macromechanical analytical model for BVID by three-point bending of triaxially braided carbon/epoxy composites that used a tie-break method to model delamination. Comparison of the model with a baseline simulation and experimental results showed that deflections were underestimated by the baseline and overestimated by the tie-break method. Wang et al. [52] performed a numerical study on BVID by impact attenuation testing of braided composite shin guards. The model was validated with experiments and demonstrated its potential of expediting performance assessment of braided composite parts as it accounted for braid angles. A significant gap remains in the experimental assessment of internal structures subjected to BVID.

This study investigated the impact performance of 2D tubular braided hybrid carbon-aramid composites. A multi-layered inter-ply symmetrical configuration of biaxial braided carbon and aramid fibres was manufactured, and impact testing was performed using a split Hopkinson pressure bar (SHPB) system to induce BVID. The sample was imaged before and after impact testing using ex-situ μCT and the datasets were aligned using image registration. Quantitative analysis was performed on the individual voids and the damage cracks using an algorithm developed herein. Finally, a DVC study was performed to measure 3D strains within representative volumes of interest and associate the results with findings from the crack detection algorithm.

3.2 Methods

3.2.1 Sample Preparation

The hybrid braided tubular sample, as shown in Figure 3-1, was manufactured using a hand lay-up technique. As illustrated in Figure 3-1(a), the material consisted of an inter-ply hybrid of carbon and aramid fibres. Figure 3-1(b) illustrates the laminate configuration as braided plies of aramid over carbon over aramid in a $[\pm 40°]_3$ configuration. The manufactured sample is shown in Figure 3-1(c). A combination of 2” braided carbon fibre biaxial sleeves and 2” braided aramid fibre biaxial sleeves (#2609 and #2611, Fibre Glast Developments Corp., Brookville, OH) was used as the fibre materials. A laminating epoxy resin and cure (2000 epoxy resin with 2060 hardener, Fibre Glast Developments Corp., Brookville, OH) was used as the matrix material. Lay-up was performed on a 38.1 mm (1.5”) diameter mandrel, forming a tube of length 304.8 mm (12”). The sample was cut to size using an abrasive saw. As shown in Figure 3-1(d), the braid angle, θ, was measured from images of the braid pattern, acquired by a high-resolution camera (Ace acA2440-35um, Basler AG, Ahrensburg, Germany). Based on physical measurements, the sample had an inner diameter of 38.1 mm (1.50”), an outer diameter of 41.0 mm (1.61”), and a height of 53.1 mm (2.09”).

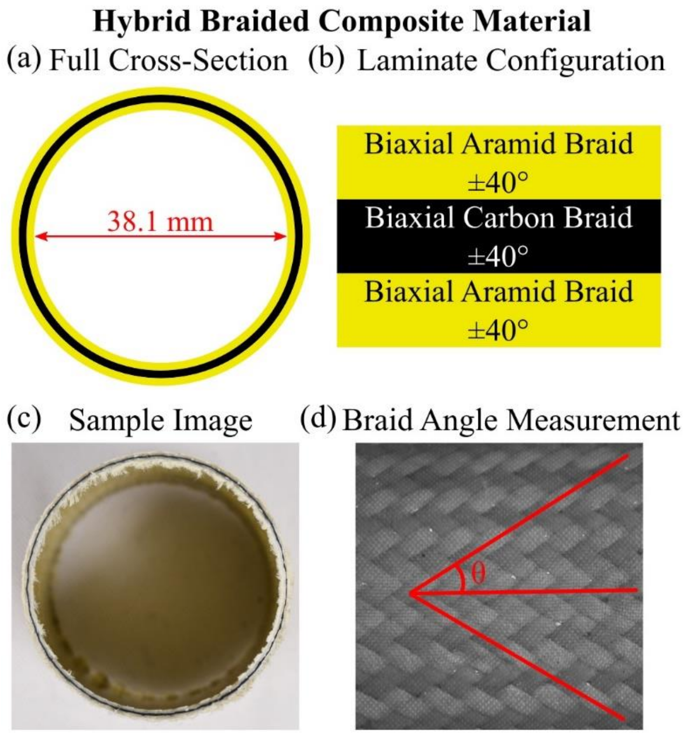

Figure 3-1: Hybrid braided composite lay-up: (a) schematic of full tubular cross-section; (b) ply-by-ply material properties; (c) image of sample in cross-sectional view; (d) image of sample in transverse view for braid angle measurement.

3.2.2 Impact Testing

The sample was subjected to transverse impact testing using a split Hopkinson pressure bar (SHPB) testing apparatus [53]. A custom fixture was designed to clamp the sample in place, leaving a free length of 38.1 mm (1.5”). A round tip with a 20 mm diameter was attached to the incident bar, serving as the point of contact with the sample. The striker bar was accelerated by a gas pressure of 690 kPa (100 psi). As a result, based on the mass of the striker and the measured impact velocity, the impact energy applied to the sample was measured to be 8.76 J, which induced BVID in the material that was then analyzed volumetrically.

3.2.3 Volumetric Scanning

The sample was subjected to pre-impact and post-impact volumetric X-ray scanning by micro-computed tomography (μCT) using a high-resolution 3D X-ray microscope (SkyScan 1272, Bruker Corporation, Billerica, MA, USA). The scan settings for the braided composite sample are listed in Table 3-1. These settings were chosen to provide optimal image contrast of the hybrid braided composite sample for further image processing and analysis. The settings resulted in a field of view of 43.6 mm × 43.6 mm × 13.3 mm allowing for the entire sample diameter to be imaged.

Table 3-1: Micro-computed tomography scan settings for tubular braided composite sample.

Source Voltage	50 kV
Source Current	153 μA
Filter	Aluminum 0.25 mm
Camera Binning	2 × 2
Horizontal Offset Positions	2
Image Pixel Size	9.3 μm
Frame Averaging	2
Rotation Step	0.4°
Reconstructed Volume Resolution	4688 px × 4688 px × 1433 px
Reconstructed Volume Size	43.6 mm × 43.6 mm × 13.3 mm

The transverse projections of the sample acquired by μCT scans were then reconstructed using proprietary CT data reconstruction software (NRecon, Bruker Corporation, Billerica, MA, USA). The result is a set of image slices representing cross-sections of the sample, as shown in Figure 3-2. The undamaged sample, as shown in Figure 3-2(a), contained small holes throughout the circumference which were classified as voids, and a larger hole which was classified as an imperfection or defect caused by the manufacturing process. The damaged sample, as shown in Figure 3-2(b), contained a similar configuration of holes as well as thin features at the impact site which were classified as impact damage by cracking.

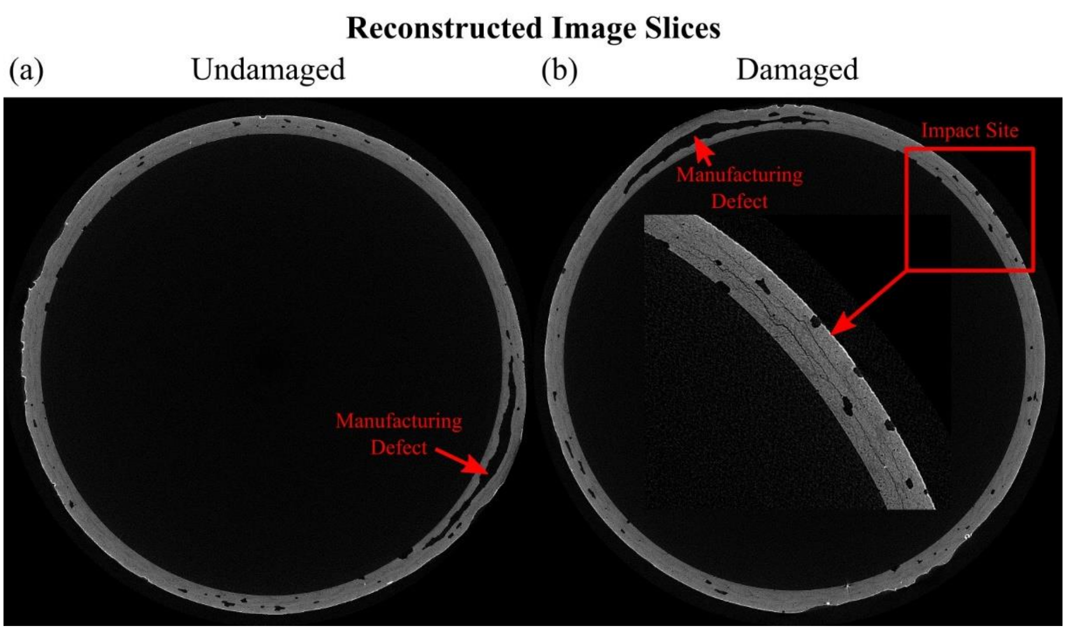

Figure 3-2: Representative cross-sectional images of the hybrid braided composite sample (a) before impact damage; (b) after impact damage. A defect caused by the hand lay-up process is found in both the undamaged and damaged samples. Sample damage manifested as thin internal cracks and was localized to the impact site.

3.2.4 Image Processing

3.2.4.1 Volume Registration

Alignment of datasets is critical for accurate determination of localized changes before and after impact damage. The datasets were registered using the 3D inspection software (DataViewer, Bruker Corporation, Billerica, MA, USA), using the undamaged sample data as the reference and the damaged sample data as the target. As shown in Figure 3-3, the 3D registration process used a sum of square difference as a similarity metric, then applied rigid transformations in the form of Cartesian x/y/z translations and Euler angles following the z-x-z convention. After the datasets were cropped to 4608 px × 4644 px × 921 px, preserving the matching regions, the resultant dimensions and coordinate system for the registered volumes are shown in Figure 3-4.

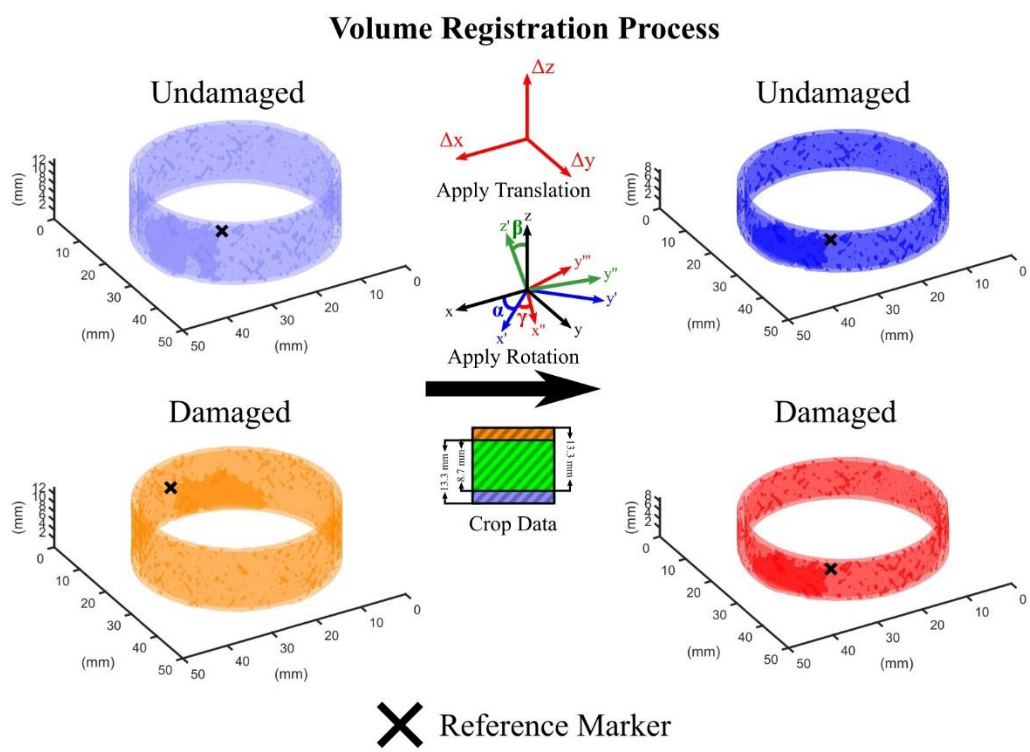

Figure 3-3: Process for registering volumetric datasets from μCT. The damaged dataset is rotated, then vertically translated to align with the matching portion of the undamaged sample.

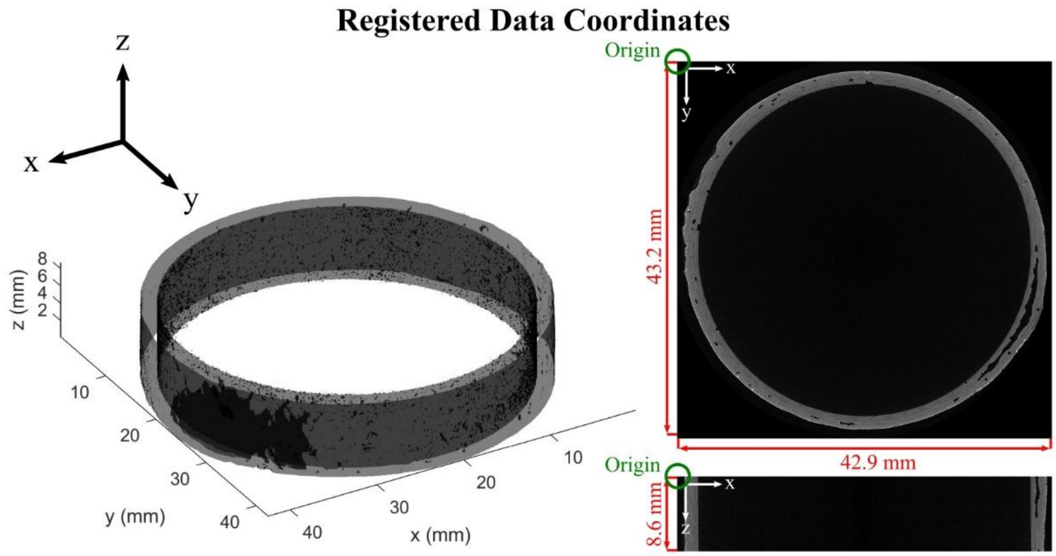

Figure 3-4: Dimensions and coordinate system of registered datasets. The origin of the coordinate system is shown in green in the x-y and x-z views.

3.2.4.2 Geometry Analysis

Geometric properties of the tubular sample were assessed using a series of image processing techniques using MATLAB and the Image Processing Toolbox. To expedite image processing and analysis of object properties, the datasets were downsampled by a factor of 4 on each axis to volumes of 1161 px × 1152 px × 231 px. In the decimated datasets, a 3D median filter with a window size of 3 pixels was applied to provide clarity between the sample material and voids. Next, the image slices were binarized using a threshold found by an automated search using histograms of light intensity values as shown in Figure 3-5(b), separating the sample material from its surroundings and voids as shown in Figure 3-5(c). A solid outer region was then created by filling the holes in the binarized image using the ‘imfill’ function as shown in Figure 3-5(d). The hollow inner region was then extracted by subtracting the binarized image from the filled outer region using a Boolean operation as shown in Figure 3-5(e), then isolating the largest object using the ‘bwareafilt’ function as shown in Figure 3-5(f). Object properties for the inner and outer regions such as area and eccentricity were extracted using the ‘regionprops’ function. Cross-sectional areas A_c were evaluated based on pixel counts and the diameters D of the inner and outer regions were evaluated at each image slice using Equation 1. Eccentricities e were evaluated from an ellipse with semi-major and semi-minor axis lengths a and b respectively, using Equation 2.

$$D = \sqrt{\frac{4A_c}{\pi}} \tag{1}$$

$$e = \sqrt{1 - \frac{b^2}{a^2}} \tag{2}$$

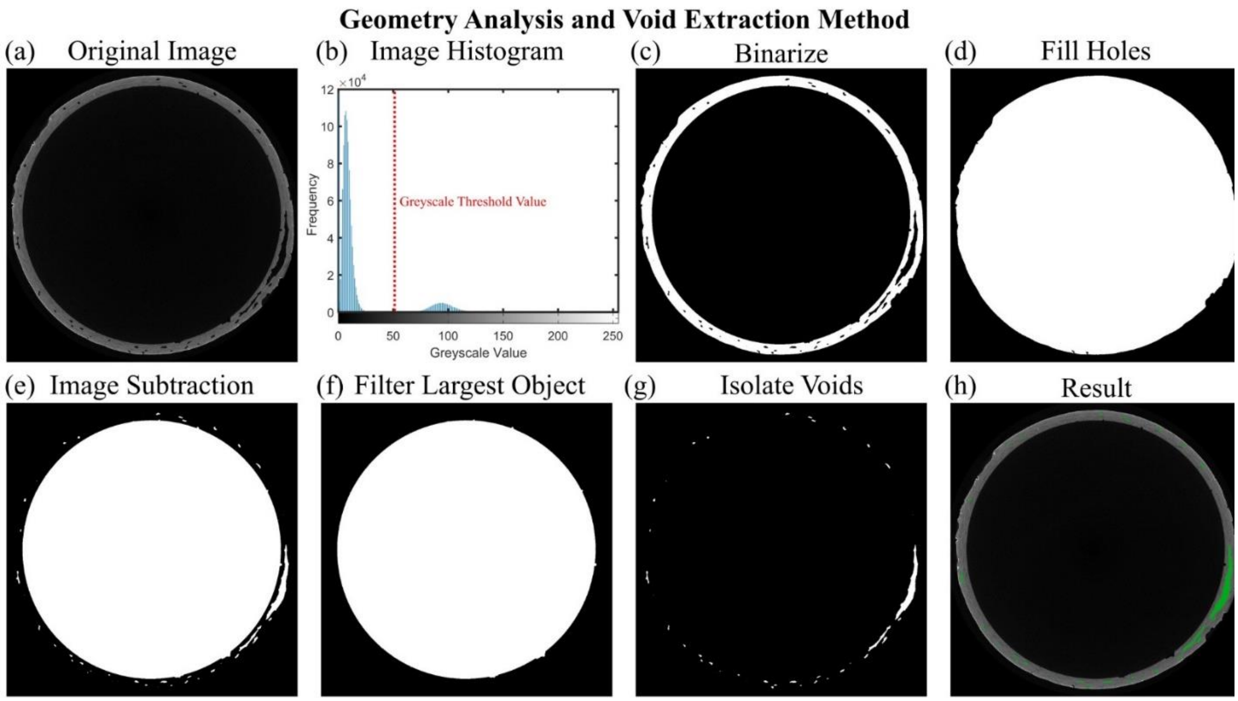

Figure 3-5: Process for sample geometry analysis and void extraction: (a) original resized image; (b) image histogram with threshold value chosen using peak greyscale values; (c) image filtered and binarized; (d) flood-fill operation applied, creating the outer region; (e) binarized image subtracted from outer region; (f) subtracted image filtered for the largest object, creating the inner region; (g) inner region removed from subtracted image to isolate voids; (h) resultant void objects overlayed in green over the original image.

3.2.4.3 Void Extraction

The voids in the sample were extracted by removing the inner region in Figure 3-5(f) from the subtracted image in Figure 3-5(e), as shown in Figure 3-5(g). The result, as shown in Figure 3-5(h), illustrates the identified voids in the context of the raw image slice.

The volume of voids V_v and volume of the composite material V_c were used to calculate the void volume fraction v_v of the undamaged and damaged samples using Equation 3.

$$v_v = \frac{V_v}{V_c + V_v} \times 100\% \tag{3}$$

Properties for each void such as centroid, volume, and surface area were acquired using the 'regionprops3' function. The position of each void was expressed as the distance of its centroid from the centroid of the sample interior region at its height. The sphericity ψ of each void was evaluated from volume V and surface area A_s using Equation 4. Next, a void registration process was developed as shown in Figure 3-6, where each void in the undamaged sample was matched to a suitable void in the damaged sample based on proximity and volume similarity, allowing for the analysis of volume change in each void due to impact damage. Statistical analysis in the form of a t-test was performed to determine if the applied impact damage caused an enlargement of voids.

$$\psi = \frac{\pi^{\frac{1}{3}}(6V)^{\frac{2}{3}}}{A_s} \tag{4}$$

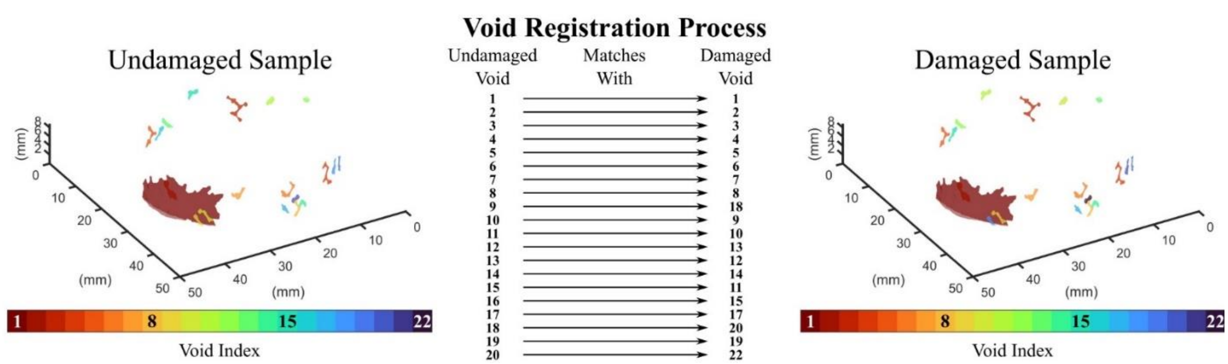

Figure 3-6: Process for registering individual voids. Voids are sorted by size and indices are assigned. Undamaged voids are matched to corresponding damaged void based on size and location similarities.

3.2.4.4 Crack Detection

A crack detection process was developed for the damaged sample in MATLAB as shown in Figure 3-7. Here, the dataset of the damaged volume was downsampled by a factor of 2 on each axis to a volume of 2322 px × 2304 px × 461 px. The higher-resolution volume was necessary to sufficiently resolve the thin features, whereas larger features such as voids were nevertheless sufficiently resolved after heavier downsampling. As shown in Figure 3-7(b), images were binarized using higher threshold values than those identified by the void extraction algorithm to mitigate blurring and separate the cracks from void perimeters. Voids were removed from the binarized images as shown in Figure 3-7(d) using a mask created by median filtering as shown in Figure 3-7(c). Next, image objects were filtered by eccentricity using the 'bwpropfilt' function as shown in Figure 3-7(e), such that only thin features with very high eccentricity were retained. The 'regionprops3' function was then used to identify and remove small 3D objects from the volume as shown in Figure 3-7(f). Next, objects were grouped into clusters by a mask to remove objects distant from the impact region and identify the crack network. As shown in Figure 3-7(g), the mask was created by applying a morphological dilation with a disk-shaped structural element with an initial size of 41 pixels. The crack was then isolated using a Boolean operation with the largest mask region as shown in Figure 3-7(h). The arc length of the crack at each image slice was then measured using a second-degree polynomial curve fit. Next, using the measurements shown in Figure 3-7(i), a refinement process was developed to eliminate outlier measurements and ensure the output of an appropriate crack profile. For each identified outlier, the masking process was retried by modifying the structural element size. The final crack network is shown in the context of raw image slices in Figure 3-7(j-l).

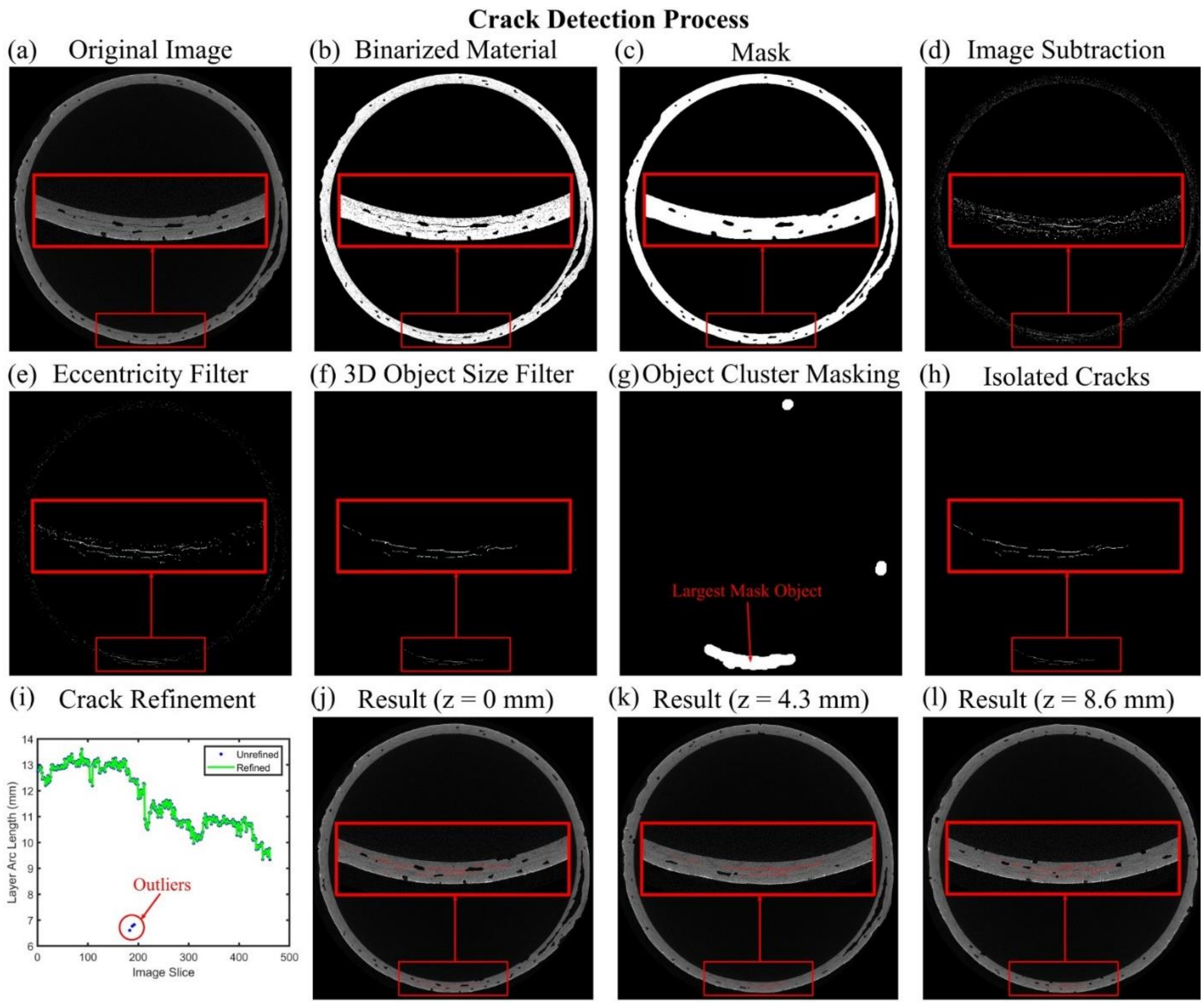

Figure 3-7: Process for impact crack detection: (a) raw resized image; (b) binarized image; (c) mask created by median filtering; (d) binarized image subtracted from mask; (e) image filtered for objects with thin features representing a crack profile; (f) image with small objects removed; (g) mask created by image dilation to identify the largest cohesive region; (h) image features extracted within the largest dilation mask object, representing the final isolated crack; (i) layer arc length versus image slice, used to refine the dilation masking process to eliminate outliers; (j) crack overlayed in red over the original image at z = 0 mm; (k) at z = 4.3 mm; (l) at z = 8.6 mm.

3.2.5 Digital Volume Correlation

Since two µCT image datasets were obtained before and after deformation, DVC was performed using a commercial image analysis software package (Avizo 2021.2, Thermo Fisher Scientific, Waltham, MA, USA) and the DVC Local Approach module to measure the resulting strain. As shown in Figure 3-8(a), the undamaged and damaged datasets were cropped to two 13.0 mm × 2.2 mm × 8.6 mm regions of interest, where deformations and strains were measured at the impacted side and its opposite side. As illustrated in Figure 3-8(b), the DVC process performed the measurements locally in cubic subsets, with a size of 138 µm as determined by a sensitivity study.

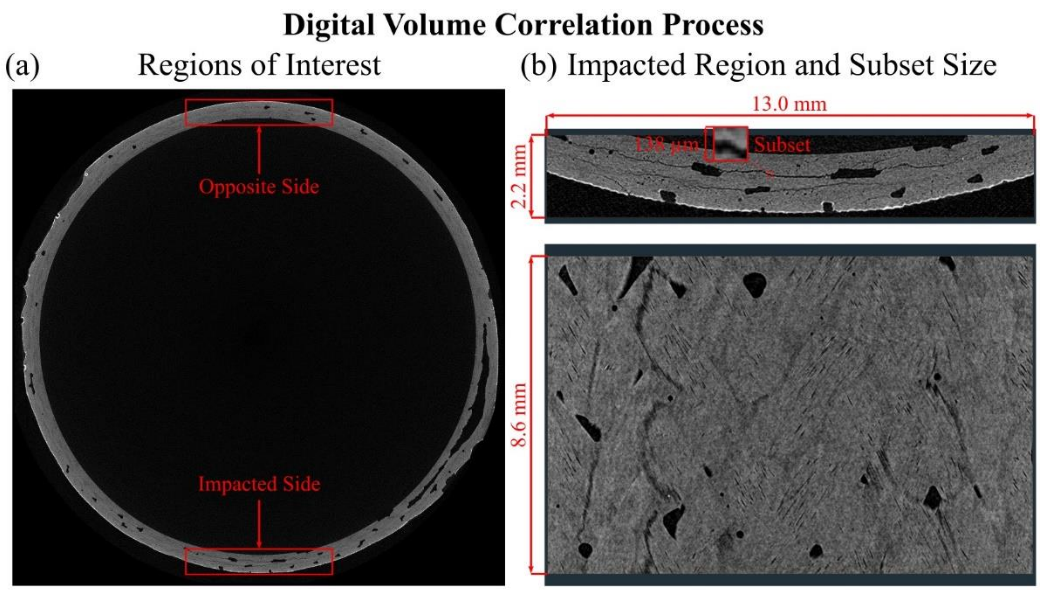

Figure 3-8: Digital volume correlation process: (a) the selected regions at the impacted side and opposite side are of equal volume; (b) dimensions of the region of interest at the impacted side with a subset enlarged for illustration.

3.2.5.1 Sensitivity Study

Results from the DVC sensitivity study are shown for the central x-y image slice in Figure 3-9. The selected region for this analysis is represented by the image slice shown in Figure 3-9(a), where delamination cracking occurred in both the inner and outer ply interfaces. At larger subsets shown in Figure 3-9(b-c), the expected strain profiles were present, but not with sufficient spatial resolution. At a subset size of 138 µm, as shown in Figure 3-9(d), local tensile strains from cracking and compressive strains from void deformation were appropriately resolved. Consequently, this subset size was chosen for further DVC processing of the sample volumes. At smaller subsets, noise artifacts became prominent around the edges of the material as shown in Figure 3-9(e), or throughout the material as shown in Figure 3-9(f).

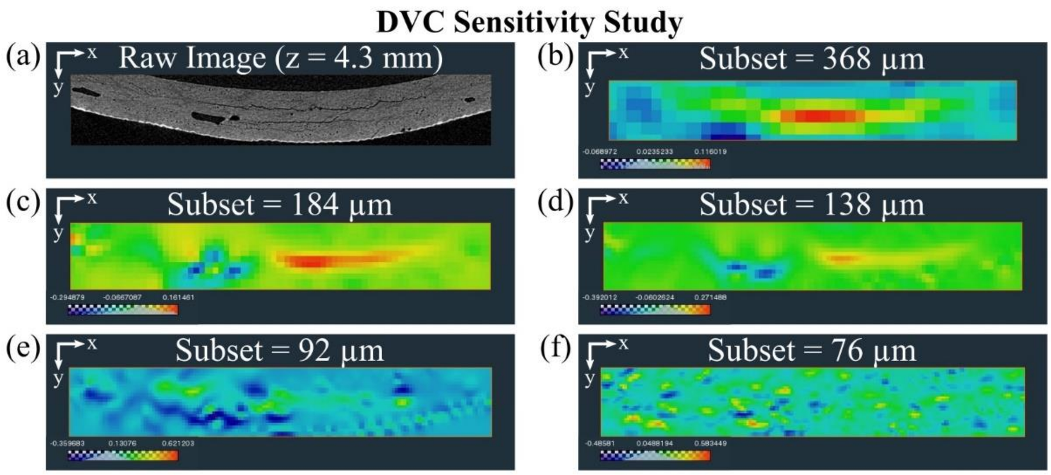

Figure 3-9: Results from DVC sensitivity study: (a) original image slice of the impacted side of the damaged sample at z = 4.3 mm; (b) normal y-strain map for a subset size of 368 µm; (c) 184 µm; (d) 138 µm; (e) 92 µm; (f) 76 µm.

3.3 Results & Discussion

3.3.1 Volume Registration

Transformations applied to the damaged sample data for volume registration are listed in Table 3-2. Results from the volume registration process are visualized in Figure 3-10. Figure 3-10(a) demonstrates the overlap between the undamaged and damaged volumes before registration, as shown in Figure 3-10(i), and after registration, as shown in Figure 3-10(ii). Figure 3-10(b) shows these results in terms of the voids alone, providing a different perspective where the voids are largely mismatched before registration, as shown in Figure 3-10(iii), but largely matched after registration, as shown in Figure 3-10(iv).

Table 3-2: Volume registration results - applied transformations to the damaged sample.

Translation $[x, y, z]$ (px)	[80, -44, 488]
Rotation $[\alpha, \beta, \gamma]$ (°)	[-162.6, -0.7, -29.8]

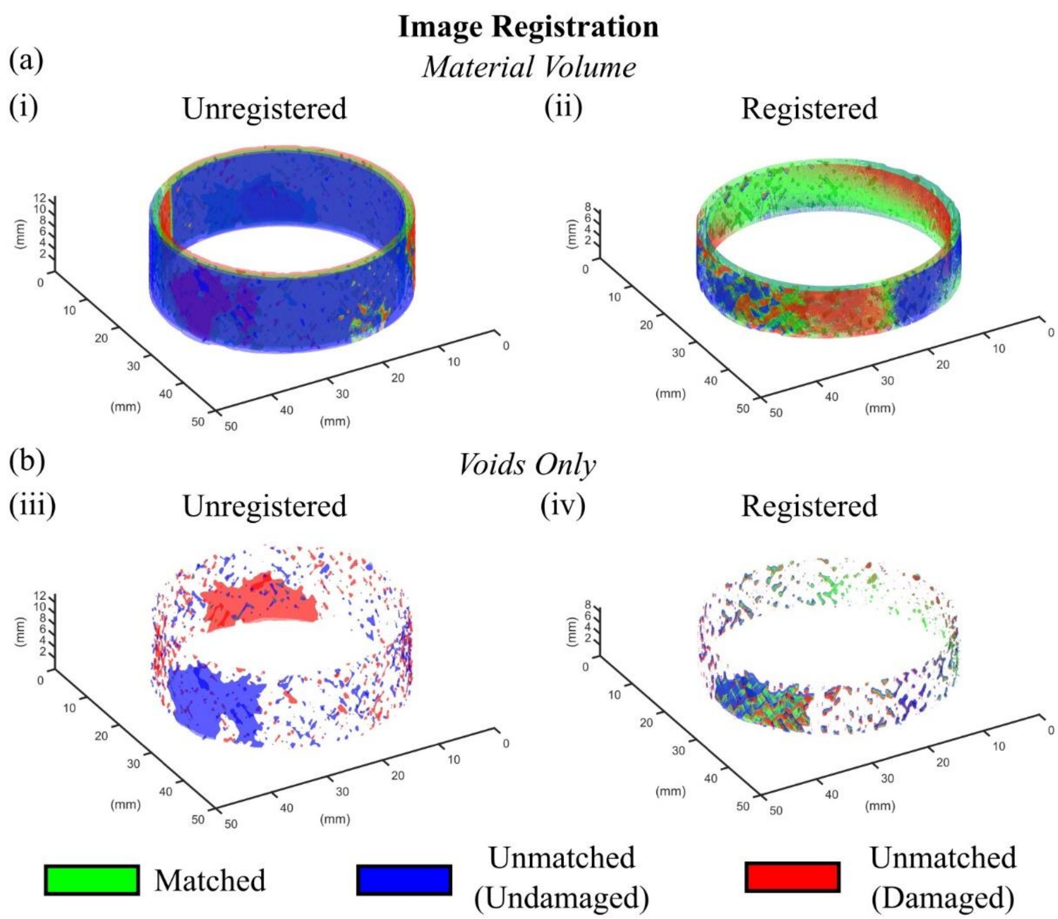

Figure 3-10: Visualized image registration results: (a) material volumes: (i) before; (ii) after registration; (b) isolated voids: (iii) before; (iv) after registration.

The extent to which the volumes match was evaluated using the cross-correlation coefficient r, calculated using Equation 5, where image intensities at pixel i are denoted by x_{ui} for the undamaged sample and x_{di} for the damaged sample. A value of 1 indicates perfect matching, whereas a value of 0 indicates no matching.

$$r = \frac{\sum(x_{ui} - \bar{x}_u)(x_{di} - \bar{x}_d)}{\sqrt{\sum(x_{ui} - \bar{x}_u)^2 \sum(x_{di} - \bar{x}_d)^2}} \tag{5}$$

The resultant cross-correlation coefficients are listed in Table 3-3 for the 4 × 4 × 4 downsampled data used for geometry and void analysis, and for the 2 × 2 × 2 downsampled data used for crack detection and DVC. The significant improvements in cross-correlation coefficients with registration indicate that the registration process is an imperative step in the analysis of a singular sample under ex-situ mechanical testing.

Table 3-3: Volume registration results - cross-correlation coefficients between undamaged and undamaged datasets.

	4 × 4 × 4 Downsampled		**2 × 2 × 2 Downsampled**	
	Unregistered	**Registered**	**Unregistered**	**Registered**
Raw Imported	0.6162	0.9162	0.5900	0.8696
3D Median Filtered	0.6492	0.9638	0.6226	0.9308
Binarized	0.6589	0.9669	0.6551	0.9639

3.3.2 Volume and Void Analysis

3.3.2.1 Geometry and Topology Analysis

Results from the geometry and topology analysis of the undamaged and damaged samples are shown in Figure 3-11. Figure 3-11(a-b) shows measurements of inner and outer diameters measured from image slices compared with the physical measurement by micrometer. Average inner diameter values from images were 38.05 ± 0.01 mm and 38.03 ± 0.01 mm for the undamaged and damaged samples respectively, indicating slight underestimation by up to 0.2%. Average outer diameter values from images were 41.29 ± 0.06 mm and 41.27 ± 0.06 mm for the undamaged and damaged samples respectively, indicating substantial overestimation by 0.7%, owing to the protrusion of the outer layer caused by the manufacturing defect. Figure 3-11(c) shows measurements of eccentricity of the inner and outer surfaces at each image slice. The inner surface was observed to become noticeably more circular over its full measured length after impact damage. This effect is illustrated in Figure 3-11(d-f), where delamination cracks induced by impact caused local inward plastic deformation, resulting in an overall shift in cross-sectional geometry.

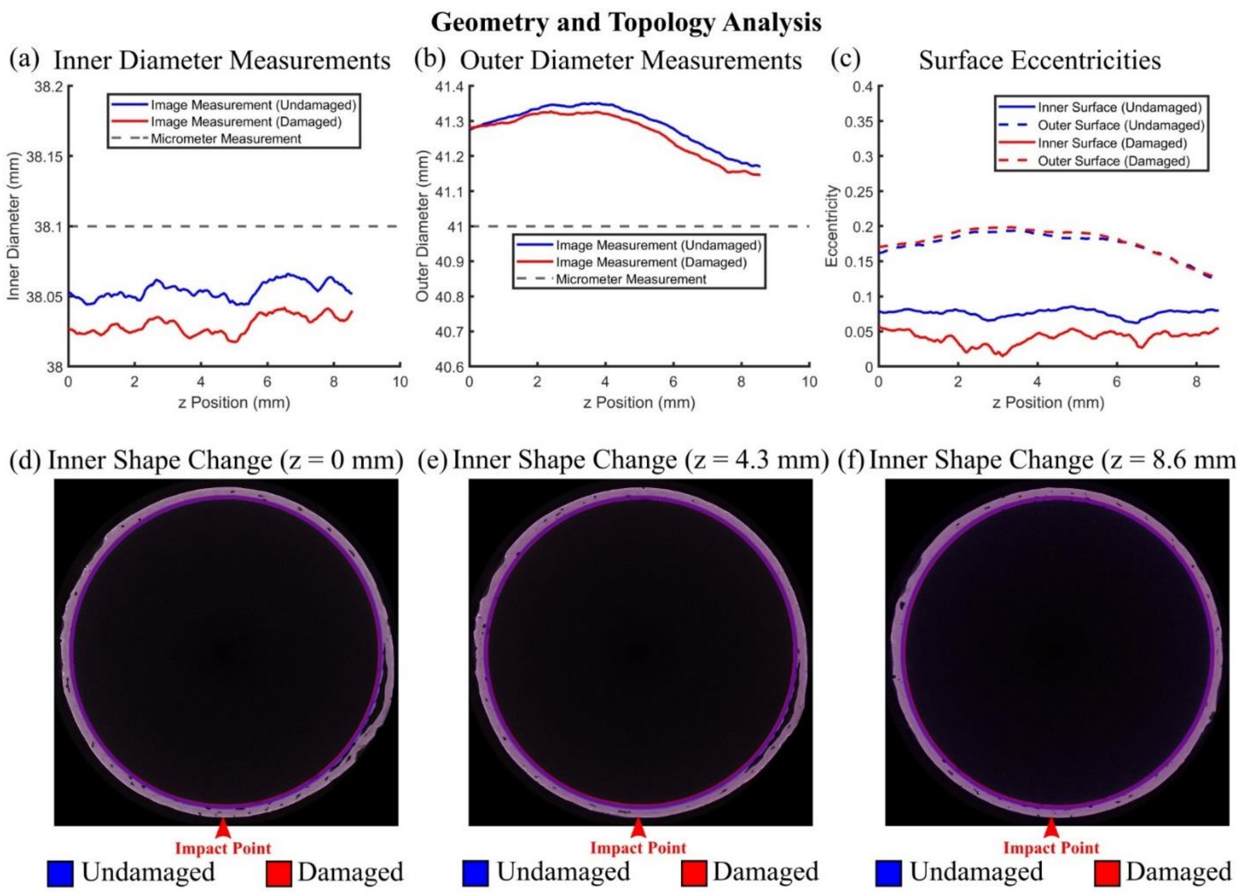

Figure 3-11: Results for topology analysis: (a) measurements of sample inner diameter over vertical position; (b) measurements of sample outer diameter over vertical position; (c) measurements of eccentricity of cross-sectional profiles over sample vertical position; (d) illustration of the inner cross-sectional profile shift at z = 0 mm; (e) at z = 4.3 mm; (f) at z = 8.6 mm.

From the t-test results shown in Table 3-4, the outer surface experienced a slight decrease in circularity, stemming from either slight plastic deformation near the region of impact, or from residual misalignment of datasets. A p-value of <0.05 was used as the criterion to indicate that a statistically significant difference exists between the undamaged and damaged samples. In contrast, the inner surface experienced a clear and significant increase in circularity due to the local plastic deformation of laminae. These topology changes demonstrate the high ductility of the material, similarly to the work by Ying et al. [42], which found the inter-ply laminate with aramid at the impact surface to have the highest ductility index among other forms of hybrid carbon-aramid woven composites. From these findings, it is expected that at higher impact energy levels, the topology shift would be more significant, and diameter measurements would be affected substantially by the larger shape changes.

Table 3-4: Paired-sample t-test results for inner and outer surface topology shifts.

	Inner Surface	**Outer Surface**
t-Test Null Hypothesis	The surfaces have no significant shift in shape after impact damage.	
Mean Eccentricity Change	-0.0350 ± 0.0080	0.0039 ± 0.0030
***t* Critical Value**	1.65	1.65
***t* Statistical Value**	-66.22	19.98
***p* Value**	< 0.001	< 0.001
95% Confidence Interval	[-0.0360, -0.0339]	[0.0035, 0.0043]

3.3.2.2 Volume Fractions

General volume measurements that were used to evaluate the void volume fractions of the sample before and after impact damage are listed in Table 3-5. The results in the context of the full sample volume are shown in Figure 3-12. The large void content of roughly 5% was largely attributed to a manufacturing defect that formed during the hand lay-up process. Excluding this defect, the void content was measured at around 1.5%. In comparison, a similar work for an aramid/epoxy braided composite by Melenka et al. [30] determined an enclosed volume fraction of 1.04% and a defect volume fraction of 2.44%. Next, a work for cellulose/bio-epoxy braided composites by Melenka et al. [31] found closed void volume fractions between 0.94% and 1.08% for two different braid angles. Additionally, a work for cellulose/hemp and cellulose/bio-epoxy braided composites by Bruni-Bossio et al. [32] found total void volume fractions ranging from 1.5% to 6.2% for various braid angles. Although much variation in measurements can occur in the presence of material defects, total void volume fractions were within expected values from literature. However, the enclosed void volume fractions that exclude the manufacturing defect were higher for the multi-layered braided composites than for the single-layered materials studied in literature. This result was attributed to the presence of layer interfaces which formed additional spaces for voids to form.

Table 3-5 also lists general statistical data of voids larger than 0.001 mm^3 for the undamaged and damaged samples. Due to the significant proportion of the void volume being occupied by the manufacturing defect, statistical results differed largely between its inclusion and exclusion.

Table 3-5: Volume measurement, general statistical data, and t-test results for the voids of the undamaged and damaged samples.

	Undamaged	Damaged
Material Volume (mm^3)	1648.7	1650.6
Void Volume (mm^3) **(Excluding Manufacturing Defect)**	83.94 (24.06)	80.96 (24.37)
Void Volume Fraction **(Excluding Manufacturing Defect)**	4.85% (1.46%)	4.69% (1.47%)
Number of Voids	482	498
Mean Void Volume (mm^3)	0.1741	0.1626

(Excluding Manufacturing Defect)	(0.0500)	(0.0491)
Standard Deviation (mm^3) **(Excluding Manufacturing Defect)**	2.7271 (0.1103)	2.5354 (0.1095)
Extent of Manufacturing Defect in Void Volume	71.33%	69.88%
t-Test Null Hypothesis	The voids had no significant size change due to impact damage. P-Value < 0.05 indicates significance	
p Value	0.36 > 0.05	

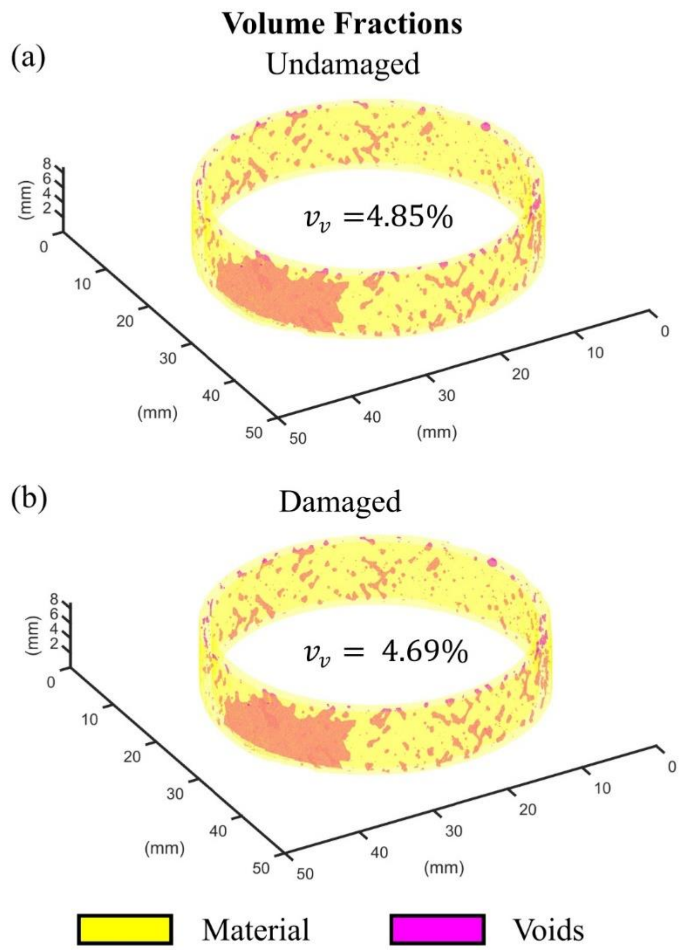

Figure 3-12: Void volume fraction results in the context of the original material volume: (a) undamaged sample; (b) damaged sample.

3.3.2.3 Void Registration and Statistics

Results from void registration and statistical analysis are shown in Figure 3-13. Figure 3-13(a) illustrates the registration the 40 largest voids in the undamaged sample, indicating that these voids shown in Figure 3-13(i) were matched within the 42 largest voids in the damaged sample shown in Figure 3-13(ii). As an example, undamaged void #21 and its corresponding damaged void #21 were compared and no clear difference in shape or volume was observed.

Figure 3-13(b) shows the statistics that followed the void registration. Figure 3-13(iii) shows the histograms of void volumes, from which it was found that 25% of voids were larger than 0.05 mm^3, whereas 53% of voids were smaller than 0.01 mm^3. Figure 3-13(iv) shows the histograms of void positions with respect to the sample centre. The vertical lines in the plot show the inner and outer radii from micrometer measurements for reference. Two peaks were found at positions of one-third and two-thirds between the inner and outer radii, indicating that the voids were primarily concentrated at the ply interfaces. Figure 3-13(v) shows the histograms of void sphericities, indicating that 29% of voids had a spherical profile with a sphericity value of 1, whereas 29% of voids had a sphericity of less than 0.8. Figure 3-13(vi) shows the percentage volume change of the voids shown in Figure 3-13(a). The voids that showed the most significant volume changes were situated along the edges of the reconstructed volume. As such, any residual misalignment of datasets would result in sections of such voids to become either revealed or occluded.

A t-test was performed to determine whether void volume change between the two datasets was universally evident. The results, shown in Table 3-5, suggested that the impact damage did not cause any significant void enlargement.

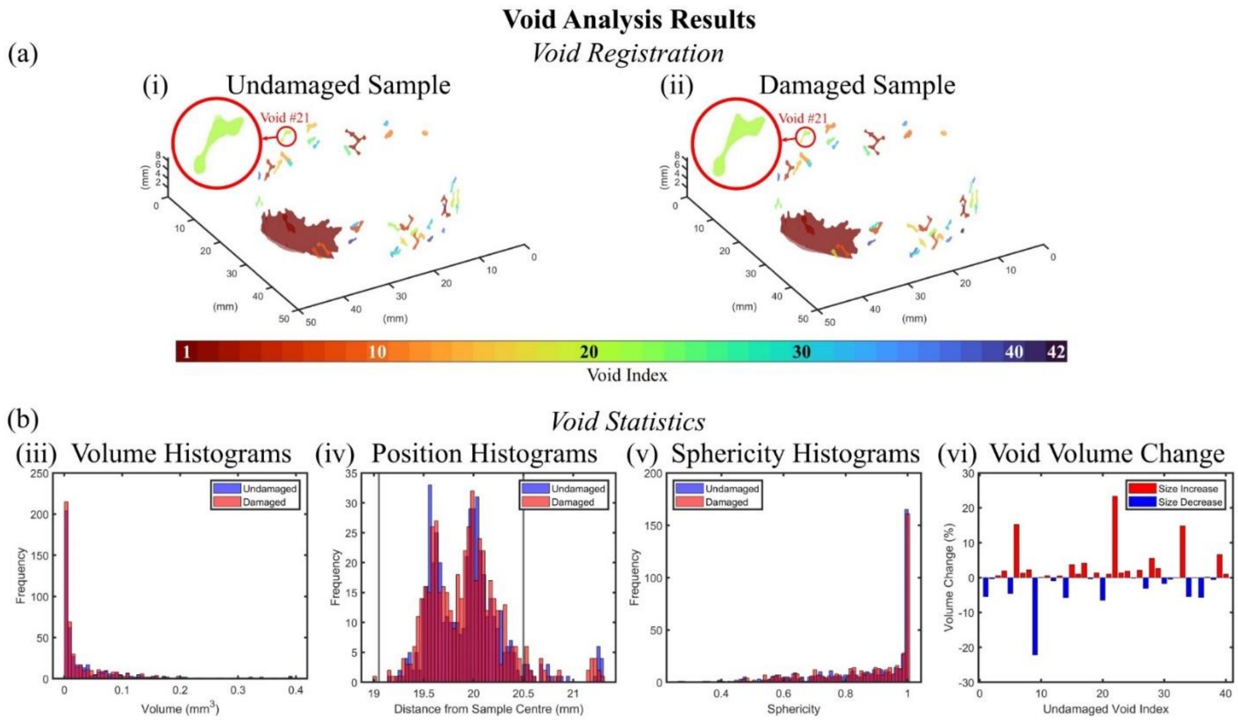

Figure 3-13: Results from individual void analysis: (a) void registration: (i) 40 largest undamaged voids; (ii) corresponding registered damaged voids; (b) void statistical analysis; (iii) histograms of void volumes; (iv) histograms of void positions from sample centre; (v) histograms of void sphericities; (vi) volume change percentages of the largest voids after impact.

3.3.2.4 Crack Detection

Results from the crack detection algorithm are shown in Figure 3-14, and key data metrics are listed in Table 3-6. Figure 3-14(a) shows the crack in the context of the full sample volume. The crack was observed to propagate mostly tangentially along the circumference of the sample cross-section, as well as enclose the voids at the impact site. The impact cracks were primarily in the form of delamination, agreeing with the findings of Tian et al. [43], which concluded that this inter-ply configuration allows the aramid layers to disperse the impact energy tangentially over a larger area, thereby advancing delamination cracks and limiting failure of the internal carbon fibres. Furthermore, the largest voids at the layer interfaces near the impact site were the primary nucleation site of damage cracks, agreeing with the findings of Lambert et al. [22], which found a correlation between the size of the largest void at critical locations and fatigue life to crack initiation, which can consequently predict the likelihood of crack initiation and extent of its propagation under applied impact energy. Additionally, Maragoni et al. [18] demonstrated a correlation between void area fraction and fatigue life degradation, which can be used again to predict similar effects for impact resistance. Figure 3-14(b) shows measurements of crack arc length and area at each position along the length of the sample. The region with the highest arc lengths, which was located around the lower half of the sample shown in Figure 3-14(a), was presumed to be nearest the true location of impact. Figure 3-14(c) shows the histogram of crack voxel positions with respect to the sample centre. Like the void positions in Figure 3-13(iv), the crack was concentrated at two peak positions, particularly at the ply interfaces, providing quantitative indication that delamination was the primary damage mechanism in the sample. Nearly three-quarters of the crack were situated in the inner half through the thickness of the sample.

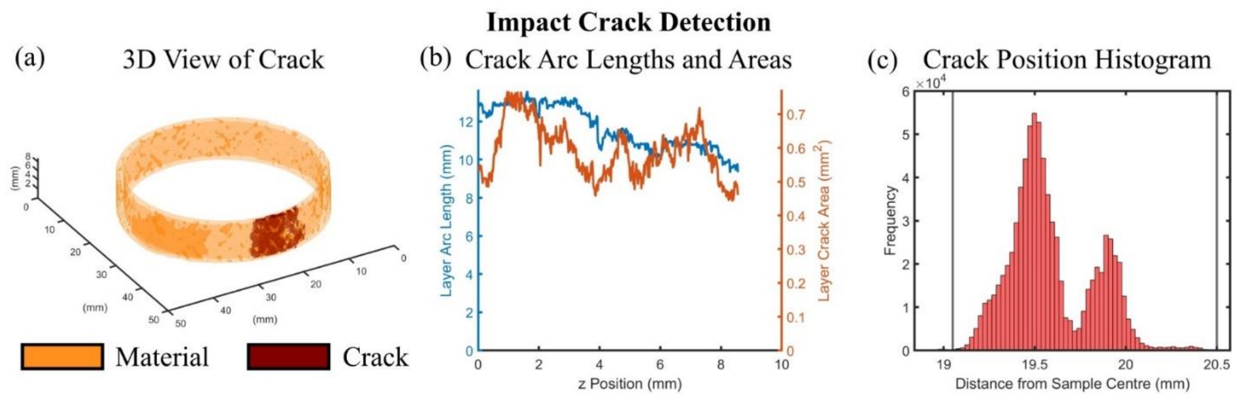

Figure 3-14: Results from impact crack detection: (a) detected crack in the context of the original material volume; (b) measures of crack arc lengths and areas over sample vertical position; (c) histogram of crack voxel distances from sample centre.

Table 3-6: General statistical data of the detected impact crack.

Mean Crack Arc Length (mm)	11.67 ± 1.15
Crack Extent Along Nominal Circumference	$9.4\% \pm 0.9\%$
Crack Volume (mm^3)	5.07
Crack Volume Fraction	0.29%

3.3.2.5 Application of Crack Identification to Fracture Mechanics

For braided composites, FEA is a common means of applying fracture mechanics. This approach was used recently by Shi et al. [54] for 3D braided composite notched beams under SHPB impact testing. The numerical model used a collection of unit cells of the braiding pattern, referred to as representative volume elements (RVE), created by microstructure modelling of the fibre and matrix materials. The time-dependent load $P(t)$ of the specimen under SHPB impact was calculated from the modulus of elasticity E, cross-sectional area A, and strain gauge signals of the input wave $\varepsilon_I(t)$ and reflected wave $\varepsilon_R(t)$ using Equation 6 [55]. The findings from FEA were in good agreement with experimental results and demonstrated that the employed method can be used for in-depth application of fracture mechanics in braided composites.

$$P(t) = EA[\varepsilon_I(t) + \varepsilon_R(t)] \tag{6}$$

However, in this work, only the impact energy of the striker bar was known, and no strain gauge measurements were acquired. As proposed future work, the multi-layered 2D braided composite can be impact tested with strain gauges instrumented to the incident and transmission bars. Additionally, FEA can be performed using a geometric model developed by Gholami and Melenka [56], [57] to create RVE geometries. Comparison with a corresponding μCT model showed that a geometric model error of less than 1% was achieved using particle swarm optimization [57], which demonstrates good applicability to numerical modelling of the SHPB testing performed in this work.

3.3.3 Digital Volume Correlation

The DVC method allows for internal strain fields to be observed within a sample. Figure 3-15 shows results from DVC processing of the impacted side of the sample as normal y-strain maps along x-y image slices. The maximum positive strain of 0.16 mm/mm was mostly situated around regions of cracking. The maximum negative strain of 0.16 mm/mm was mostly situated around the largest voids in the region of interest.

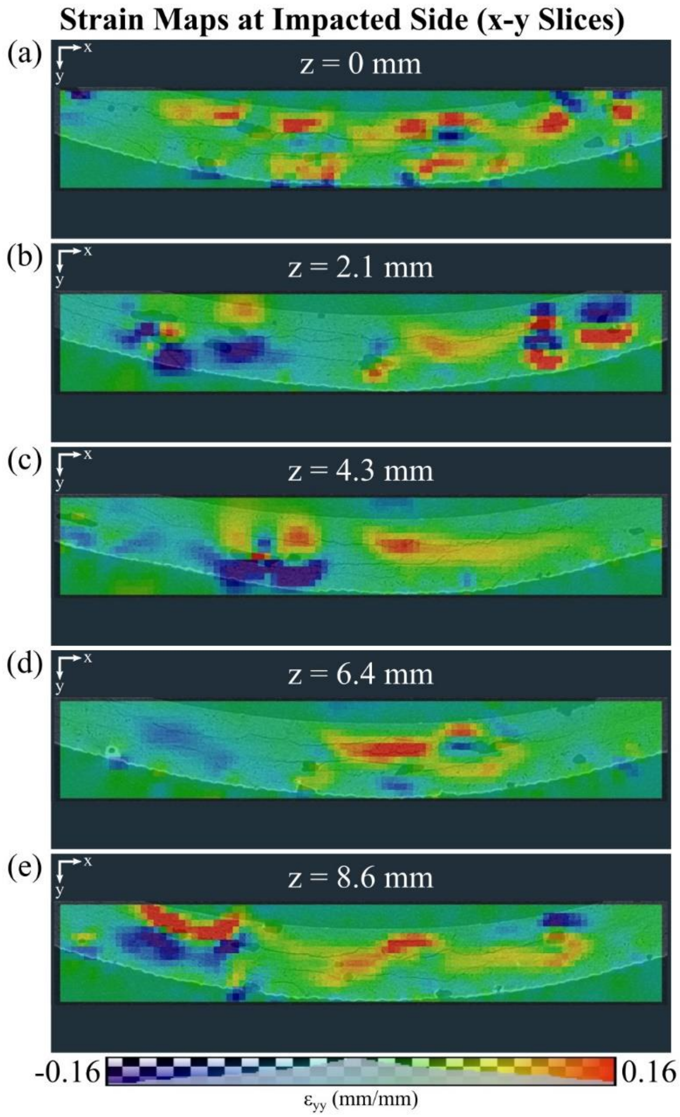

Figure 3-15: Normal y-strain maps of x-y slices for the impacted side at: (a) z = 0 mm; (b) z = 2.1 mm; (c) z = 4.3 mm; (d) z = 6.4 mm; (e) z = 8.6 mm.

Figure 3-16 shows the normal y-strain measurements along x-z image slices corresponding to each of the material plies. Figure 3-16(a) illustrates the positions along the y-axis from which each slice was extracted. From the strain maps in Figure 3-16(b-d), the highest concentrations of strain were found in the middle layer of the material. Additionally, compressive strains were concentrated in regions with large voids at each layer, whereas tensile strain concentrations relied on patterns found along x-y slices in Figure 3-15 rather than along x-z slices.

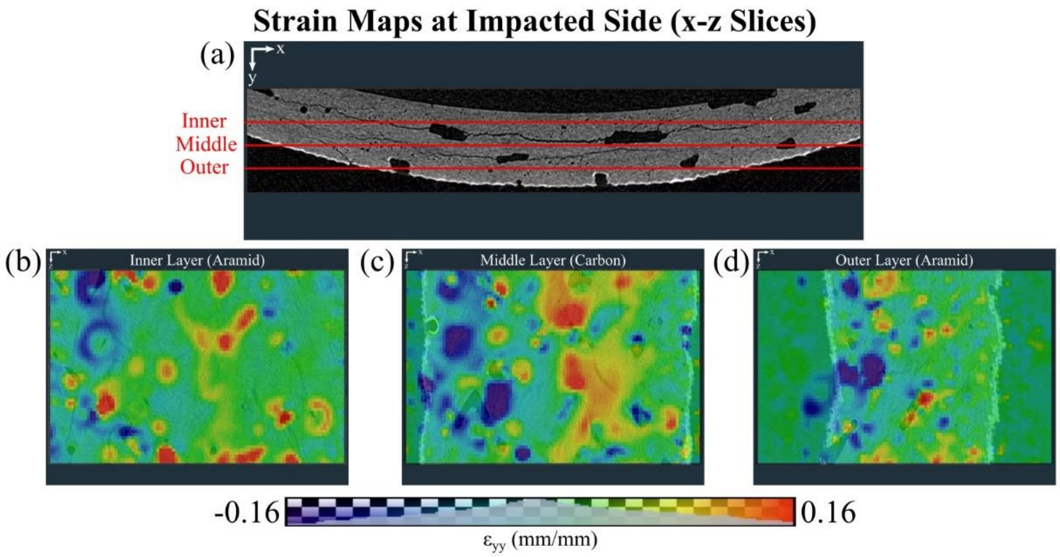

Figure 3-16: DVC measurements of x-z slices for the impacted side: (a) x-y view with locations of selected slices for each material layer; (b) normal y-strain maps of the inner layer; (c) the middle layer; (d) the outer layer.

Figure 3-17 shows the normal y-strain measurements for both the impacted side and its opposite side along x-y image slices. The strain maps shown in Figure 3-17(a) show that unlike the impacted side of the sample, where the strain profiles shown in Figure 3-15 correlated with the impact damage, the opposite side did not experience significant deformation. The strain measurements are also shown as line plots through the centres of the volumes of interest along the x-direction in Figure 3-17(b). At the opposite side, short peaks in measurements as shown in Figure 3-17(iv-vi) were situated near voids that were large enough to cause loss of correlation.

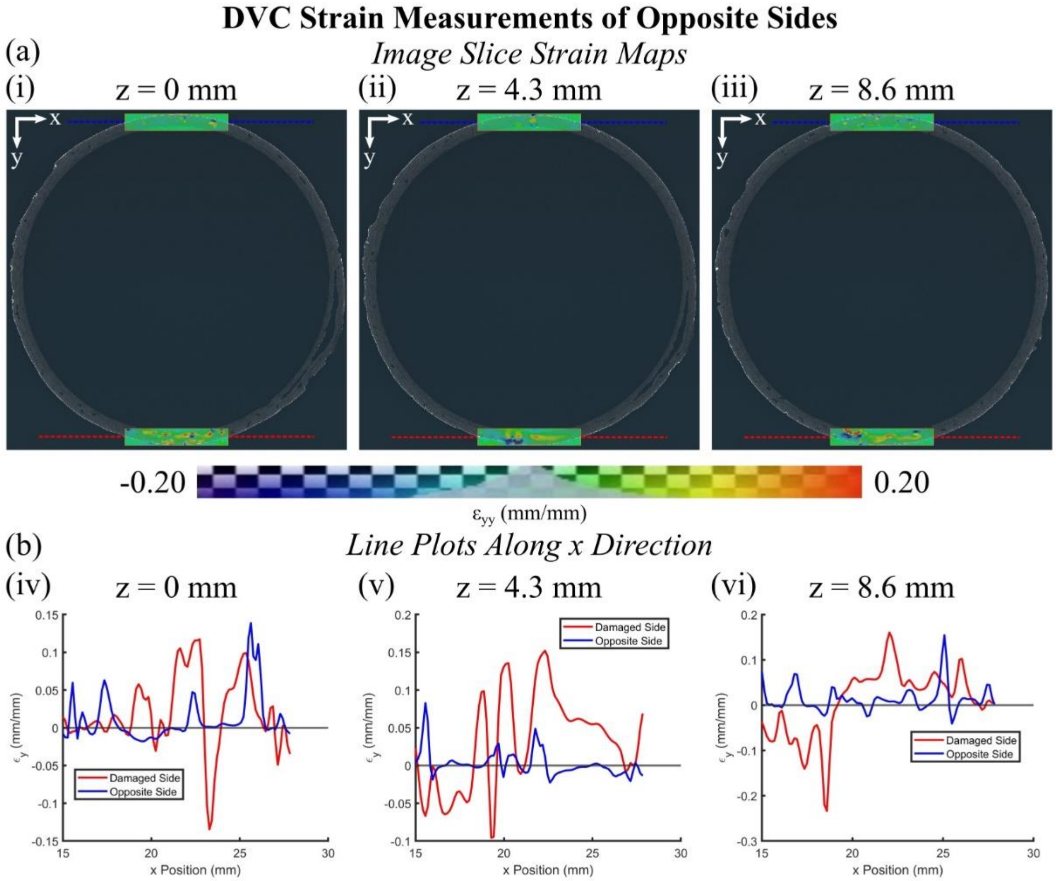

Figure 3-17: Normal y-strain measurements of the impacted and opposite sides: (a) maps of x-y slices at: (i) z = 0 mm; (ii) z = 4.3 mm; (iii) z = 8.6 mm; (b) line plots along dashed lines illustrated in image slices at: (iv) z = 0 mm; (v) z = 4.3 mm; (vi) z = 8.6 mm.

The DVC analysis shows that the impact energy that reached the middle carbon layer of the material was mostly converted to plastic deformation rather than internal fracture, further demonstrating the role of the surrounding aramid layers in dispersing energy along the ply interfaces. This section highlights the advantages of the DVC method for assessing damage and internal strain fields of composite structures.

3.4 Conclusions

In this study, the impact performance of a 2D tubular braided inter-ply hybrid carbon-aramid polymer matrix composite material was investigated. Impact testing was performed using a split Hopkinson pressure bar (SHPB) at an impact energy level that induced barely visible impact damage (BVID). Quantitative analysis was performed on the internal structure of the sample from micro-computed tomography (μCT) imaging. Image registration was performed to align datasets to allow for effective characterization of void content and distribution, geometry and topology change, and impact crack development. An algorithm was developed to match voids between the undamaged and damaged samples, such that each void could be locally quantified to allow for statistical analysis of the effect of the applied impact energy on the properties of the voids. Another algorithm was developed to detect the impact cracks in the damaged sample amid the voids at the impact site. Finally, digital volume correlation (DVC) was used to measure volumetric deformations and strains at representative volumes of interest. The findings of this work are summarised by the following:

(1) Image registration provided a suitable cross-correlation coefficient, affirming this process as a crucial step in accurately comparing the undamaged and damaged datasets.

(2) The void volume fraction, the majority of which occupied by a manufacturing defect from the hand lay-up process, remained unchanged from the applied impact energy.

(3) Statistical analysis demonstrated that the sizes of individual voids also remained unchanged after impact, inferring that the impact energy was expended towards the development of cracks rather than the enlargement of voids.

(4) The inner and outer surfaces experienced non-negligible plastic deformation due to impact, owing to the high ductility index of the laminate configuration. The inner surface

experienced the highest plastic deformation, specifically at the impact site, owing to the delamination cracks causing inward displacement of plies.

(5) Impact cracks were largely in the form of delamination, demonstrating a property of aramid fibres where they effectively distribute energy over a larger tangential area to minimize the energy experienced by the internal carbon layer.

(6) Large voids at the impact site were the primary sites for crack initiation, dictating the extent of tangential crack propagation by measure of arc length, and the density of damage along the radial direction by measure of crack area.

(7) Volumetric strain measurements by DVC show that tensile strain concentrations followed the profiles of delamination cracks and that damage in the middle carbon layer largely manifested as plastic deformation.

3.5 Acknowledgements

The authors gratefully acknowledge the support from Dr. Aleksander Czekanski for providing the SHPB apparatus, CMC Microsystems for providing the software for DVC, and the financial support from the Natural Sciences and Engineering Research Council of Canada RGPIN-2018-05899.

3.6 Supplemental Files

MATLAB code used for image processing and data analysis, reconstructed images of the tubular braided composite, and scan logs are available in the data repository (Federated Research Data Repository: https://doi.org/10.20383/103.0770).

3.7 References

[1] C. Ayranci and J. Carey, “2D braided composites: A review for stiffness critical applications,” *Compos Struct*, vol. 85, no. 1, pp. 43–58, Sep. 2008, doi: 10.1016/J.COMPSTRUCT.2007.10.004.

[2] G. W. Melenka and C. Ayranci, “Advanced measurement techniques for braided composite structures: A review of current and upcoming trends,” *J Compos Mater*, vol. 54, no. 25, pp. 3895–3917, Oct. 2020, doi: 10.1177/0021998320903105.

[3] D. K. Rajak *et al.*, “Impact of fiber reinforced polymer composites on structural joints of tubular sections: A review,” *Thin-Walled Structures*, vol. 180, p. 109967, Nov. 2022, doi: 10.1016/J.TWS.2022.109967.

[4] G. A. Bibo and P. J. Hogg, “The role of reinforcement architecture on impact damage mechanisms and post-impact compression behaviour,” *J Mater Sci*, vol. 31, no. 5, pp. 1115–1137, Mar. 1996, doi: 10.1007/BF00353091.

[5] H. Zhou, Z. Pan, R. K. Gideon, B. Gu, and B. Sun, “Experimental and numerical investigation of the transverse impact damage and deformation of 3-D circular braided composite tubes from meso-structure approach,” *Compos B Eng*, vol. 86, pp. 243–253, Feb. 2016, doi: 10.1016/J.COMPOSITESB.2015.10.019.

[6] S. Del Rosso, L. Iannucci, and P. T. Curtis, “On the ballistic impact response of microbraid reinforced polymer composites,” *Compos Struct*, vol. 137, pp. 70–84, Mar. 2016, doi: 10.1016/J.COMPSTRUCT.2015.10.031.

[7] A. VanderKlok *et al.*, “An experimental investigation into the high velocity impact responses of S2-glass/SC15 epoxy composite panels with a gas gun,” *Int J Impact Eng*, vol. 111, pp. 244–254, Jan. 2018, doi: 10.1016/J.IJIMPENG.2017.10.002.

[8] Y. Yang, L. Zhang, L. Guo, W. Zhang, J. Zhao, and W. Xie, “Dynamic response and research of 3D braided Carbon Fiber Reinforced Plastics subjected to ballistic impact loading,” *Compos Struct*, vol. 206, pp. 578–587, Dec. 2018, doi: 10.1016/J.COMPSTRUCT.2018.08.021.

[9] A. C. Jackson, “Development of textile composite preforms for aircraft primary structures,” in *Collection of Technical Papers - AIAA/ASME/ASCE/AHS/ASC Structures, Structural Dynamics and Materials Conference*, 1994, pp. 1008 – 1012. doi: 10.2514/6.1994-1430.

[10] M. A. Kuykendall, “Braided frame testing and analysis,” in *International SAMPE Technical Conference*, 1994, pp. 746 – 758.

[11] D. S. Brookstein, “Processing advanced braided composites,” in *American Society of Mechanical Engineers, Materials Division (Publication) MD*, 1988, pp. 33 – 36.

[12] D. Brookstein, “Structural applications of advanced braided composites,” *in: Proceedings SPE/APC ’88. Advanced Polymer Composites for Structural Applications. Los Angeles, 14-17 November*, pp. 415 – 424, 1988.

[13] A. K. Munjal and P. F. Maloney, “Braining for improving performance and reducing manufacturing costs of composite structures for aerospace applications,” in *National SAMPE Technical Conference*, 1990, pp. 1231 – 1242.

[14] D. Branscomb, D. Beale, and R. Broughton, “New Directions in Braiding,” *J Eng Fiber Fabr*, vol. 8, no. 2, pp. 11–24, Jun. 2013, doi: 10.1177/155892501300800202.

[15] G. W. Melenka *et al.*, “Manufacturing processes for braided composite materials,” *Handbook of Advances in Braided Composite Materials: Theory, Production, Testing and Applications*, pp. 47–153, Jan. 2017, doi: 10.1016/B978-0-08-100369-5.00003-9.

[16] H. Zhou, W. Zhang, T. Liu, B. Gu, and B. Sun, “Finite element analyses on transverse impact behaviors of 3-D circular braided composite tubes with different braiding angles,” *Compos Part A Appl Sci Manuf*, vol. 79, pp. 52–62, Dec. 2015, doi: 10.1016/J.COMPOSITESA.2015.09.012.

[17] L. Wu, W. Wang, Q. Jiang, J. H. Lin, and Y. Tang, “Illustrating hybrid effect and damage evolution of carbon/aramid braided composite under low-velocity impact,” *Compos Struct*, vol. 245, p. 112372, Aug. 2020, doi: 10.1016/J.COMPSTRUCT.2020.112372.

[18] L. Maragoni, P. A. Carraro, M. Peron, and M. Quaresimin, “Fatigue behaviour of glass/epoxy laminates in the presence of voids,” *Int J Fatigue*, vol. 95, pp. 18–28, Feb. 2017, doi: 10.1016/J.IJFATIGUE.2016.10.004.

[19] Z. Zhao *et al.*, “Effects of loading rate and loading direction on the compressive failure behavior of a 2D triaxially braided composite,” *Int J Impact Eng*, vol. 156, p. 103928, Oct. 2021, doi: 10.1016/J.IJIMPENG.2021.103928.

[20] J. Hsieh, *Computed Tomography: Principles, Design, Artifacts, and Recent Advances*. SPIE PRESS, 2015. doi: 10.1117/3.2197756.

[21] S. C. Garcea, Y. Wang, and P. J. Withers, “X-ray computed tomography of polymer composites,” *Compos Sci Technol*, vol. 156, pp. 305–319, Mar. 2018, doi: 10.1016/J.COMPSCITECH.2017.10.023.

[22] J. Lambert, A. R. Chambers, I. Sinclair, and S. M. Spearing, “3D damage characterisation and the role of voids in the fatigue of wind turbine blade materials,” *Compos Sci Technol*, vol. 72, no. 2, pp. 337–343, Jan. 2012, doi: 10.1016/J.COMPSCITECH.2011.11.023.

[23] M. Ueda, K. Mimura, and T.-K. Jeong, “In situ observation of kink-band formation in a unidirectional carbon fiber reinforced plastic by X-ray computed tomography imaging,” *Advanced Composite Materials*, vol. 25, no. 1, pp. 31–43, Jan. 2016, doi: 10.1080/09243046.2014.973173.

[24] K. M. Jespersen, J. Zangenberg, T. Lowe, P. J. Withers, and L. P. Mikkelsen, “Fatigue damage assessment of uni-directional non-crimp fabric reinforced polyester composite using X-ray computed tomography,” *Compos Sci Technol*, vol. 136, pp. 94–103, Nov. 2016, doi: 10.1016/J.COMPSCITECH.2016.10.006.

[25] F. Léonard, J. Stein, C. Soutis, and P. J. Withers, “The quantification of impact damage distribution in composite laminates by analysis of X-ray computed tomograms,” *Compos Sci Technol*, vol. 152, pp. 139–148, Nov. 2017, doi: 10.1016/J.COMPSCITECH.2017.08.034.

[26] F. Yoshinaka *et al.*, “Characterization of internal fatigue crack initiation in Ti-6Al-4V alloy via synchrotron radiation X-ray computed tomography,” *Fatigue Fract Eng Mater Struct*, Feb. 2023, doi: 10.1111/ffe.13957.

[27] Y. Chai *et al.*, "Damage evolution in braided composite tubes under torsion studied by in-situ X-ray computed tomography," *Compos Sci Technol*, vol. 188, p. 107976, Mar. 2020, doi: 10.1016/J.COMPSCITECH.2019.107976.

[28] L. Shi, Z. Wu, X. Cheng, Z. Pan, and Y. Yuan, "Transverse impact response of hybrid biaxial/uniaxial braided composite tubes," *Eng Struct*, vol. 244, p. 112816, Oct. 2021, doi: 10.1016/J.ENGSTRUCT.2021.112816.

[29] Z. Wu, S. Qin, P. Zhang, Z. Pan, X. Hu, and L. Shi, "Damage evolution in braided composite tubes under axial compression studied by combining infrared thermography and X-ray computed tomography," *Compos Struct*, vol. 307, p. 116634, Mar. 2023, doi: 10.1016/J.COMPSTRUCT.2022.116634.

[30] G. W. Melenka, E. Lepp, B. K. O. Cheung, and J. P. Carey, "Micro-computed tomography analysis of tubular braided composites," *Compos Struct*, vol. 131, pp. 384–396, Nov. 2015, doi: 10.1016/J.COMPSTRUCT.2015.05.057.

[31] G. W. Melenka, B. M. Bruni-Bossio, C. Ayranci, and J. P. Carey, "Examination of voids and geometry of bio-based braided composite structures," *IOP Conf Ser Mater Sci Eng*, vol. 406, Sep. 2018, doi: 10.1088/1757-899X/406/1/012012.

[32] B. M. Bruni-Bossio, G. W. Melenka, C. Ayranci, and J. P. Carey, "Micro-computed tomography analysis of natural fiber and bio-matrix tubular-braided composites," *J Compos Mater*, vol. 53, no. 28–30, pp. 4003–4013, Dec. 2019, doi: 10.1177/0021998319853023.

[33] C. Unlusoy and G. W. Melenka, "Flexural testing of cellulose fiber braided composites using three dimensional digital image correlation," *Compos Struct*, vol. 230, p. 111538, Dec. 2019, doi: 10.1016/J.COMPSTRUCT.2019.111538.

[34] H. Zhou, C. Li, L. Zhang, B. Crawford, A. S. Milani, and F. K. Ko, “Micro-XCT analysis of damage mechanisms in 3D circular braided composite tubes under transverse impact,” *Compos Sci Technol*, vol. 155, pp. 91–99, Feb. 2018, doi: 10.1016/J.COMPSCITECH.2017.11.025.

[35] G. Fang, C. Chen, S. Yuan, S. Meng, and J. Liang, “Micro-tomography based Geometry Modeling of Three-Dimensional Braided Composites,” *Applied Composite Materials*, vol. 25, no. 3, pp. 469–483, Jun. 2018, doi: 10.1007/s10443-017-9630-8.

[36] X. Liu, X. Wang, D. Zhang, and K. Qian, “Effect of voids on fatigue damage propagation in 3D5D braided composites revealed via automated algorithms using X-ray computed tomography,” *Int J Fatigue*, vol. 158, p. 106778, May 2022, doi: 10.1016/J.IJFATIGUE.2022.106778.

[37] X. Liu, D. Zhang, C. Mao, X. Wang, and K. Qian, “Full-field progressive fatigue damage of 3D5D braided composites with yarn-reduction: visualization, classification, and quantification,” *Compos Sci Technol*, vol. 218, p. 109214, Feb. 2022, doi: 10.1016/J.COMPSCITECH.2021.109214.

[38] B. Yu, R. Blanc, C. Soutis, and P. J. Withers, “Evolution of damage during the fatigue of 3D woven glass-fibre reinforced composites subjected to tension–tension loading observed by time-lapse X-ray tomography,” *Compos Part A Appl Sci Manuf*, vol. 82, pp. 279–290, Mar. 2016, doi: 10.1016/J.COMPOSITESA.2015.09.001.

[39] V. M. Karbhari, J. E. Haller, P. K. Falzon, and I. Herszberg, “Post-impact crush of hybrid braided composite tubes,” *Int J Impact Eng*, vol. 22, no. 4, pp. 419–433, Apr. 1999, doi: 10.1016/S0734-743X(98)00059-1.

[40] M. P. F. Sutcliffe, C. Monroy Aceves, W. J. Stronge, R. S. Choudhry, and A. E. Scott, “Moderate speed impact damage to 2D-braided glass–carbon composites,” *Compos Struct*, vol. 94, no. 5, pp. 1781–1792, Apr. 2012, doi: 10.1016/J.COMPSTRUCT.2011.12.026.

[41] D. Chen, Q. Luo, M. Meng, Q. Li, and G. Sun, “Low velocity impact behavior of interlayer hybrid composite laminates with carbon/glass/basalt fibres,” *Compos B Eng*, vol. 176, Nov. 2019, doi: 10.1016/j.compositesb.2019.107191.

[42] S. Ying, T. Mengyun, R. Zhijun, S. Baohui, and C. Li, “An experimental investigation on the low-velocity impact response of carbon–aramid/epoxy hybrid composite laminates,” *Journal of Reinforced Plastics and Composites*, vol. 36, no. 6, pp. 422–434, Mar. 2017, doi: 10.1177/0731684416680893.

[43] J. Tian, T. Xu, L. An, S. Wang, Y. Tan, and G. Chen, “Study on behavior and mechanism of low-velocity impact and post-impact flexural properties of carbon-aramid/epoxy resin laminated composites,” *Compos Struct*, vol. 300, p. 116166, Nov. 2022, doi: 10.1016/J.COMPSTRUCT.2022.116166.

[44] R. Seltzer, C. González, R. Muñoz, J. Llorca, and T. Blanco-Varela, “X-ray microtomography analysis of the damage micromechanisms in 3D woven composites under low-velocity impact,” *Compos Part A Appl Sci Manuf*, vol. 45, pp. 49–60, Feb. 2013, doi: 10.1016/J.COMPOSITESA.2012.09.017.

[45] V. Mazars *et al.*, “Damage investigation and modeling of 3D woven ceramic matrix composites from X-ray tomography in-situ tensile tests,” *Acta Mater*, vol. 140, pp. 130–139, Nov. 2017, doi: 10.1016/j.actamat.2017.08.034.

[46] R. Lorenzoni *et al.*, “Combined mechanical and 3D-microstructural analysis of strain-hardening cement-based composites (SHCC) by in-situ X-ray microtomography,” *Cem Concr Res*, vol. 136, Oct. 2020, doi: 10.1016/j.cemconres.2020.106139.

[47] C. Liu, Y. Chen, D. Shi, J. Marrow, X. Jing, and X. Yang, “In situ investigation of failure in 3D braided SiCf/SiC composites under flexural loading,” *Compos Struct*, vol. 270, Aug. 2021, doi: 10.1016/j.compstruct.2021.114067.

[48] A. Goyal and G. W. Melenka, “Investigation of Carbon- Aramid Hybrid Braided Composites using Digital Volume Correlation,” *Compos Struct*, Jun. 2023, doi: 10.1016/j.compstruct.2023.117207.

[49] J. Holmes, S. Sommacal, Z. Stachurski, R. Das, and P. Compston, “Digital image and volume correlation with X-ray micro-computed tomography for deformation and damage characterisation of woven fibre-reinforced composites,” *Compos Struct*, vol. 279, Jan. 2022, doi: 10.1016/j.compstruct.2021.114775.

[50] J. Wang, W. Xie, F. Yi, S. Liu, and S. Meng, “Numerical simulation on fracture mechanisms of CFRP with barely visible impact damage by hail impact,” *Compos Struct*, vol. 305, Feb. 2023, doi: 10.1016/j.compstruct.2022.116499.

[51] B. J. Blinzler and W. K. Binienda, “Macromechanical Approach to Modeling Barely Visible Damage in Braided Composites,” *J Aerosp Eng*, vol. 27, no. 3, pp. 466–472, May 2014, doi: 10.1061/(ASCE)AS.1943-5525.0000375.

[52] C. Wang, Z. Chen, A. Roy, and V. V. Silberschmidt, “Energy absorption of composite shin-guard structure under low-velocity impacts,” in *Dynamic Deformation, Damage and*

Fracture in Composite Materials and Structures, Elsevier, 2023, pp. 623–637. doi: 10.1016/B978-0-12-823979-7.00021-1.

[53] H. Kolsky, "An Investigation of the Mechanical Properties of Materials at very High Rates of Loading," *Proceedings of the Physical Society. Section B*, vol. 62, no. 11, pp. 676–700, Nov. 1949, doi: 10.1088/0370-1301/62/11/302.

[54] B. Shi, S. Liu, A. Siddique, Y. Du, B. Sun, and B. Gu, "Impact fracture behaviors of three-dimensional braided composite U-notch beam subjected to three-point bending," *International Journal of Damage Mechanics*, vol. 28, no. 3, pp. 404–426, Mar. 2019, doi: 10.1177/1056789518772619.

[55] J. Fernández-Sáez, L. Rubio, S. De Luna, J. L. Pérez-Castellanos, and C. Navarro, "Determination of dynamic fracture initiation toughness of linear elastic materials," *Revista de Metalurgia*, vol. 37, no. 1, pp. 34–48, Feb. 2001, doi: 10.3989/revmetalm.2001.v37.i1.439.

[56] A. Gholami and G. W. Melenka, "Finite element analysis of 2-D tubular braided composite based on geometrical models to study mechanical performances," *Mechanics of Advanced Materials and Structures*, vol. 29, no. 28, pp. 7542–7558, 2022, doi: 10.1080/15376494.2021.2001879.

[57] A. Gholami and G. W. Melenka, "Studying the geometrical models of tubular braided composite using micro computed tomography and particle swarm optimization," *Compos B Eng*, vol. 260, Jul. 2023, doi: 10.1016/j.compositesb.2023.110758.

Chapter 4 Conclusions, Recommendations, and Future Work

4.1 Conclusions

This thesis aimed to use μCT to assess 2D tubular hybrid braided composites subjected to impact testing. First, a comprehensive introduction of fundamentals and a review of the current literature was presented, providing key background information on composites and braided composites, high strain rate testing, and non-destructive testing techniques. Composites have become a viable alternative to traditional materials due to advantages such as favourable ratios of strength and stiffness to weight and tailorable properties. Braided composites use an architecture of interwoven fibres that interact under loading to improve mechanical performance. However, braided composites are complex due to material heterogeneity and anisotropy, as well as the sensitivity of properties to imperfections and damage. As such, these materials are not sufficiently characterized by traditional measurement methods such as strain gauges.

Impact response is a critical factor in designing braided composites for high-performance applications, which can be assessed using SHPB testing. For braided composites, SHPB testing has been performed largely for 3D braid architectures, as these materials have through-thickness reinforcement resulting in high impact performance. However, 3D braided composites require specialized equipment for manufacturing and are costly, thus having limited feasibility for commercial applications. In contrast, 2D braided composites are more cost-effective and commercially available but have limited supporting literature on impact response by SHPB testing.

The existing literature on SHPB testing of braided composites was presented and summarized in Chapter 2.

A thorough assessment of impact performance in materials requires an investigation of internal features and their changes before and after impact loading. For this task, materials can be assessed on a volumetric basis using an X-ray based imaging technique such as µCT. For braided composites that contain a network of voids, a challenge is presented in accurately segmenting impact damage due to its tendency to propagate towards voids. This work was focused on a rapid method of quantifying the impact behaviours of 2D tubular braided composites by assessing the development of material damage and changes to material geometry and voids caused by impact loading.

A critical step in achieving this goal of rapidly characterizing the impact response of braided composite structures is the development of an algorithm to process µCT images of a sample and extract key properties. This work developed an algorithm based on image processing techniques and statistical analysis for automated quantification of geometry, voids, and damage from volumetric data. The details of the methodology were presented in Chapter 3. First, a 2D tubular hybrid braided composite sample was manufactured using the hand lay-up method, then scanned by µCT to obtain a reference volume. Next, the sample was fixed at its ends before undergoing transverse impact loading by SHPB testing. The sample was then scanned again by µCT to obtain a target volume. The reference and target volumes were aligned using 3D image registration. The reference and target volumes underwent various image processing and segmentation techniques for identifying and extracting individual features. First, geometries of the inner and outer surfaces were acquired from both volumes to determine the extent of geometry change caused by plastic deformation. Next, a void registration algorithm was developed, where voids were extracted from both volumes, then individually matched between datasets using similarity metrics based on location and size. For each void, the extent of volume change was acquired. Paired-sample t-tests were performed to determine whether the applied impact damage caused overall geometry change and void enlargement within the sample. Then, a crack detection algorithm was developed using the target volume, where further image processing and segmentation were performed to identify and extract the network of thin cracks that developed from impact loading. Properties such as arc length, cross-sectional area, and position along the radius of the tube were extracted to determine the extent of impact damage along the circumference, and to estimate the dominant damage modes of the composite structure. Finally, DVC was performed on reduced target volume regions representing the impacted and the opposite sides. This technique was used to measure impact-induced strains to supplement findings from the crack detection algorithm.

The 2D tubular braided composite sample, which consisted of a hybrid lay-up of aramid over carbon over aramid in a $[\pm 40°]_3$ configuration, was found to have a total void volume fraction between 4.7% and 4.9%, as the sample contained a defect caused by ply wrinkling from the manufacturing process. Excluding this manufacturing defect, the void volume fraction was measured to be around 1.5%, which was expected for braided composites manufactured by hand lay-up.

It was determined that the applied impact energy induced sufficient plastic deformation to cause overall changes in surface geometries. Measurements of eccentricity for the inner and outer regions of the sample were compared by t-tests, where it was found that the outer surface experienced a slight increase in eccentricity. In contrast, the inner surface experienced a substantial decrease in eccentricity due to impact.

Results from void registration and analysis provided several key findings. First, the voids were mostly situated along the ply interfaces, which formed naturally resin-rich regions. Next, the voids were mostly spherical, with only 29% of voids having a sphericity of less than 0.8. Finally, the impact loading did not cause significant change to void volumes as determined by a t-test.

Results from crack detection determined that the impact damage occupied 0.3% of the total material volume and spanned 9.4% of the nominal circumference of the tubular structure. Additionally, the crack was largely situated along ply interfaces, indicating delamination as the primary damage mode.

Results from DVC found tensile strains that followed the contours of damage cracks and compressive strains that coincided with voids in the sample. At the impacted side, strain measurements ranged from -0.16 mm/mm to 0.16 mm/mm. Additionally, the middle carbon layer experienced the highest strain concentrations, demonstrating that the surrounding aramid layers effectively dispersed energy along the interfaces to minimize damage within the carbon layer and induce plastic deformation instead.

In conclusion, μCT was applied to SHPB impact testing of a 2D tubular hybrid braided composite for rapid, automated, and thorough characterization of its response to transverse impact. An algorithm-based methodology was presented to extract the volumetric properties of the composite structure before and after impact damage. A thorough analysis was performed on sample geometry, void properties, and internal damage using statistical methods. Finally, DVC was performed, and strain measurements correlated with the developed algorithms' findings.

4.2 Recommendations

The algorithms developed in this work have demonstrated good versatility for impact characterization of advanced materials. In this section, recommendations are provided for successful experimentation of impact testing for braided composites to ensure good repeatability of results. These recommendations were formulated based on the author's experience through the work in this thesis. This section presents recommendations in three major categories: sample preparation, SHPB instrumentation and testing, and data analysis.

Several factors should be considered when preparing 2D tubular braided composite samples to achieve high sample quality, repeatable scanning, and effective measurements. When manufacturing a tubular braided composite from multiple layers of dry braided preforms, care should be taken at each step of the process to prevent fibre warpage and ply wrinkling to limit the introduction of defects into the final part. Instructions for carrying out the manufacturing process are provided in Appendix B . If a work primarily focuses on DVC, it is recommended to use particle seeding, where high-density particles (e.g., copper) are introduced into the epoxy resin during the manufacturing process. This process will allow for more reliable tracking of subsets by DVC and limit poorly correlated regions. After sample manufacturing, it is also recommended to apply a witness marker to the point of impact (e.g., by applying a spot of paint). This step is helpful to both SHPB testing and μCT scanning. For SHPB, the witness marker will serve as the contact point for the incident bar of the apparatus. If a work considers the study of multiple impacts, the witness marker will ensure a fixed impact site for each subsequent test. For μCT, the witness marker will provide a point of reference for the sample to be oriented consistently between scans, such that better sample alignment can be achieved and data loss and residual misalignment from image registration is minimal. Additionally, the location of the impact site can be more precisely identified from the reconstructed images.

When performing SHPB testing, it is recommended to instrument the apparatus with strain gauges such that the input and reflected waves can be measured over time. These strain gauge measurements and sample properties can be used to evaluate the applied load over time, which is useful for applying fracture mechanics theory to the findings of µCT. This data can provide further insight into the validity of numerical models based on SHPB testing. Additionally, it is recommended to choose impact energy levels that induce multiple observable damage modes in the material. For instance, it is expected that as the applied impact energy is increased, through-thickness matrix cracking will be observed, followed by fibre fracture.

When processing and analyzing the data, it is important to examine the results from each step of each algorithm one at a time. Each processing algorithm performs a set of operations in decreasing order of scope, where early steps aim to address general contents across the full image, while late steps are targeted towards more specific objects and serve as refinement steps. Achieving the optimal configurations in the processing algorithms for a given sample depends on tuning several parameters, such as filter window sizes, object property limits, and refinement thresholds. This limitation exists due to the variability of sizes and shapes of materials, voids, and damage.

4.3 Future Work

The use of the presented methodology in impact testing of 2D tubular hybrid braided composites demonstrates the versatility of the developed algorithms for application to other pathways of future research. Continued work in this field can be done through testing of various material configurations, by using different inter-ply hybrid lay-up configurations, or by incorporating intra-ply hybrid textile or commingled fibre preforms. The damage profiles between different hybrid materials can be compared to identify various phenomena caused by material hybridization for braided composites.

As another approach, testing can also involve impacting tubular braided samples multiple times and scanning them between each test. This approach can quantify progressive damage development, and the dominant damage modes can be identified after each impact event. Additionally, the DVC technique can be leveraged further to provide more insightful data in the form of progressive strains between testing stages.

Testing can also be performed on braided composites in varying geometric configurations to study their effects on impact performance. For tubular geometries, samples can be manufactured at varying braid angles or on varying mandrel diameters. Braided composite samples can also be manufactured into shapes like rectangular tubes or flat panels. The variation of induced stress concentrations can provide direct implications on the applicability of geometric configurations in the design of high-performance parts.

Finally, this methodology can be applied to FEA, where numerical models of impact testing can be developed and validated with experimental data acquired by µCT and DVC. As more experimental data becomes available to relate material configurations, void networks, imperfections, and impact energy levels to expected damage profiles and strain behaviours, more opportunity is presented for the development of more complete numerical models for braided composites. Such models are particularly useful in rapidly determining the mechanical properties of complex materials without the cost of experimental testing, which can expedite the design turnaround of new materials for specialized applications.

Appendix A Image Processing for Braided Composites

A.1 Introduction

This appendix provides a demonstration of the image processing steps used in this work using an example image of the tubular braided composite. The code provided in this appendix demonstrates the process of geometry analysis, void extraction, and crack detection. Next, the supplemental data is provided, along with important information and instructions on its use.

A.2 Sample MATLAB Code

A.2.1 Tubular Braided Composite Image Processing Example

Author: Alexander Dondish

E-mail: alexdon@yorku.ca

Date: 2023-06-15

Article: Assessment of low-velocity impact response of a hybrid carbon-aramid braided composite by algorithmic quantification of volumetric structures

Description: In this Live Script, the image processing scheme will be illustrated using an example image.

```
clear; clc;

exampleFile = 'E:\OneDrive - York University\Research\uCT Data\0-SCM-DOT-02\Registration\T-S01-0-SCM-DOT-02_IR_rec0000_Tar_Tar0598.png';

scanPixelSize = 9.3; % [microns]

exampleImage = imread(exampleFile);
```

```
imshow(exampleImage); title('Original Resolution Image Slice');
```

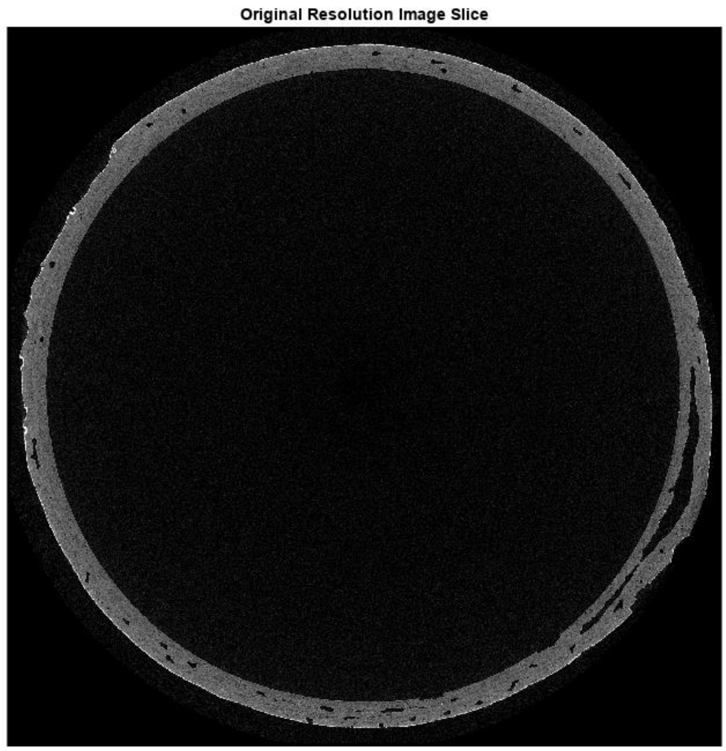

A.2.2 Geometry Analysis and Void Extraction

The image is downsampled by a factor of 4 on each axis.

```
im1Resized = imresize(exampleImage, 1/4);
imshow(im1Resized); title('Geometry Analysis and Void Extraction - 4x4
Downsampled Image Slice');
```

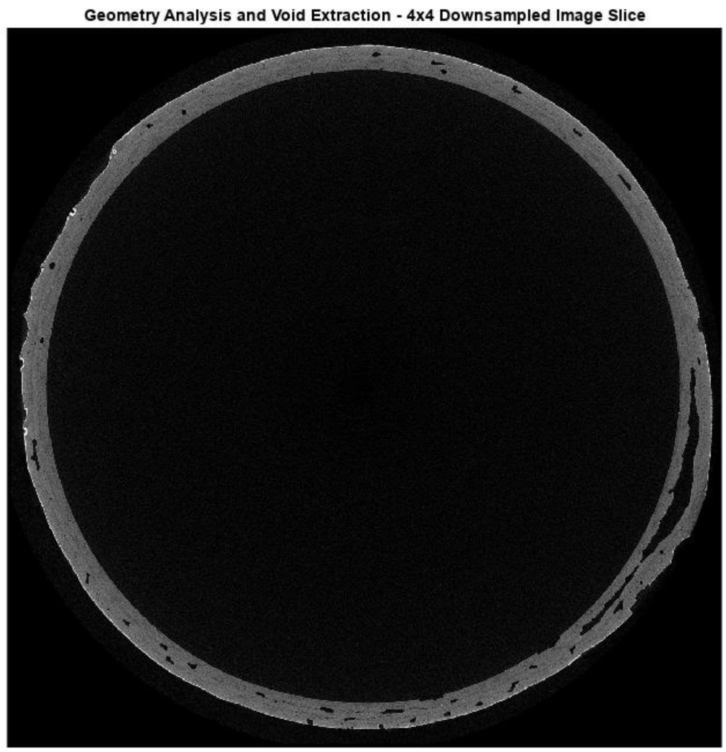

A median filter with a window size of 3 is applied as a pre-processing step.

```
im1PreProcessed = medfilt2(im1Resized, [3, 3]);
imshow(im1PreProcessed); title('Geometry Analysis and Void Extraction - Median Filtered Image Slice');
```

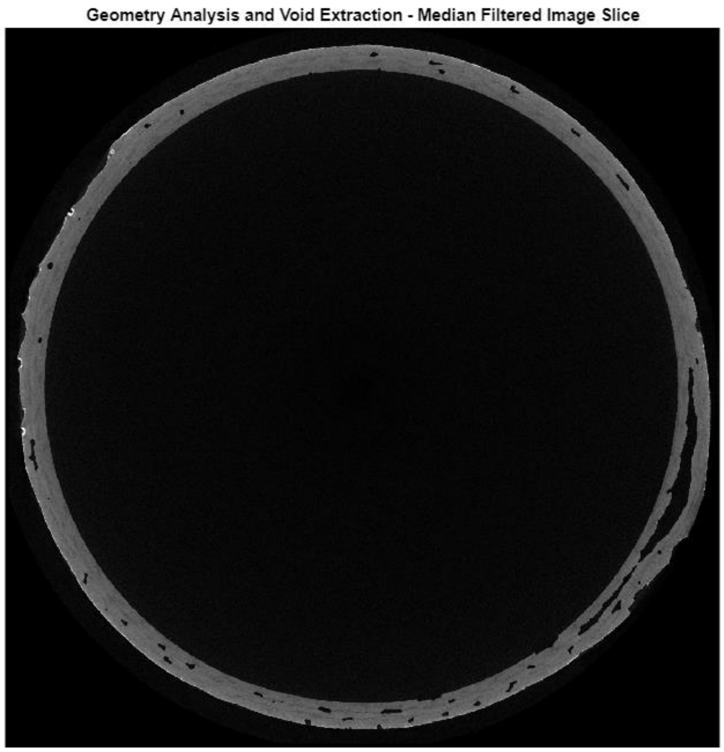

The image histogram is acquired and an optimal threshold for binarization is evaluated.

```
hist = imhist(im1Resized); imhist(im1Resized); title('Geometry Analysis and Void Extraction - Image Histogram');
```

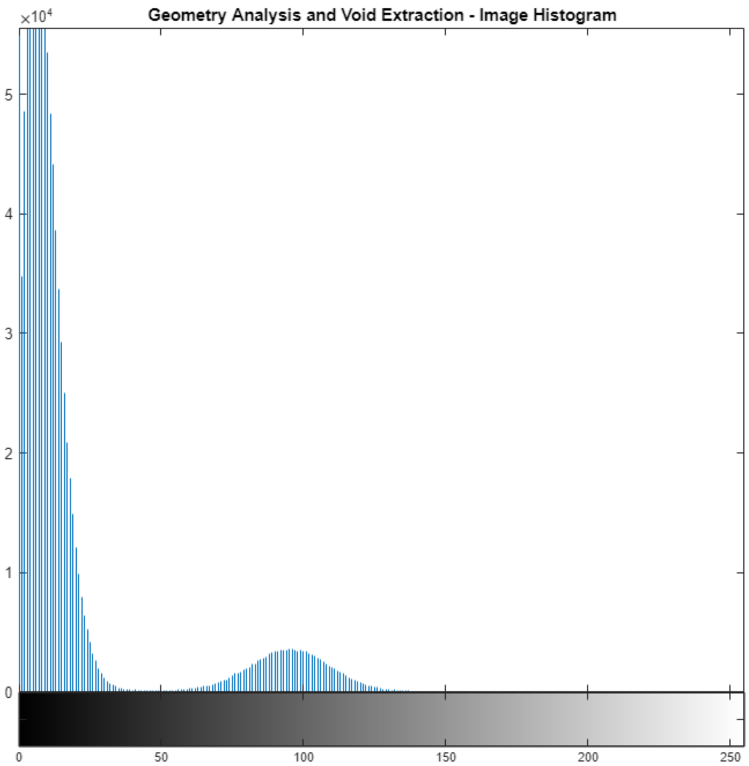


```
hist(1) = [];
countMaxima = sum(islocalmax(hist));
peakProminence = 0;

while countMaxima > 2
    peakProminence = peakProminence + 2;
    [peakVal, peakIdx] = findpeaks(hist, 'MinPeakProminence', peakProminence);
    countMaxima = length(peakIdx);
    if peakProminence > length(hist)
        disp('[Count Maxima] Something must be wrong here. Stopping auto
threshold...');
        return;
    end
end

leftLimReg = hist(peakIdx(1):floor(mean(peakIdx)));
rightLimReg = hist(ceil(mean(peakIdx)):peakIdx(2));
findLeftLimLocal = find(abs(leftLimReg - 0.05 * peakVal(2)) ==
min(abs(leftLimReg - 0.05 * peakVal(2))));
```

```
 findRightLimLocal = find(abs(rightLimReg - 0.05 * peakVal(2)) ==
min(abs(rightLimReg - 0.05 * peakVal(2))));
 globalLims = [findLeftLimLocal + peakIdx(1) - 1, findRightLimLocal +
ceil(mean(peakIdx)) - 1];

 threshold = round(mean(globalLims));
 disp(strcat({'Threshold set to '}, string(threshold)));
```

```
Threshold set to 53
```

The 8-bit image is then binarized using the acquired threshold value.

```
 im1Binarized = imbinarize(im1PreProcessed, threshold / 255);
 imshow(im1Binarized); title('Geometry Analysis and Void Extraction - Binarized
Image');
```

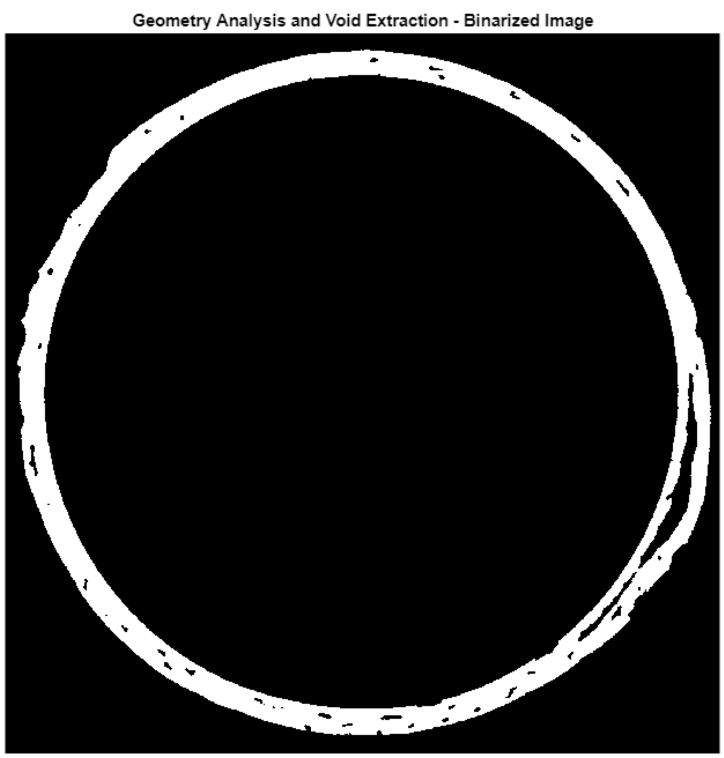

A flood-fill operation is performed to acquire the outer profile of the cross-section. Image subtraction and size filtering is performed to acquire the inner profile.

```
 exteriormask = imfill(im1Binarized, 'holes');
 imshow(exteriormask); title('Geometry Analysis and Void Extraction - Outer
Profile');
```

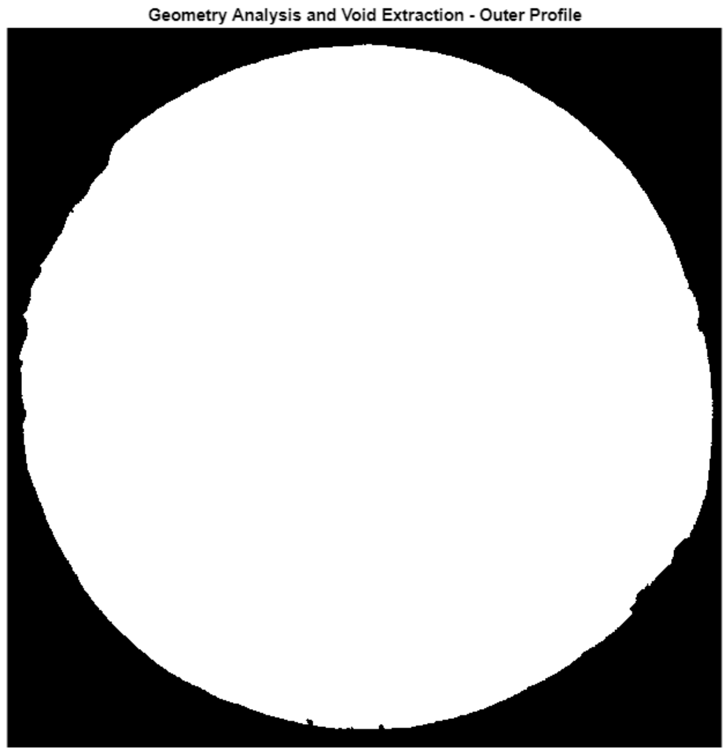


```
 interiorplusvoids = and(exteriormask, ~im1Binarized);
 imshow(interiorplusvoids); title('Geometry Analysis and Void Extraction - Inner
Profile and Voids');
```

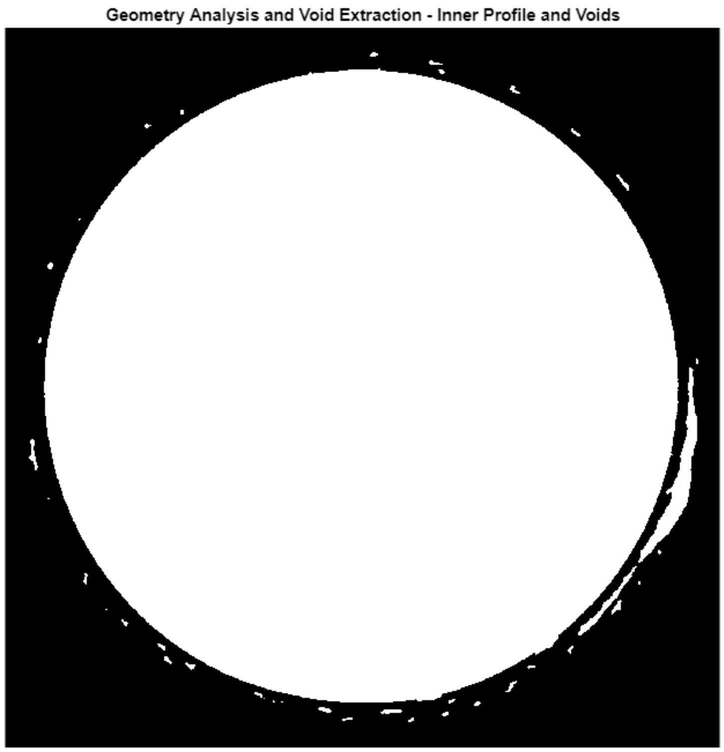


```
interiormask = bwareafilt(interiorplusvoids, 1, 'largest');
imshow(interiormask); title('Geometry Analysis and Void Extraction - Inner Profile');
```

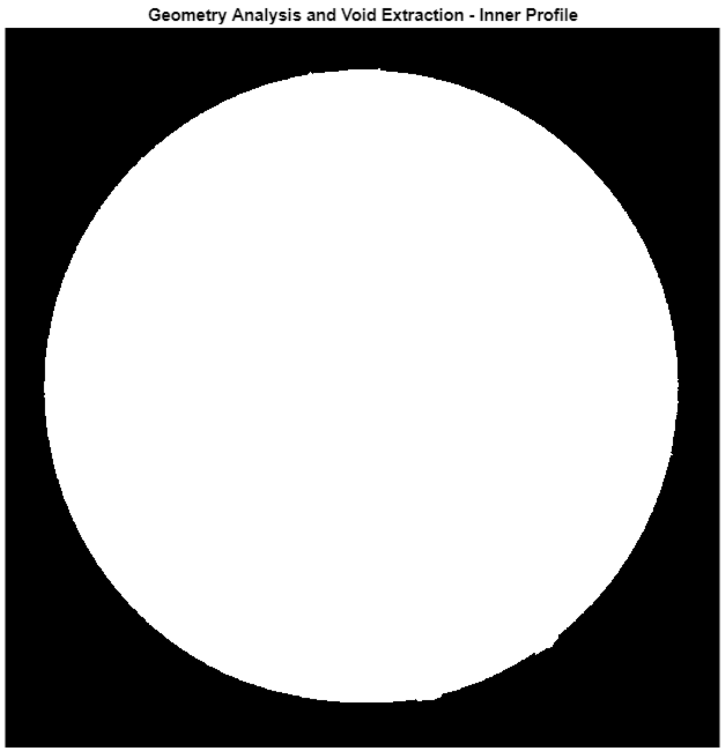

Voids are extracted using a Boolean operation.

```
voids = ~im1Binarized & exteriormask & ~interiormask;
imshow(voids); title('Geometry Analysis and Void Extraction - Isolated Voids');
```

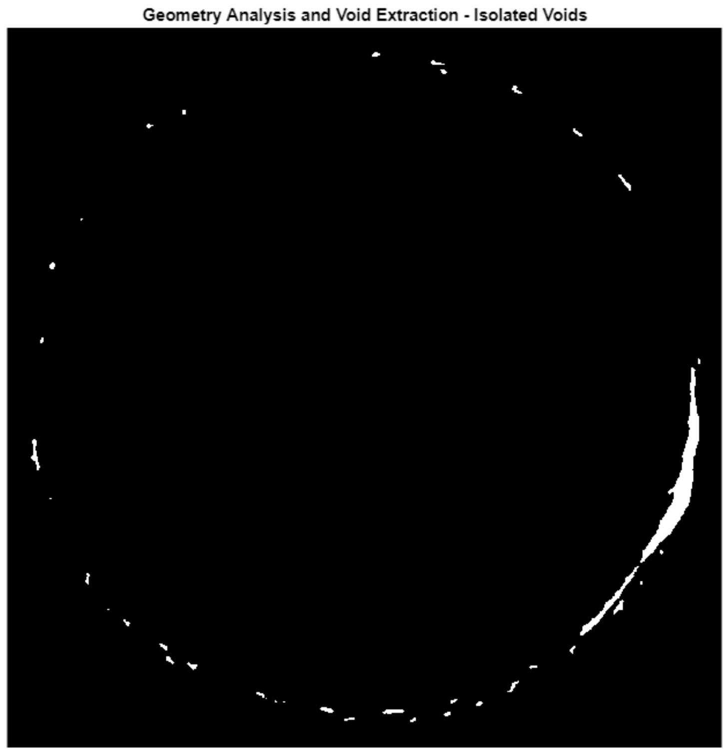

A.2.3 Crack Detection

The image is downsampled by a factor of 2 on each axis.

```
im2Resized = imresize(exampleImage, 1/2);
imshow(im2Resized); title('Crack Detection - 2x2 Downsampled Image Slice');
```

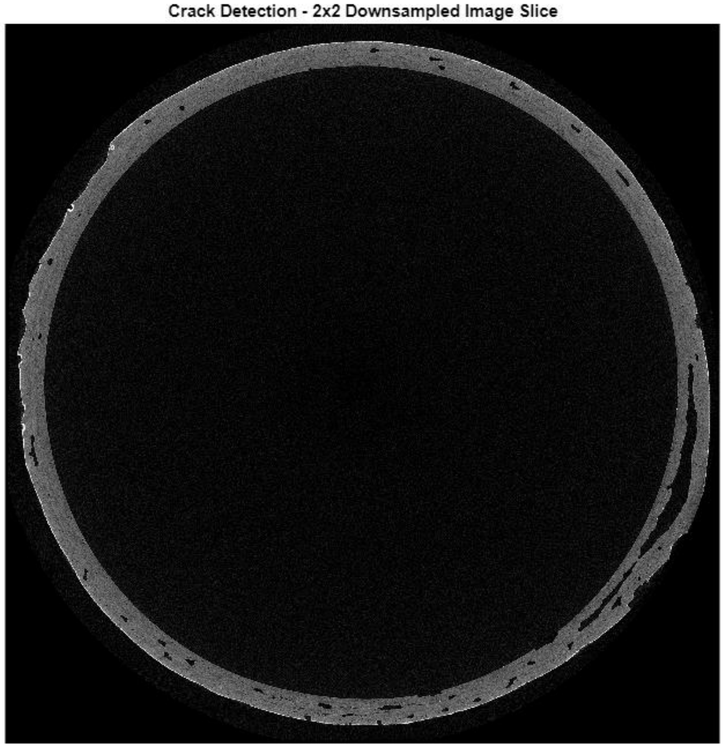

The image is binarized manually using a higher threshold to capture all of the darker features.

```
im2Binarized = imbinarize(im2Resized, 65 / 255);
imshow(im2Binarized); title('Crack Detection - Binarized Image');
```

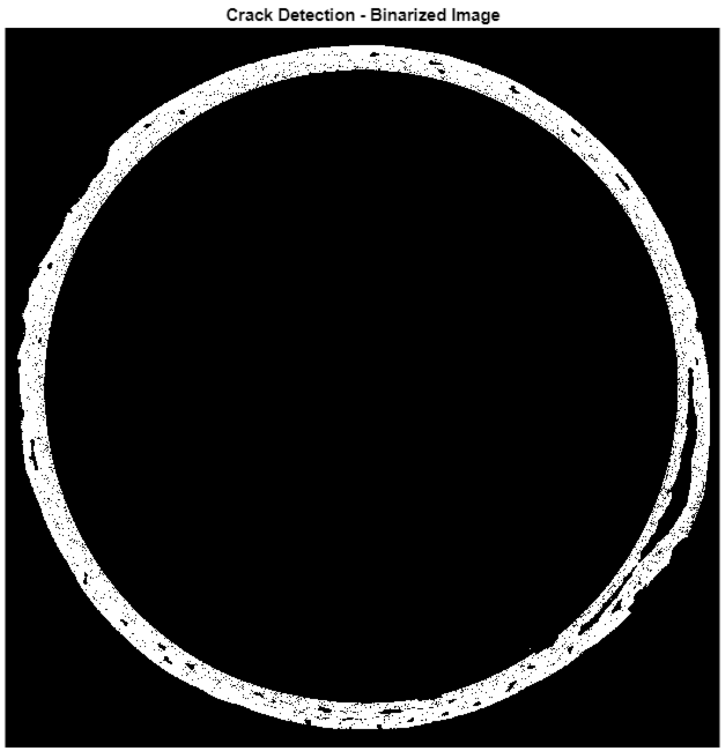

A mask is created by substantial median filtering to extract thin features by image subtraction.

```
tMed = medfilt2(im2Resized, [11, 11]);
imshow(tMed); title('Crack Detection - Median Filtered Image for Masking');
```

Crack Detection - Median Filtered Image for Masking

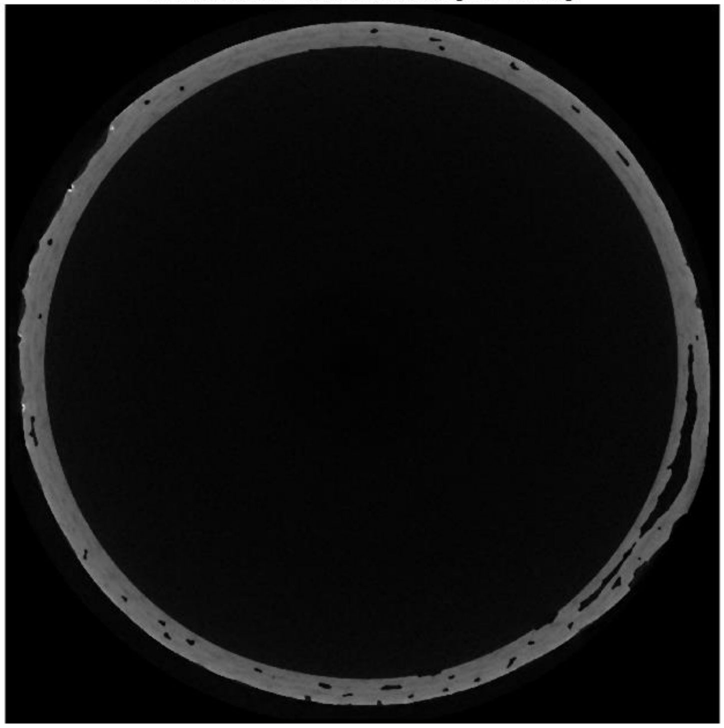

```
medbin = imbinarize(tMed, 70 / 255);
imshow(medbin); title('Crack Detection - Binarized Masking Image');
```

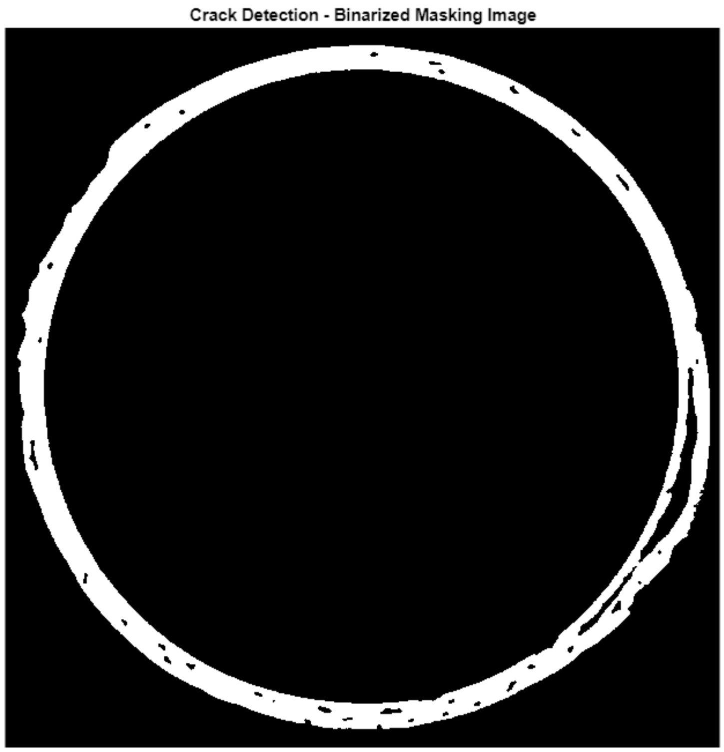


```
 imcrackinit = and(~im2Binarized, medbin);
 imshow(imcrackinit); title('Crack Detection - Initial Candidate Crack
Features');
```

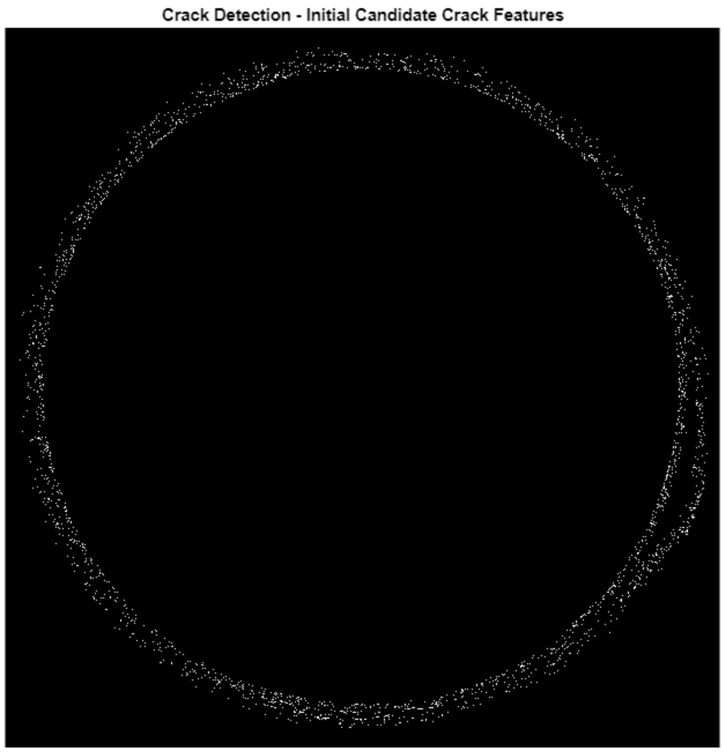

The initial features are then filtered by eccentricity, such that only thin features with an eccentricity of at least 0.9 are retained.

```
imeccfilt = bwpropfilt(imcrackinit, 'Eccentricity', [0.9, 1]);
imshow(imeccfilt); title('Crack Detection - Filtered Thin Features');
```

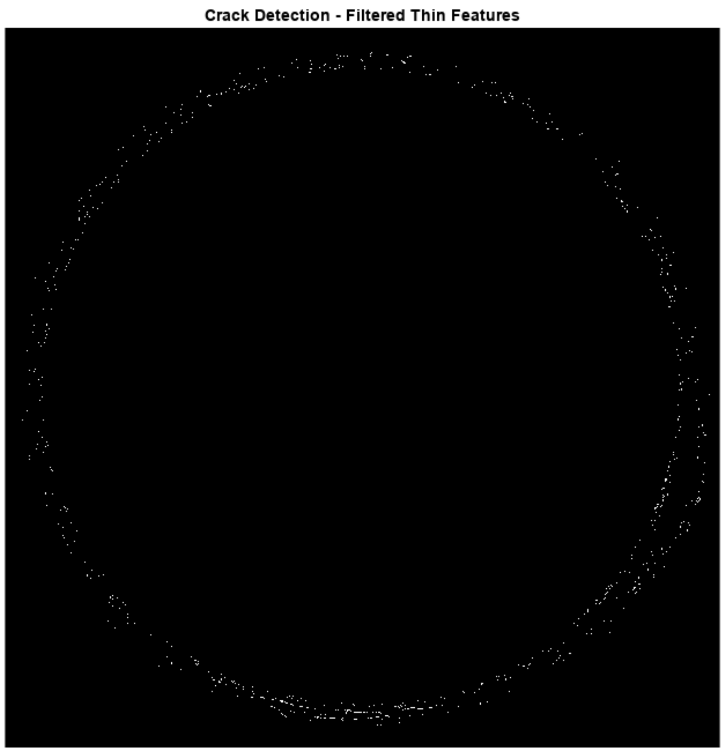

For the full volume, small objects are detected and removed as 3D objects. Here, 2D object area filtering is performed instead for demonstration purposes.

```
imareafilt = bwareafilt(imeccfilt, [20, Inf]);
imshow(imareafilt); title('Crack Detection - Small Objects Removed');
```

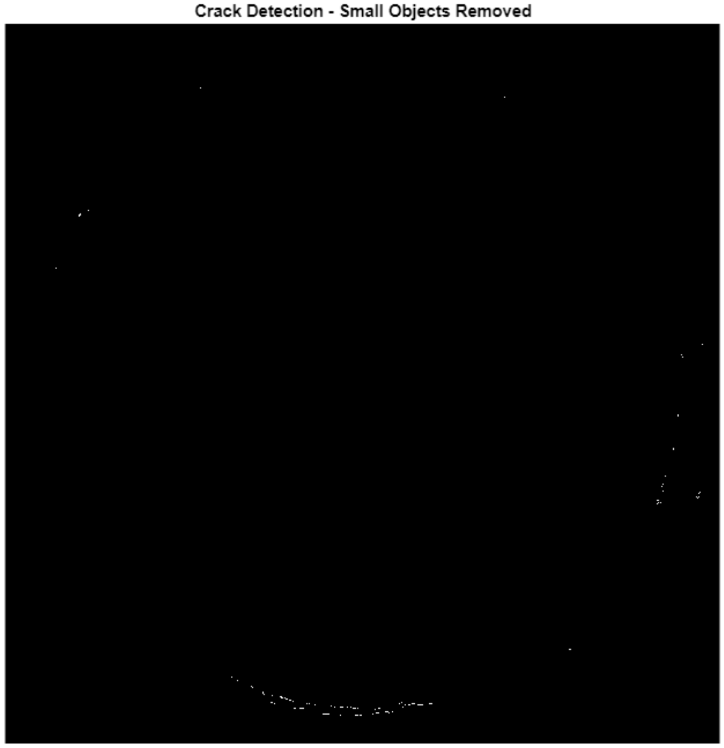

Objects are clustered by masking using heavy image dilation. The largest object of this mask is taken as the region of the crack profile.

```
tDilated = imdilate(imareafilt, strel('disk', 41));
imshow(tDilated); title('Crack Detection - Object Clustering');
```

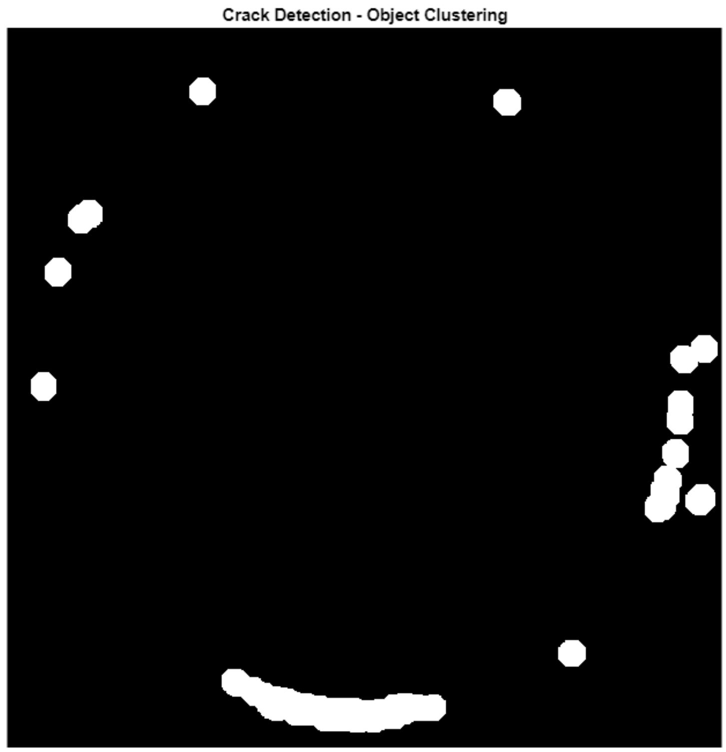


```
tMask = bwareafilt(tDilated, 1);
imshow(tMask); title('Crack Detection - Identified Largest Cluster');
```

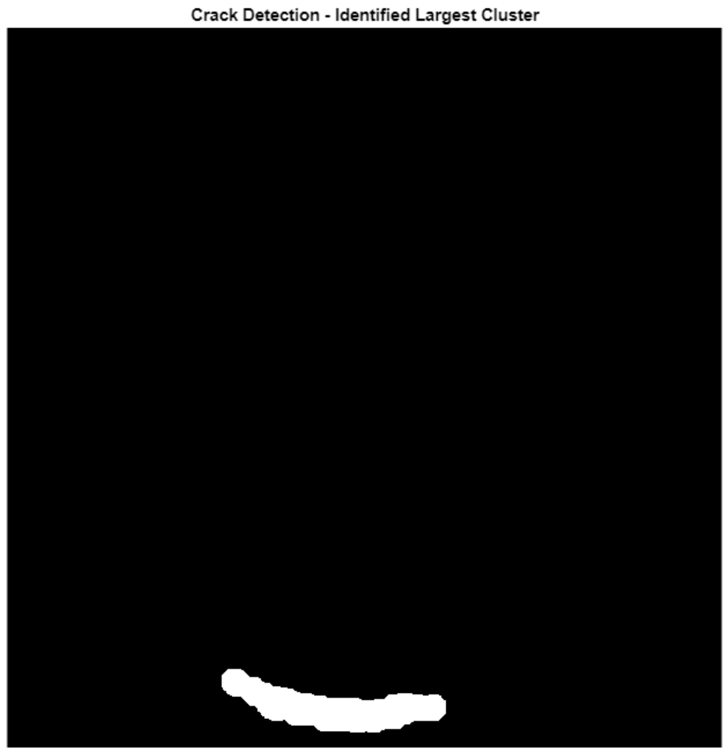


```
tDamage = and(imareafilt, tMask);
imshow(tDamage); title('Crack Detection - Final Identified Crack');
```

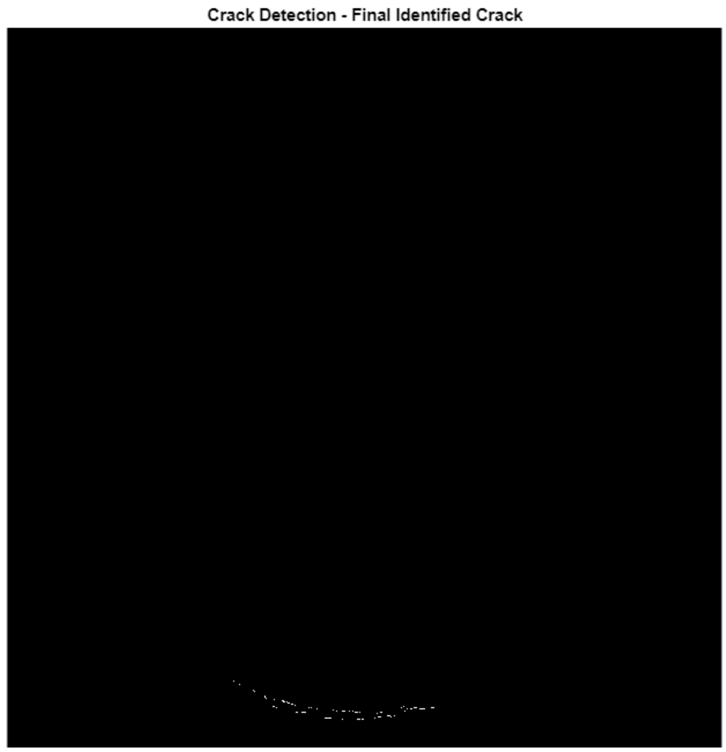

A.3 Supplemental Data and Instructions

A.3.1 Data Repository

The data used in this work is available in the FRDR repository:

https://doi.org/10.20383/103.0770

A.3.2 General Information

1. Title of Dataset: Assessment of low-velocity impact response of a hybrid carbon-aramid braided composite by algorithmic quantification of volumetric structures

2. Author Information

Name: Dondish, Alexander

Institution: York University

Email: alexdon@yorku.ca

Name: Melenka, Garrett W.

Institution: York University

Email: gmelenka@yorku.ca

3. Information about funding sources that supported the collection of the data:

Funder: Natural Sciences and Engineering Research Council of Canada

Award No.: RGPIN-2018-05899

A.3.3 Sharing and Access Information

1. Licenses/restrictions placed on the data:

These data are available under a CC BY-SA 4.0 license <https://creativecommons.org/licenses/by-sa/4.0/>

2. Was data derived from another source? yes/no

A. If yes, list source(s): No.

3. Recommended citation for this dataset:

Dondish, A., Melenka, G.W. (2023). Assessment of low-velocity impact response of a hybrid carbon-aramid braided composite by algorithmic quantification of volumetric structures. Federated Research Data Repository. https://doi.org/10.20383/103.0770

A.3.4 Data and File Overview

1. File List

list all files (or folders, as appropriate for dataset organization) contained in the dataset, with a brief description

A. Filename: Registration\P-S01-0-SCM-DOT-02_IR_rec_Ref_Ref0000*.png

Short description: Image slices reconstructed from CT of the pre-impact tubular braided composite sample and registered.

B. Filename: Registration\T-S01-0-SCM-DOT-02_IR_rec0000_Tar_Tar*.png

Short description: Image slices reconstructed from CT of the post-impact tubular braided composite sample and registered.

C. Filename: Registration*_spr.png

Short description: Original projections acquired by the CT apparatus, cropped and adjusted to illustrate registration.

D. Filename: Registration*.log

Short description: Scan log files.

E. Filename: MATLAB Code\TubeCT.m

Short description: MATLAB code file for void and geometry extraction and void registration of the undamaged and damaged samples.

F. Filename: MATLAB Code\TubeGeometry.m

Short description: MATLAB code file for extraction of geometry properties of the inner and outer surfaces of the samples.

G. Filename: MATLAB Code\TubeVoidHist.m

Short description: MATLAB code file for statistical analysis of registered voids in the samples.

H. Filename: MATLAB Code\TubeCrackDetect.m

Short description: MATLAB code file for detection and generation of the impact crack profile of the damaged sample.

I. Filename: MATLAB Code\TubeCrackPostProcess.m

Short description: MATLAB code file for statistical analysis of the acquired crack profile.

J. Filename: MATLAB Code\TubeProcessingExample.mlx

Short description: MATLAB Live Script file to demonstrate the processing steps of an example image.

K. Filename: MATLAB Code\TubeProcessingExample.pdf

Short description: PDF document of the processing steps in TubeProcessingExample.mlx

2. Relationship between files, if important:

The code in the file TubeCT.m must be run to acquire the variables required to run TubeGeometry.m and TubeVoidHist.m.

The code in the file TubeCrackDetect.m must be run to acquire the variables required to run TubeCrackPostProcess.m.

A.3.5 Methodological Information

1. Description of methods used for collection/generation of data:

To generate the provided data, the following workflow was followed:

1. Projections of the sample were collected from the μCT apparatus
2. The acquired projections were reconstructed into image slices along the length of the sample using CT data reconstruction software
3. The image slices of the damaged (target) sample were registered to those of the undamaged (reference) sample using 3D data inspection software.

2. Methods for processing the data:

The following file naming convention was followed for the provided data: Sample Damage State - Scan Number - Sample Name

Sample Damage State:

P: Pre-impact

T: Post-impact

Scan Number:

Example: S01 = scan 1

Sample Name:

Example: 0-SCM-DOT-02 = sample name based on internal naming convention

Following image registration:

For the reference images (i.e., P-S01-...), a suffix of "Ref" was added, followed by the image slice index.

For the target images (i.e., T-S01-...), a suffix of "Tar" was added, followed by the image slice index.

The MATLAB code uses the above file naming conventions to read files automatically. The files should be contained in a folder named "Registration", in a folder with the same name as the sample, in a root folder that the user can define in the code.

Example: If the root folder is C:\Data and the sample name is 0-SCM-DOT-02, the code will search for files in C:\Data\0-SCM-DOT-02\Registration\...

3. Instrument- or software-specific information needed to interpret the data:

The following toolboxes are required to run the provided MATLAB code:

A. Image Processing Toolbox

B. Signal Processing Toolbox

C. Statistics and Machine Learning Toolbox

D. Curve Fitting Toolbox

Appendix B Multi-Layered Braided Composite Manufacturing

B.1 Introduction

This appendix provides technical information on manufacturing 2D tubular braided composites with multiple fibre layers. For this process, a hardened steel mandrel with a length of 457.2 mm (18”) and a diameter of 38.1 mm (1.5”) was used. The target product is a three-layered material with a length of 317.5 mm (12.5”).

B.2 Preparing the Braided Sleeves

1. Cut three braided sleeves into lengths of 381.0 mm (15”).
    a. Pull and stretch the sleeving over the mandrel.
    b. Measure and mark the length of 381.0 mm (15”). This can be done by a small cut into the sleeve with scissors.
    c. Remove the braid from the mandrel, then cut the braid to length.

d. Subsequent braid pieces may be cut using the first cut as a reference.

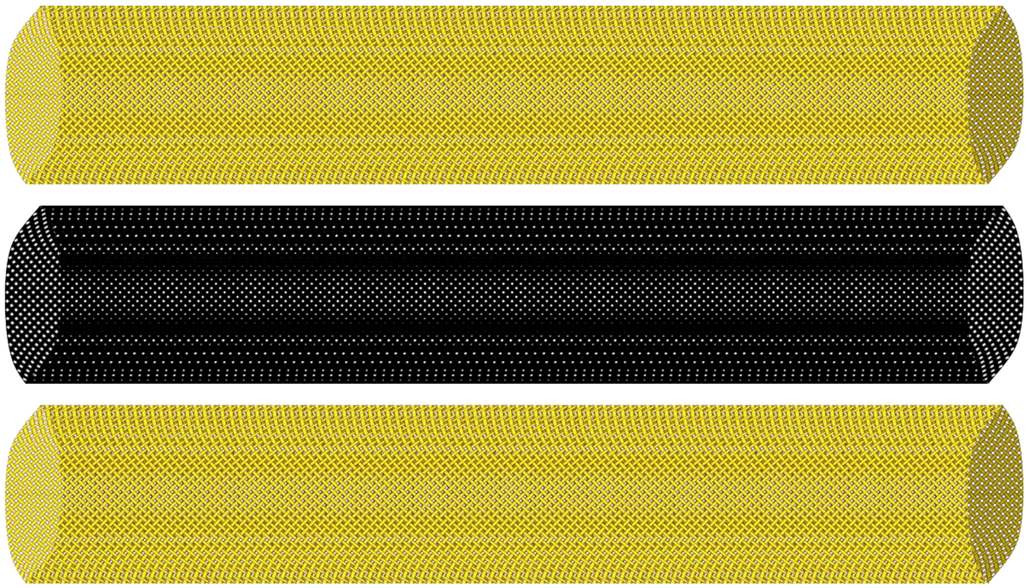

2. Form braided sleeves into a bundle.

   a. Fully compress the braided sleeve that will serve as the outer layer.

   b. Fully stretch the braided sleeve that will serve as the middle layer, then slot it through the outer sleeve.

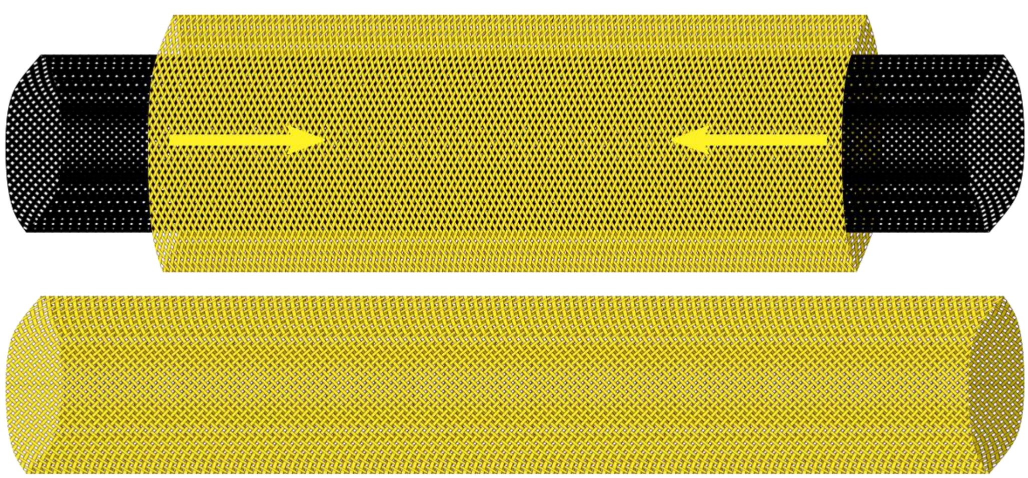

   c. Fully compress the middle sleeve such that it meets with the outer sleeve.

d. Fully stretch the braided sleeve that will serve as the inner layer, then slot it through the outer and middle sleeves.

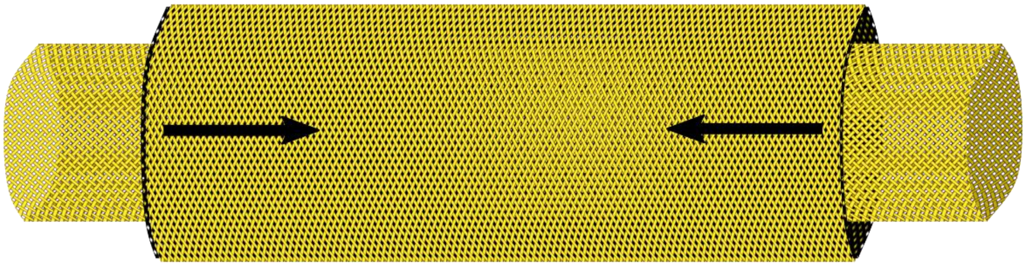

e. Carefully stretch the outer and middle sleeves over the inner sleeve.

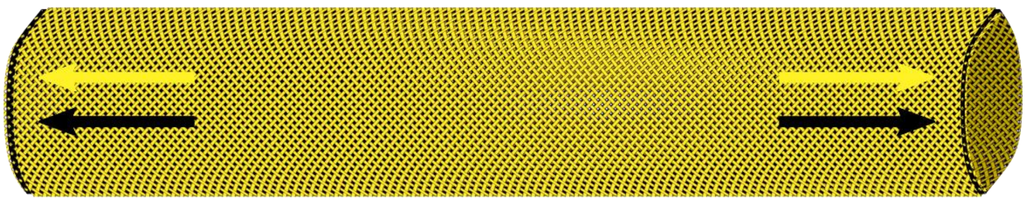

B.3 *Preparing the Mandrel*

1. Prepare a layer of peel ply by cutting it to a 381 mm × 139.7 mm (15” × 5.5”) rectangular sheet.

2. Apply mold release to the mandrel surface (wear nitrile gloves for this process).

   a. Apply mold release (Frekote 700-NC, Loctite, Düsseldorf, Germany) to a rag, then apply an even coating onto the surface of the mandrel.

   b. Apply a total of three coats. Let dry for 5-10 minutes between coats and 15-20 minutes after the final coat.

3. Wrap a layer of 25.4 mm (1”) PET tape at each end of the mandrel.

4. Pull the braided sleeve bundle over the mandrel, positioning it in the middle of the mandrel such that about 38.1 mm (1.5”) of space is left at each end.

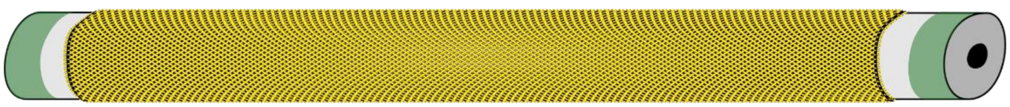

5. Fasten one end of the braided sleeves to the mandrel using a layer of PET tape, such that 12.7 mm (0.5”) adheres to the mandrel and 12.7 mm (0.5”) adheres to the braided sleeves.

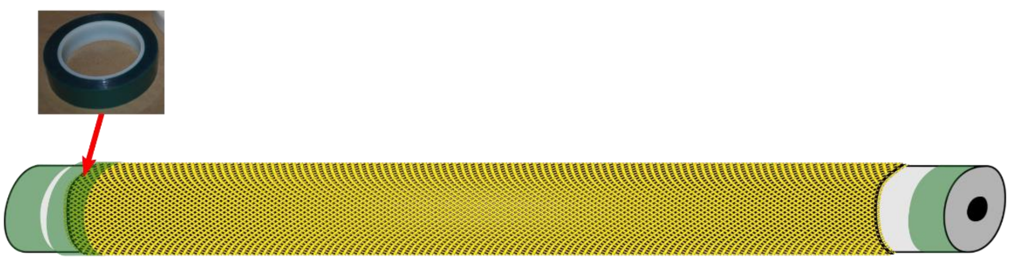

6. Cover the remaining exposed surface of the mandrel with PET tape. Do not fasten the other end of the braided sleeves to the mandrel. There should be minimal overlap between the fibres and the tape and no remaining exposed surface on the mandrel.

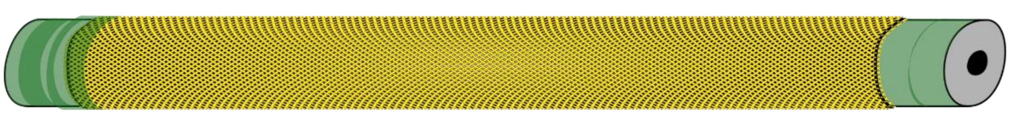

7. Apply 25.4 mm (1”) double-sided tape, leaving the backing, just outside each end of the exposed regions of the braided sleeves.

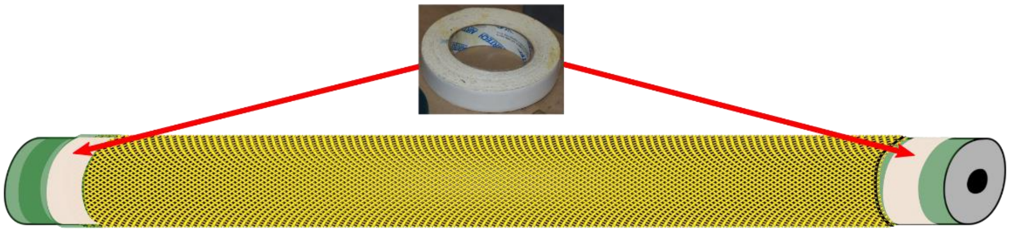

B.4 Hand Lay-Up

1. Set the mandrel horizontally on a stand or a set of V-blocks.

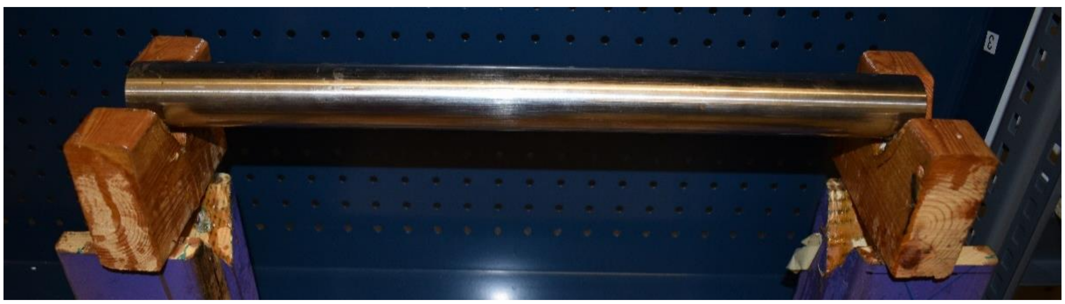

2. Prepare the epoxy mixture (<u>nitrile gloves, lab coat, and safety glasses required</u>).

   a. Measure 50 g of resin (#2000, Fibre Glast Developments Corp., Brookville, OH) and 13.5 g of 60-minute hardener (#2060, Fibre Glast Developments Corp., Brookville, OH).

b. Combine the resin and hardener and stir for 60 seconds. Once the mixing begins, the working time is 60 minutes, after which the resin will begin to gel and fail to apply to the fibres.

3. Apply the epoxy onto the braids.

    a. Draw the resin mixture through a syringe to reduce messes.

    b. Using the syringe, apply the resin lengthwise onto the braided sleeves, starting from the fastened end and moving towards the free end. Use your gloved fingers to evenly smear the epoxy onto the fibres. Do not use any motions in the opposite direction as this will cause fibre warpage and ply wrinkling. Rotate the mandrel occasionally and repeat this process until the fibres are fully saturated and no longer absorb additional epoxy.

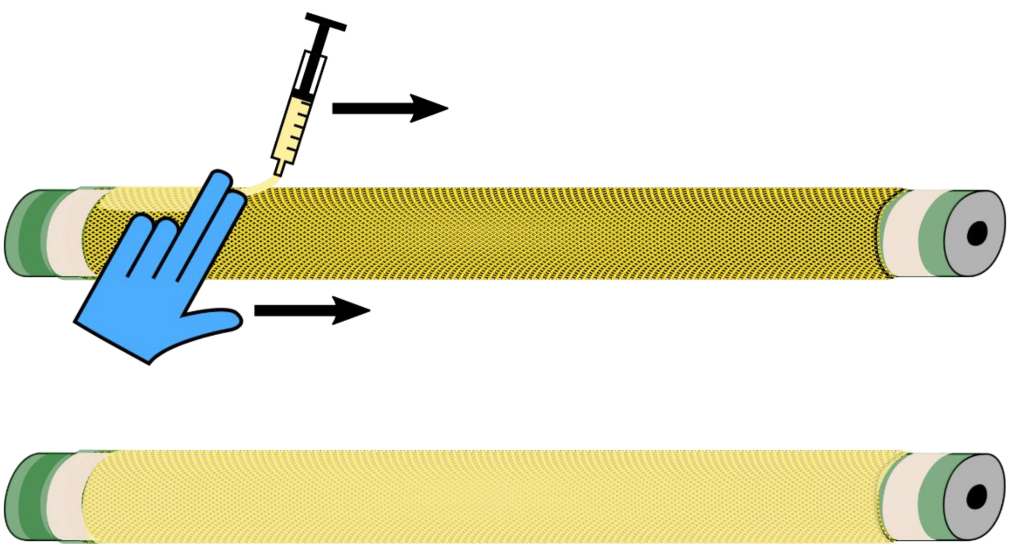

4. Apply the peel ply and heat shrink.

a. Remove the backing from the double-sided tape pieces at each end. Apply the peel ply onto the braids, making sure to stretch it tightly around the braids to minimize part defects. Ideally, the peel ply should reach a small portion of each piece of double-sided tape.

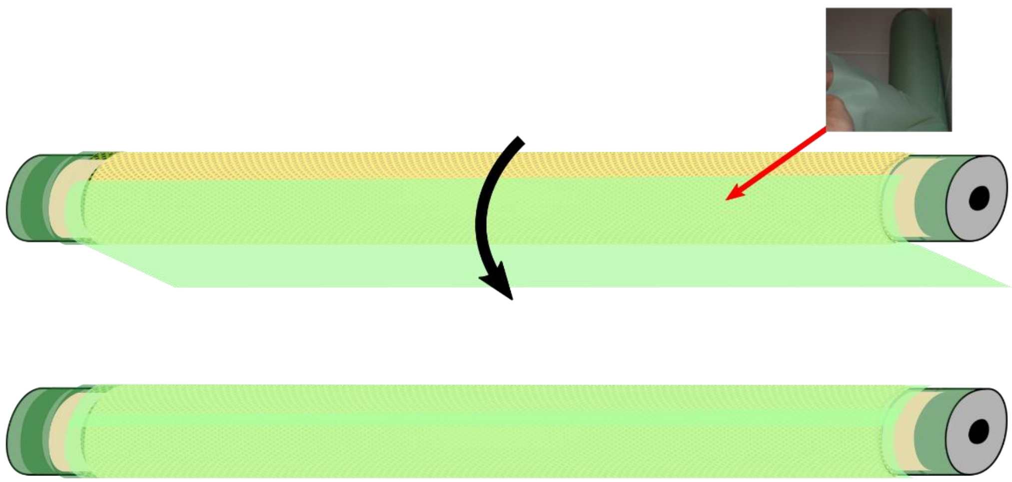

b. Apply heat shrink to the remaining double-sided tape at the fastened end. Wrap the heat shrink in a spiral, overlapping each pass by two-thirds to three-quarters of its width. Make sure to apply consistent pressure as you wrap the heat shrink to prevent wrinkling. Continue until you reach the double-sided tape at the free end and attach the heat shrink to it.

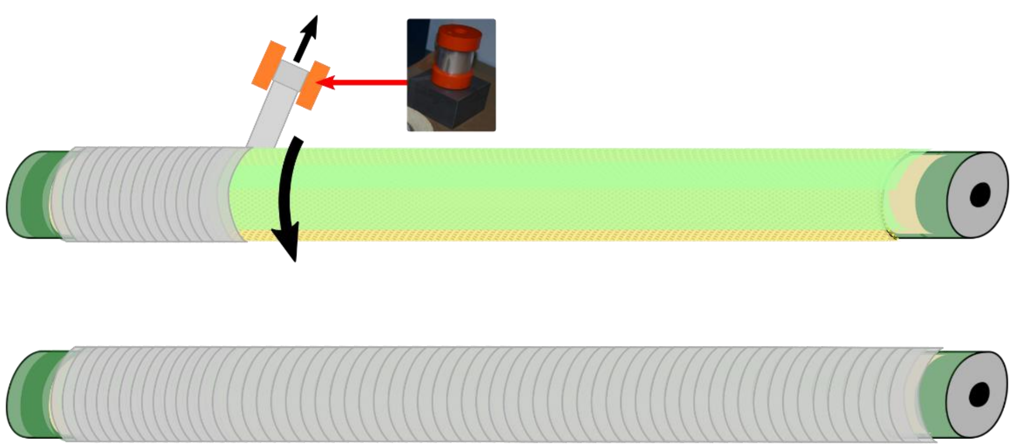

5. Heat the heat shrink (work gloves, lab coat, and safety glasses required for this step).
    a. Using a heat gun, evenly heat the heat shrink. Use lengthwise, steady, and moderately paced motions from the free end to the fastened end. Do not apply concentrated heat as this will cause the heat shrink to shrivel at that region. Rotate the mandrel occasionally and repeat until the heat shrink is fully attached to the material.

6. Allow the resin to cure for 24 hours.

B.5 Part Extraction

1. Clear the mandrel by removing the heat shrink, peel ply, double-sided tape, and as much of the PET tape as possible.
2. Extract the tube with a hydraulic press (safety glasses and safety boots, inserts, or toe covers are required). Press the mandrel through a jig with a press-fit hole diameter to release the tubular braided composite part.


50 TON
RK
MACHINERY
12 TO
WARNING
REMOVE LOAD BEFORE
RAISING OR LOWERING TABLE
CYLINDER ACTIVATION
POWER LIFT
DANGER
PROPER GUARDING MUST BE INSTALLED BETWEEN PRESS AND OPERATOR
DO NOT OPERATE WITHOUT EYE PROTECTION
KEEP HANDS AWAY